

ADVISORY COMMITTEE

Chairman – JAN KMITA¹
Subchairman – WOJCIECH GLABISZ²
JAN BILISZCZUK (Poland)
CZESŁAW CEMPEL (Poland)
ANTONI GRONOWICZ (Poland)
M.S.J. HASHMI (Ireland)
HENRYK HAWRYLAK (Poland)
RYSZARD IZBICKI (Poland)
WAŁAW KASPRZAK (Poland)
MICHAEL KETTING (Germany)
MICHAŁ KLEIBER (Poland)
VADIM L. KOŁMOGOROV (Russia)

ADOLF MACIEJNY (Poland)
ZDZISŁAW MARCINIAK (Poland)
KAZIMIERZ RYKALUK (Poland)
ANDRZEJ RYŻYŃSKI (Poland)
ZDZISŁAW SAMSONOWICZ (Poland)
WOJCIECH SZCZEPIŃSKI (Poland)
PAWEŁ ŚNIADY (Poland)
RYSZARD TADEUSIEWICZ (Poland)
TARRAS WANHEIM (Denmark)
WŁADYSŁAW WŁOSIŃSKI (Poland)
JERZY ZIÓŁKO (Poland)
JÓZEF ZASADZIŃSKI (Poland)

EDITORIAL BOARD

Editor-in-chief – ZBIGNIEW GRONOSTAJSKI³
ROBERT ARRIEUX (France)
AUGUSTO BARATA DA ROCHA (Portugal)
GHEORGHE BRABIE (Romania)
LESŁAW BRUNARSKI (Poland)
EDWARD CHLEBUS (Poland)
LESZEK F. DEMKOWICZ (USA)
KAZIMIERZ FLAGA (Poland)
YOSHINOBI FUJITANI (Japan)
FRANCISZEK GROSMAŃSKI (Poland)
MIECZYSLAW KAMIŃSKI (Poland)
Scientific secretary – SYLWESTER KOBIELAK

ANDRZEJ KOCANĀDA (Poland)
WAŁAW KOLLEK (Poland)
PIOTR KONDERLA (Poland)
ZBIGNIEW KOWAL (Poland)
TED KRAUTHAMMER (USA)
ERNEST KUBICA (Poland)
CEZARY MADRYAS (Poland)
TADEUSZ MIKULCZYŃSKI (Poland)
HARTMUT PASTERNAK (Germany)
MACIEJ PIETRZYK (Poland)
EUGENIUSZ RUSIŃSKI (Poland)
HANNA SUCHNICKA (Poland)

¹ The Faculty of Civil Engineering, Wrocław University of Technology
Wybrzeże Wyspiańskiego 27, 50-370 Wrocław, Poland
Tel. +48 71 320 41 35, Fax. +48 71 320 41 05, E-mail: jan.kmita@pwr.wroc.pl

² The Faculty of Civil Engineering, Wrocław University of Technology
Wybrzeże Wyspiańskiego 27, 50-370 Wrocław, Poland
Tel. +48 71 320 34 04, E-mail: wojciech.glabisz@pwr.wroc.pl

³ The Faculty of Mechanical Engineering, Wrocław University of Technology
ul. Łukasiewicza 5, 50-371 Wrocław, Poland
Tel. +48 71 320 21 73, Fax. +48 71 320 34 22, E-mail: metalplast@pwr.wroc.pl

Archives of Civil and Mechanical Engineering is indexed and abstracted in the following:

- Science Citation Index Expanded (also known as SciSearch®),
- Journal Citation Reports/Science Edition.

POLISH ACADEMY OF SCIENCES – WROCLAW BRANCH
WROCLAW UNIVERSITY OF TECHNOLOGY

ARCHIVES OF CIVIL AND MECHANICAL ENGINEERING

Quarterly
Vol. VIII, No. 4

WROCLAW 2008

EDITOR IN CHIEF

ZBIGNIEW GRONOSTAJSKI

EDITORIAL LAYOUT AND PROOF-READING

WIOLETTA GÓRALCZYK

TYPESETTING

SEBASTIAN ŁAWRUSEWICZ

SECRETARY

WIOLETTA GÓRALCZYK

**Publisher: Committee of Civil and Mechanical Engineering
of Polish Academy of Sciences – Wrocław Branch,
Faculty of Civil Engineering and Faculty of Mechanical Engineering
of Wrocław University of Technology**

© Copyright by Oficyna Wydawnicza Politechniki Wrocławskiej, Wrocław 2008

OFICyna WYDAWNICZA POLITECHNIKI WROCLAWSKIEJ

Wybrzeże Wyspiańskiego 27, 50-370 Wrocław

<http://www.oficyna.pwr.wroc.pl>

e-mail: oficwyd@pwr.wroc.pl

ISSN 1644-9665

Drukarnia Oficyny Wydawniczej Politechniki Wrocławskiej. Zam. nr 940/2008.

Contents

P. CICHOSZ, Economic aspects of cutting with diamond-coated wire	5
S. FRYDMAN, Ł. KONAT, G. PEKALSKI, Structure and hardness changes in welded joints of Hardox steels	15
A. GRAJCAR, W. BOREK, Thermo-mechanical processing of high-manganese austenitic TWIP-type steel	29
S. W. KOSTECKI, Numerical modeling of flow through moving water-control gates by vortex method. Part II – calculation result	39
R. NEUGEBAUER, M. TODTERMUSCHKE, R. MAUERMANN, F. RIEDEL, Overview on the state of development and the application potential of dieless mechanical joining processes	51
A. SABIK, I. KREJA, Linear analysis of laminated multilayered plates with the application of zig-zag function	61
K. SCHABOWICZ, B. HOŁA, Application of artificial neural networks in predicting earth-moving machinery effectiveness ratios	73
A. SKOŁYSZEWSKI, M. RUMIŃSKI, J. ŁUKSZA, Technological and material aspects of production of vibration compensators for exhaust systems	85
P. SKUBISZ, A. ŁUKASZEK-SOLEK, J. SIŃCZAK, S. BEDNAREK, Drop forging of HSLA steel with application of thermomechanical treatment	93
Information about PhDs	103

Spis treści

P. CICHOSZ, Ekonomiczne spekty cięcia struną diamentową	5
S. FRYDMAN, Ł. KONAT, G. PEKALSKI, Zagadnienia zmian struktur i twardości połączeń spawanych stali Hardox	15
A. GRAJCAR, W. BOREK, Obróbka cieplno-mechaniczna wysokomanganowych stali austenicznych typu TWIP	29
S. W. KOSTECKI, Numeryczne modelowanie przepływu przez ruchome zamknięcia wodne metodą wirów. Część II – wyniki obliczeń numerycznych	39
R. NEUGEBAUER, M. TODTERMUSCHKE, R. MAUERMANN, F. RIEDEL, Przegląd rozwoju i zastosowań bezmatrycowych mechanicznych procesów łączenia	51
A. SABIK, I. KREJA, Analiza liniowa laminowanych płyt warstwowych z zastosowaniem funkcji zig-zag	61
K. SCHABOWICZ, B. HOŁA, Zastosowanie sztucznych sieci neuronowych do predykcji wskaźników efektywności układów maszyn do robót ziemnych	73
A. SKOŁYSZEWSKI, M. RUMIŃSKI, J. ŁUKSZA, Technologiczne i materiałowe aspekty kompensatorów drgań dla układów wydechowych	85
P. SKUBISZ, A. ŁUKASZEK-SOLEK, J. SIŃCZAK, S. BEDNAREK, Proces kucia matrycowego stali HSLA z zastosowaniem obróbki cieploplastycznej	93
Informacja o pracach doktorskich	103



Economic aspects of cutting with diamond-coated wire

P. CICHOSZ

Wrocław University of Technology, Wybrzeże Wyspiańskiego 27, 50-370 Wrocław

Cutting with diamond-coated wire is of a great importance at shaping hardly workable materials. As the time goes by, due to the tool wear, cutting abilities of diamond wire are reduced up to 50%. Because of variable cutting capacity, using the full machining capacity of a wire in its entire lifetime would require a highly complicated feed drive kinematics of machine tools. The decreasing cutting capacity increases the operation costs and makes difficult taking the decision on the wire replacement. The paper presents a methodology of determining time, efficiency and costs of cutting with diamond wire. The results were verified with an experimental example. The presented mathematical formulae, used for the required transformations and calculations, have simple mathematical structure that is easy to be used in industrial conditions.

Keywords: *diamond wire, cutting, efficiency, costs*

1. Introduction

Cutting with abrasive wire reinforced with diamond grit is used for shaping hardly workable materials like ceramics, glass, minerals, laminates, liquid-sensitive materials etc. [2, 4, 7, 8, 9, 10]. Advantages of abrasive wire cutting are: low cutting temperature, very low surface structure defectiveness after cutting and a possibility of cutting along curvilinear paths [2, 3]. Disadvantages are: relatively expensive tooling and variable cutting capacity during the lifetime. Because of variable cutting capacity, using the full machining capacity of a wire in its entire lifetime would require a highly complicated feed drive kinematics of machine tools. Due to the proceeding tool wear, its cutting ability can be reduced even by half [2]. Too long operation of a wire results in a significant drop of cutting capacity, and too early replacement increases the portion of tooling in the manufacturing costs. So, the questions arise, when the wire should be replaced with a new one and what should be the optimum dullness criterion.

2. Methodology of determining efficiency and costs of diamond wire cutting

In the cases where instantaneous speed of the tool is constant within its entire lifetime, as e.g. during cutting with a circular or band saw, determining the principal cutting time t_g does not make any problem since that time depends on the applied cutting parameters, and more precisely on the feed rate v_f .

$$t_g = \frac{A_p}{Q_{ch}} = \frac{l \cdot h}{h \cdot v_f} = \frac{l}{v_f}, \quad [s] \quad (1)$$

where:

A_p – cut area of the workpiece in mm^2 ,

l, h – length and height of the cut contour in mm,

Q_{ch} – instantaneous cutting capacity in mm^2/s ,

v_f – feed rate (cutting rate) in m/s.

In this case, dullness condition of the mentioned tools does not affect the instantaneous cutting capacity but only the change, usually unfavourable, of technological effects like shape and dimension accuracy, surface layer quality of the workpiece etc.

Determining the principal cutting times (average for the whole product series), in which the instantaneous capacity is variable within the tool lifetime, as it happens e.g. during cutting with abrasive wire, requires a different approach.

Cutting with an abrasive wire can be performed in two basic kinematic versions: with constant pressure (Figure 1a), when the force acting in the direction of the workpiece travel in relation to the tool is constant ($F_f = \text{const.}$), and with constant feed rate ($v_f = \text{const.}$) (Figure 1b).

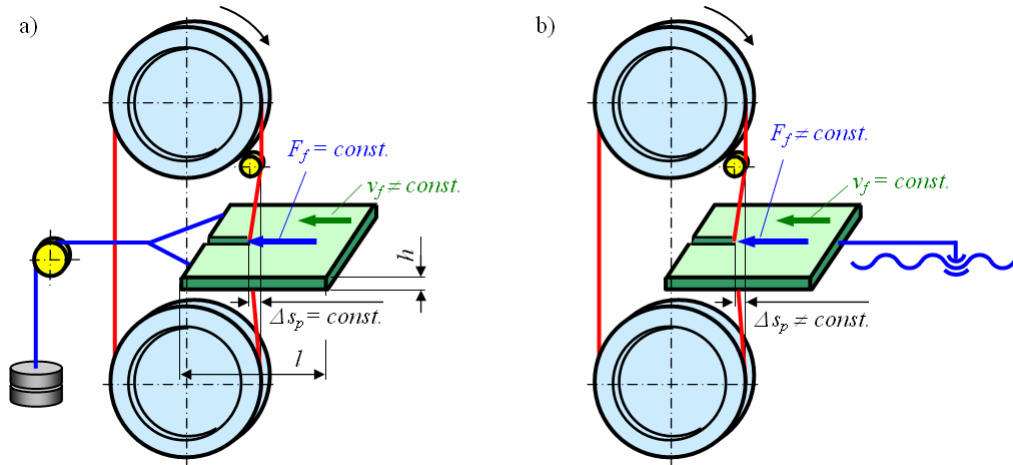


Fig. 1. Variants of kinematic cutting: (a) with constant pressing force, (b) with constant feed

Application of wire cutting at constant feed rate v_f is favourable with regard to its easy technical realisation. However, it is unfavourable with regard to the necessary low feed rates v_f which must correspond with the final stage of the wire lifetime and are much slower than at the beginning of the lifetime. This is because at the feed rates exceeding the wire cutting abilities, the workpiece travel in relation to the wire is faster than the real cutting speed. This leads to excessive transverse load of the wire

that results in its increasing deflection and, as a consequence, deteriorates the machining accuracy, and can even bring about the wire break. To prevent this, one should use the mentioned lower feed rates to secure that the cutting process will follow the workpiece travel in relation to the wire during its entire lifetime. With this approach however, the initial cutting abilities of the wire, ca. twice as high as at its lifetime end, are not fully utilised (Figure 2).

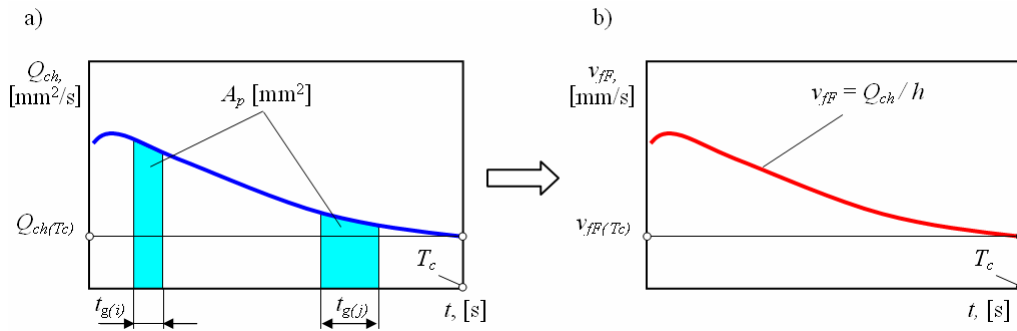


Fig. 2. Changes of (a) instantaneous capacity Q_{ch} and (b) principal cutting time t_g and cutting speed with constant pressing force during the wire lifetime T_c

In the kinematic system with constant feed rate (Figure 1b), the principal operation time is calculated from the formula (1), and the permissible feed rate (cutting rate) v_{fdop} is calculated from the formula

$$v_{fdop} = \frac{Q_{ch}(T_c)}{h}, \quad [\text{mm/s}] \quad (2)$$

where $Q_{ch}(T_c)$ is instantaneous wire cutting capacity at the moment of meeting the dullness criterion in mm^2/s .

The most favourable results of abrasive wire cutting, with respect to accuracy and efficiency, are obtained with constant pressing force. The pressing force is selected to obtain sufficient cutting accuracy that depends mostly on the wire deflection and, at the same time, it must not be so large to break the wire (fatigue failure).

Performing rectilinear wire cutting with constant pressing force is relatively easy, e.g. by gravitational drive (weight, strand, roller). In the case of curvilinear cutting, especially of closed contours, applying constant pressing force is much more difficult and requires using adaptative control systems or manual guiding of the workpiece.

In a kinematic system with constant pressing force, the principal cutting time t_g depends on cutting speed v_{fF} changing along the lifetime T_c and conditioned by variations of the wire cutting properties (Figure 2).

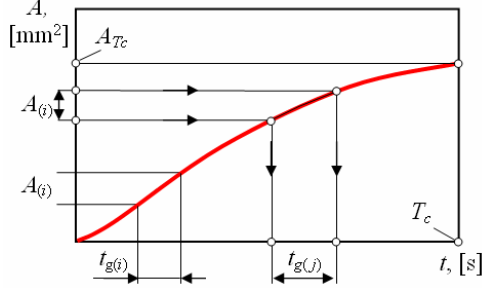


Fig. 3. Change of principal cutting time t_g during the wire lifetime T_c

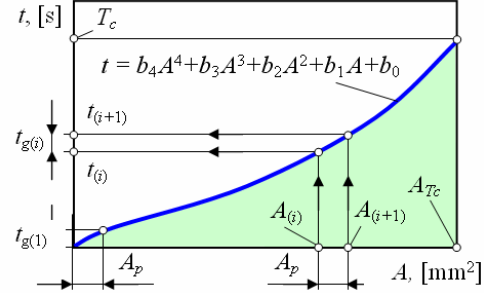


Fig. 4. Time of cutting-out a specific area during the wire lifetime (inverse function $(A)^{-1}$)

Methodology of determining the principal cutting time t_g with known $Q_{ch}(t)$ function is as follows:

1. Determining the relationship $A(t)$ (3) (Figure 3),

$$A(t) = \int Q_{ch} dt, \quad [\text{mm}^2]. \quad (3)$$

2. Determining the inverse function to $A(t)$

Using the $A(t)$ function to determine the principal machining time $t_{g(i)}$ for a specific area $A_{(i)}$ of the processed workpiece is rather complicated. It is much easier to use the inverse function (Figure 4).

The existence condition of the inverse function is that the integrand $A(t)$ (Figure 3) is a multi-valued function in the interval $\langle 0; T_c \rangle$, which in this case means that it is monotone.

3. Calculation of the principal time of the i -th operation

$$t_{g(i)} = t(A_{i+1}) - t(A_i), \quad [\text{s}]. \quad (4)$$

It results from the diagram in Figure 4 that, for identical cut area A_p , the principal machining time will depend on the wire wear condition.

The presented procedure includes the following assumptions:

- the principal machining time of one workpiece is calculated,
- the principal machining time is shorter than the wire lifetime,
- the machining is performed with one wire.

To determine efficiency and costs of wire cutting in more complex industrial conditions, it is necessary to build some general functions. First, the relationship is presented for the principal cutting time of one workpiece with the area $A_p = hl$, calculated as average value for a product lot n_{sz} and assuming that the task can be executed by a few cutting wires.

The work task is presented in Figure 5.

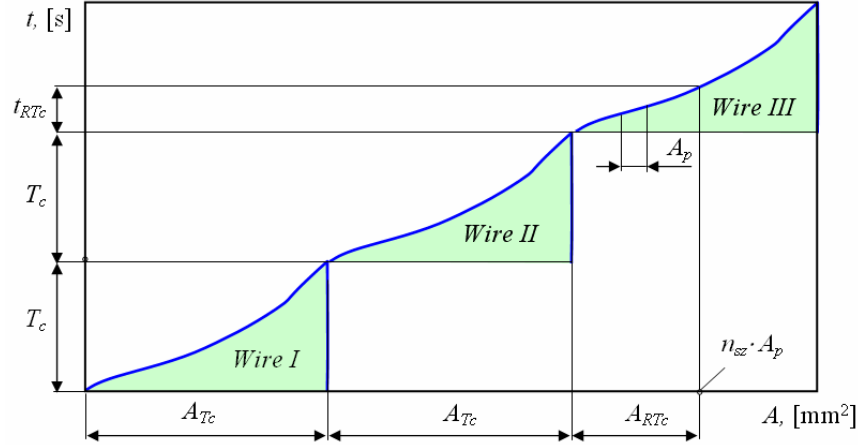


Fig. 5. Time for cutting a defined cut area of all workpieces ($n_{sz} \cdot A_p$), which requires using cutting abilities of more than two wires

The total number n_{intT_c} of wires required for production of n_{sz} pieces is calculated from the relationship

$$n_{intT_c} = \text{int} \left(\frac{n_{sz} A_p}{A_{T_c}} \right), \quad [\text{pcs}] \quad (5)$$

where A_{T_c} is total area that can be cut with one wire, mm^2 .

The remaining area A_{RT_c} to be cut out with the last wire is

$$A_{RT_c} = n_{sz} A_p - n_{intT_c} A_{T_c}, \quad [\text{mm}^2]. \quad (6)$$

The working time t_{RT_c} of the last wire for cutting out the remaining area A_{RT_c} (Figure 5) is

$$t_{RT_c} = t(A_{RT_c}), \quad [\text{s}]. \quad (7)$$

The average principal cutting time for the whole product lot (Figure 5) is

$$t_g = \frac{n_{intT_c} T_c + t_{RT_c}}{n_{sz}}, \quad [\text{s}]. \quad (8)$$

Having calculated the average principal cutting time, one can calculate the average operation time t_{sz} [6]

$$t_{sz} = \frac{60 t_{pz}}{n_{sz}} + \left[60 t_p + t_g \left(1 + \frac{t_{zn}}{T_c} \right) \right] (1 + k_u), \quad [\text{s}] \quad (9)$$

where:

t_{pz} – lead-in/lead-out time, in min,

t_p – auxiliary time in min,

t_{zn} – tool change time in min,

k_u – index of the supplementary time.

The efficiency W is the inverse of the unit operation time t_{sz}

$$W = t_{sz}^{-1}, \quad [\text{pcs/s}] \quad (10)$$

The average cutting operation cost K_j can be calculated as

$$K_j = \frac{K_m + K_{Lm}}{3600} t_{sz} + \frac{K_N}{T_c} t_g, \quad [\text{EUR/pc}] \quad (11)$$

where:

K_m – operational machining station cost in EUR/h,

K_{Lm} – operator's pay in EUR/h,

K_N – wire cost in EUR.

The first segment of the relationship (11) considers the machining station cost and the operator's pay per average operation time t_{sz} . The second segment considers the wire cost related to the number of pieces processed during the wire lifetime.

The presented formula for unit operation costs is related to the most frequently occurring cases, when the abrasive wire not completely worn on machining the last piece in the lot can be used in another machining task. Thus, a fraction of the wire value is included in the tooling costs, adequately to its utilisation degree [6].

3. Example of determining efficiency and costs of abrasive wire cutting

The efficiency and costs of diamond wire cutting were determined with the following conditions and parameters: kinematic cutting with constant pressing force $F_f = 2$ N, rectilinear cutting of silicate ceramic material, cut section $h \times l = 6 \times 12$ mm, cutting speed $v_c = 8.5$ m/s, wire tension force $F_n = 10\text{--}12$ N, cutting without cooling, $K_N = 333$ EUR, $K_{Lm} = 3.33$ EUR/h, $K_m = 10$ EUR/h, $n_{sz} = 1000$ pcs, $t_{zn} = 2$ min, $t_{pz} = 10$ min, $t_p = 0.5$ min.

On the ground of the experimental results [2], the time relationship of the instantaneous cutting capacity $Q_{ch}(t)$ within the entire wire lifetime was determined, as shown in Figure 6.

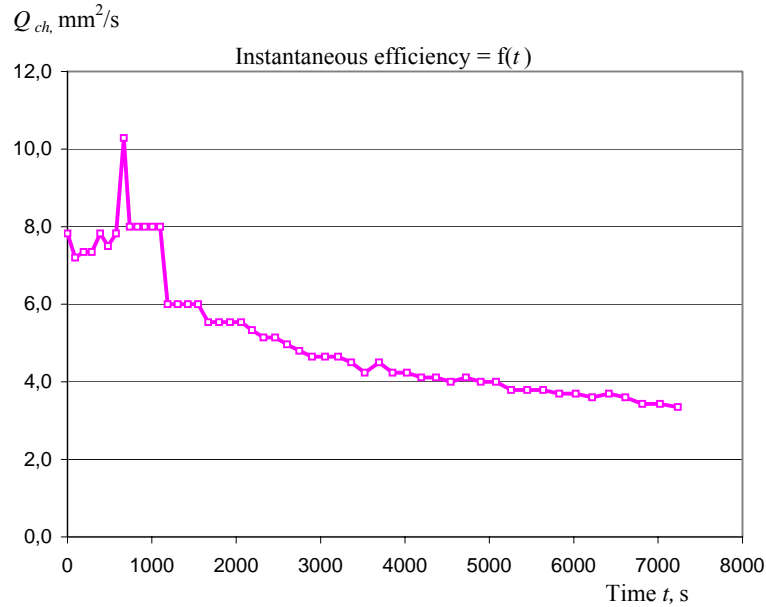


Fig. 6. Relationship between instantaneous cutting capacity of a wire and its working time

Having integrated the relationship $Q_{ch}(t)$, one obtain the relationship between the cut area and the wire working time $A(t)$. Results of numerical integration using a simple Excel datasheet are shown in Figure 7.

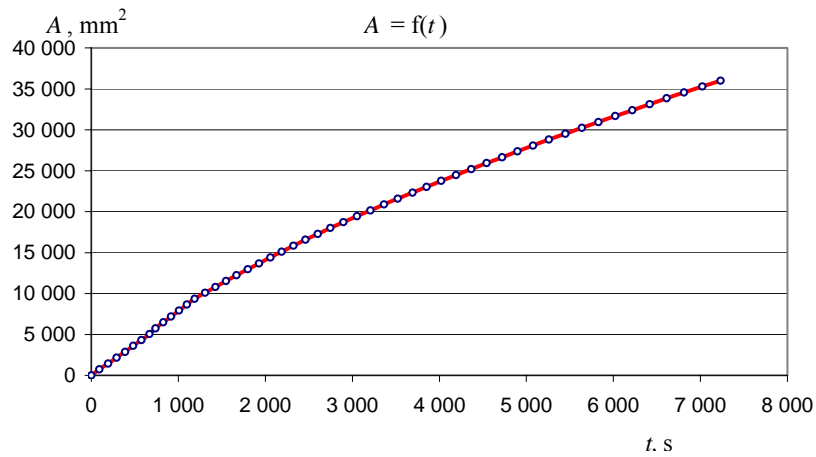


Fig. 7. Relationship between cut area and the abrasive wire working time

The function shown in Figure 7 is a multi-valued function, which allows finding its inverse function. Inverting a function written in an algebraic form is very difficult and

in many cases impossible or giving many solutions. However, if the relationship is written in a tabular form, it can be inverted using simple matrix calculus. The inverse function is shown in Figure 8. The regression coefficients of a second-degree polynomial describing the relationship in Figure 8 were determined using the least square method.

$$t = 0.00000275A^2 + 0.1014A + 39.67, \quad [\text{s}] \quad (12)$$

In Figure 8, experimental results are marked with dots and the regression function with a solid line. The equation describes the experimental results in sufficiently exact way.

The machining function given by (12) and shown in Figure 8 describes variable cutting properties during the wire lifetime in an indirect way. Knowing this function is necessary for determining efficiency and costs of abrasive wire cutting.

To determine the average operation time per piece t_{sz} or unit costs K_j , one should subsequently insert the related data to the formulae (6–12).

For the data listed at the beginning of this section, the calculated values are:

- average operation time $t_{sz} = 50.78$ s/pc,
- average cutting capacity $W = 0.0197$ pc/s,
- unit operation cost $K_j = 0.66$ EUR/pc.

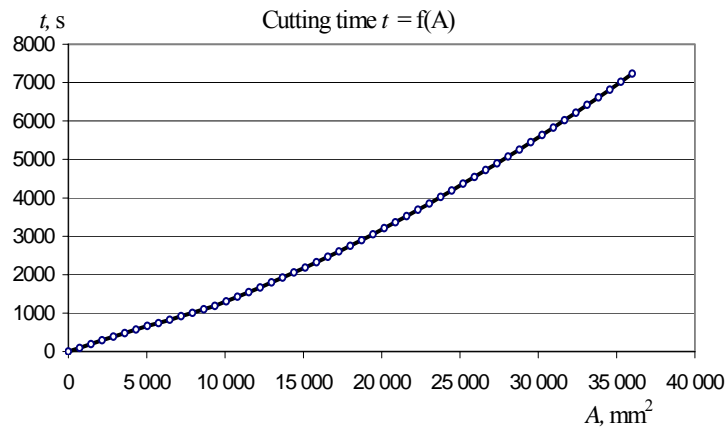


Fig. 8. Relationship between cutting time and cut area

6. Conclusions

Methodology of determining the time, efficiency and costs of cutting with diamond-coated abrasive wire were presented, as well as methodology of determining the optimum wire dullness criterion. The results were verified by an experimental example. The presented mathematical formulae used for transformation and calculation of the required relationships are mathematically simple and can be easily determined by

means of datasheets, e.g. in Microsoft Excel program, although the applied optimisation procedures are complex.

Acknowledgments

This work has been developed in the project “Theoretical background and cutting optimization of hard to machining materials with wires of different construction” (reference 5T07D01424) subsidized by the Ministry of Science and Higher Education of Poland.

References

- [1] Ciałkowska B., Kołodziej M., Szymkowski J.: *State of glass surface outer layer after cutting with diamond wire of different construction, Influence of engineering on a state of the surface layer*, International Conference WW '02, Gorzów Wlkp.–Poznań, 13.11.2002.
- [2] Ciałkowska B., Cichosz P.: *Theoretical background and cutting optimization of hard to machining materials with wires of different construction*, Reports of Institute of Production Engineering & Automation, Ser. SPR No. 9, 2006, pp. 76–92.
- [3] Ciałkowska B., Dudek K.: *Selected thermal questions of cutting hardly workable materials with diamond wire*, Drives and control, Vol. 9, 2007.
- [4] Ciałkowska B.: *Significance of wire cutting in shaping of hard to machining materials*, Manufacturing '04. II International Conference. Poznań, 4–5 November, 2004.
- [5] Cichosz P., Rosienkiewicz P.: *Determination of optimum process parameters in belt grinding*, XVIII Scientific School of Abrasive Machining, Wrocław – Szklarska Poręba, 16th September, 1995.
- [6] Cichosz P.: *Effectiveness of the cutting-forming of axially symmetric workpieces in integrated manufacturing*, Scientific Papers of Institute of Mechanical Engineering and Automation of the Wrocław University of Technology, Monographs No. 21, Wrocław, 1998, pp. 30–76.
- [7] Kray D., Baumann S.: *Wafering research at Fraunhofer ISE*, 15th Workshop on Crystalline Silicon Solar Cells and Modules, Materials and Processes, Vail, Colorado, 2007.
- [8] Clark W.I., Shih, A.J., Hardin C.W., Lemaster R.L., McSpadden S.B.: *Fixed abrasive diamond wire machining–part I: process monitoring and wire tension force*, International Journal of Machine Tools and Manufacture, Vol. 43, Issue: 5, April, 2003, pp. 523–532.
- [9] Clark W., Shih A., Lemaster R., McSpadden S.: *Fixed abrasive diamond wire machining–part II: experiment design and results*, International Journal of Machine Tools and Manufacture Vol. 43, Issue: 5, April, 2003, pp. 533–542.
- [10] Ozelik Y., Polat F., Bayram F., Ay A.M.: *Investigation of the effects of textural properties on marble cutting with diamond wire*, International Journal of Mechanics and Mining Sciences, Vol. 41, 2004, pp. 398.

Ekonomiczne aspekty cięcia struną diamentową

Cięcie za pomocą diamentowych strun ma duże znaczenie w kształtowaniu materiałów trudnoobrabialnych. Zmienna wydajność cięcia może komplikować kinematykę napędu posuwu obrabiarek, jeśli chce się wykorzystać pełne możliwości obróbkowe struny. Zmniejszająca się wydajność cięcia zwiększa koszty operacji oraz utrudnia podjęcie decyzji, kiedy wy-

mienić strunę na nową. Wyniki badań zweryfikowano przykładem doświadczalnym. Przedstawione formuły matematyczne, służące do wymaganych przekształceń i obliczeń zależności, mają prostą budowę matematyczną dającą się łatwo zastosować w warunkach przemysłowych. Opracowana metodyka ma ogólną formułę.



Structure and hardness changes in welded joints of Hardox steels

S. FRYDMAN, Ł. KONAT, G. PEKALSKI

Wrocław University of Technology, Wybrzeże Wyspiańskiego 27, 50-370 Wrocław

In the article, the structure and change in hardness of the welded Hardox 400 and Hardox 500 steels have been presented. It has been shown that structures of lower wear resistance are being created as a result of welding those materials in the “as delivered” state (i.e. with the tempered martensite structure) within the heat-affected zones. They are as much as up to 90 mm wide, and that causes their non-uniform and fast wear in the anticipated applications. Based on microscopic tests and hardness measurements a method of thermal joints treatment has been proposed, consisting in their hardening and low-temperature tempering (self-tempering) at the heat-affected zones. It leads to reproduction of that area structure, similar to the native material structure. In the laboratory conditions, a heat treatment differing from the usual practice (stress-relief annealing or normalizing) has not led to welding incompatibilities (cracks).

Keywords: *wear-resistant alloys, martensitic steels, welded joints, hardness changes, structures*

1. Introduction

Based at test results concerning Hardox 400 and Hardox 500 steels collected among others in [1], a proposal has been formulated of using those materials in the surface mining machinery construction. The own test results [2–4] confirm good weldability of the materials and very high strength properties of the joints obtained. As a result of heat processes during welding, damage is being introduced into the as delivered structures in the heat-affected zones (tempered martensite). It introduces significant change in such area hardness, as well as local drop in wear resistance. Similar phenomena are being observed in structural components cut out of metal sheets using welding methods.

Significance of such phenomena is high when intending to use Hardox steel plates for brown coal excavator parts, which are exposed to wear in the dynamic load conditions (chutes, hoppers, dumpers and scoop structure elements). The significance is even higher, because they are usually being fixed to the main structure by welding. Unfavourable structure and joint hardness appearing in low-carbon and low-alloyed steels may be reversed by heat treatment of such joints (Figure 1). In case of toughened steel, martensitic steel, as well as hyperquenched and aged aluminum alloys, the issues look different from the usual practice.

In the works [7, 8] they have been presented in relation to toughened steels in the following statements:

- in the heat-affected zone a problem of soft layer appears, which determines the strength of the whole structure,
- in the heat-affected zone of steel joints, hardened and tempered before welding, changes appear which lead to creation of tempering zones of lowered hardness and tensile strength.

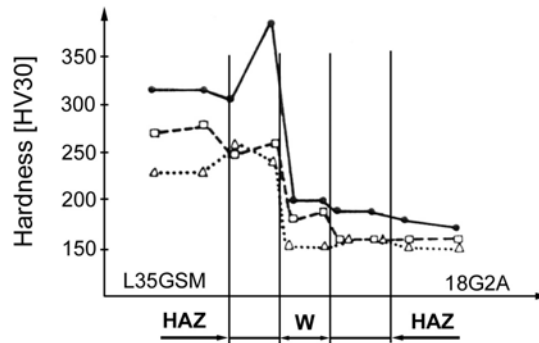


Fig. 1. Hardness distribution in welded joints of the L35GSM cast steel with 18G2A steel:
 ● – as delivered, □ – after stress relief annealing, Δ – after normalizing, W – joint area,
 HAZ – heat-affected zone [5, 6]

Authors of the works [7, 8] and [9–11] state, however, that due to the proper chemical composition of materials and proper selection of welding conditions and parameters, it is possible to obtain structures of similar material properties to the base one in the heat-affected zone, without additional efforts. In case of welding with limited line energy the “soft layer” is very narrow and the joint exhibits no clear reduction of mechanical properties. This is interpreted as “reinforcing” activity of neighbour structural areas, as a result of three-axial stress creation in that zone.

Table 1. Chemical composition of Hardox 400, Hardox 500, HTK 700H and HTK 900H steels

Material	C	Si	Mn	P	S	Cr	Ni	Mo	B
	Maximum values [%]								
Hardox 400	0.320	0.700	1.600	0.025	0.010	0.300	0.250	0.250	0.004
Hardox 500	0.300	0.700	1.600	0.025	0.010	1.000	0.250	0.250	0.004
HTK 700H	0.180	0.450	1.400	0.025	0.010	0.500	0.300	0.030	0.002
HTK 900H	0.180	0.450	1.500	0.025	0.010	1.000	0.300	0.040	0.003
AR 400	0.240	0.700	1.700	0.025	0.010	1.000	0.700	0.500	0.004

Table 2. Structural properties of investigated steels

Material	Structure
Hardox 400	martensitic
Hardox 500	martensitic
HTK 700H	martensitic – bainitic
HTK 900H	martensitic
AR 400	martensitic

Hardox Steels, as well as HTK steels (Table 1 and 2) are well weldable materials with low, or depending on conditions, crack sensitivity (susceptibility) (Figure 2). In the as delivered state they have the structure of tempered martensite. According to the producer data for those materials the hardness changes are as presented in Figure 3. As it comes out of the graph, hardness reduction in the heat-affected zone could go as high as 65% in relation to materials in the as delivered state. The extension of such area of hardness reduction is not being determined by the steel producer. However, the problem itself is being recognized in the form of recommendation for the zones to be padded for hardening.

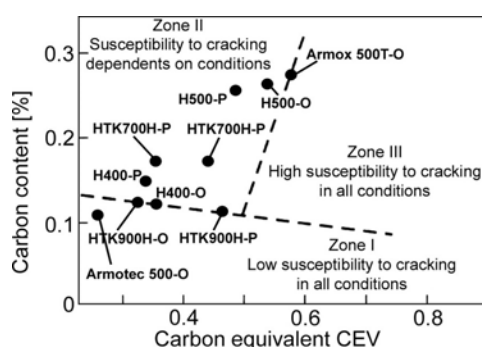


Fig. 2. Crack sensitivity of welded joints in Hardox 400 and Hardox 500, as well as HTK 700H and HTK 900H steels, for sheets of 8 mm thickness as a function of carbon contents and carbon equivalent:
P – according to a producer data, W – according to own chemical analysis [3, 12]

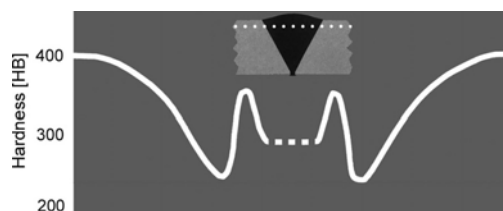


Fig. 3. Hardness change diagram in the welded joint of Hardox 400 steel [13]

However, the method does not solve the problem, as the hardening process of padding must cause new zones of unfavourable structural changes shifted toward edges of padding weld. The following aims of the current studies emerge in the context of the presented information:

- identification of microscopic structure in welded joints of Hardox 400 and Hardox 500 steels in the as delivered state and determination of structure and hardness change extension caused by welding,
- introduction of such structural transformations in joints by heat treatment as to eliminate the changes to the maximum degree.

2. Study results

2.1. Welding conditions

Joints in Hardox steels have been performed using technology of submerged arc welding (SAW), considering welding materials and parameters recommended by producer. As welding material the Multimet IMT9 ϕ 3 mm (carbon contents 0.09 %) filler wire and Lincoln Electric FX 780-25 flux have been used. The samples were made of Hardox steel sheets of 500×300 dimensions (8 mm thickness) joined with double-sided weld with the following parameters providing for correct material penetration:

- minimum current for the first joint layer $I_1 = 300$ A,
- minimum current for the second joint layer $I_2 = 500$ A,
- electric arc voltage for both joint layers $U = 30$ V,
- constant welding speed $v = 0.35$ m/min,
- maximum linear energy: 2.57 kJ/mm.

Table 3 presents real chemical compositions of the welded steels. Their comparison with producer data indicates for lower contents of alloy additions. This justifies for more favourable location of points determining crack sensitivity of welded steels (Figure 2).

Table 3. Real chemical compositions of the welded Hardox steels and filler wire

Material	C	Si	Mn	P	S	Cr	Ni	Mo	B
Hardox 400	0.120	1.050	0.34	0.006	0.001	0.240	0.040	0.017	0.002
Hardox 500	0.260	0.750	0.200	0.005	0.005	0.700	0.05	–	0.001
IMT9 Wire	0.090	0.140	1.000	–	–	–	–	–	–

Table 4. Heat treatment pattern and parameters for Hardox 400 and Hardox 500 steels

Pos.	Sample marking		Heat treatment pattern	Heat treatment parameters
	Hardox 400	Hardox 500		
1	I – 1	II – 1	As delivered state	–
2	I – 4	II – 4	Hardening	930°C/20min/cooling in H ₂ O
3	I – 6	II – 6	Hard./H ₂ O/Temp.	Temp. 200°C/2h/air cooling
4	I – 7	II – 7	Hard./H ₂ O/Temp.	Temp. 300°C/2h/air cooling

Table 4 presents methods and parameters of heat treatments applied to the joints tested. They were performed in the as delivered state (pos. 1), hardened after welding (pos. 2) or after hardening and tempering (pos. 2 and 3). Tempering temperature limitation to 300 °C results from hardness and structure tests performed for the Hardox 400 and Hardox 500 steels within the tempering temperature range from 200 °C to 700 °C. Up to the tempering temperature of 300 °C the steels preserve average hardness: 363 HV10 – Hardox 400 and 428 HV10 Hardox 500. From the tempering temperature of 400 °C their hardness drops fast, which excludes them from use in the wear conditions.

2.2. Joint structure and hardness changes in the as delivered state

Figure 4 presents exemplary structure of Hardox 500 steel as delivered. Joint welding has introduced apparent changes and diversification in structure (Figure 5). Graphs of hardness measurement (Figure 6 and 7) prove the extension of lowered hardness zones. In case of Hardox 400 steel the zone is 70 mm wide, and for Hardox 500 it goes up to as much as 90 mm.

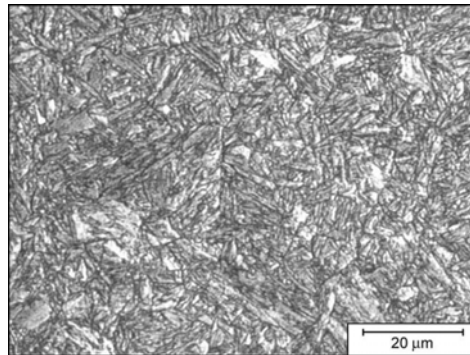


Fig. 4. Microstructure of Hardox 500 steel “as delivered”. Tempered martensite without clear grain orders of the previous austenite. Mi1Fe etched, LM [2]

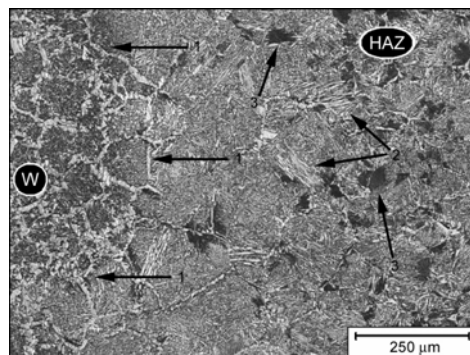


Fig. 5. Structure of welded joint of Hardox 500 steel in the fusion zone: W – weld material, HAZ – heat-affecting zone. Arrows (1) indicate weak outline of the fusion area.

In the heat affecting zone a structure of post-martensitic orientation with areas of bainite (2) and troostite (3) is clearly visible. Widmanstätten’s structures typical for significant over-cooling have been observed locally. Mi1Fe etched, LM [2]

Also, the content of carbon in the joint material is clearly higher than it could result from Table 3. It demonstrates itself with high quantity of fine-dispersive pearlite in the joint material (Figure 5, zone W). A lack of welding incompatibilities is also a result of macro- and microscopic observations of the tested joints.

Welded joint strength test results in the as delivered state have shown an average joint strength of Hardox 400 steel equal to 615 MPa, and for Hardox 500 the strength was 634 MPa. These are very high values and they constitute about 60% of the yield point for Hardox 400 and about 50% for Hardox 500 steel.

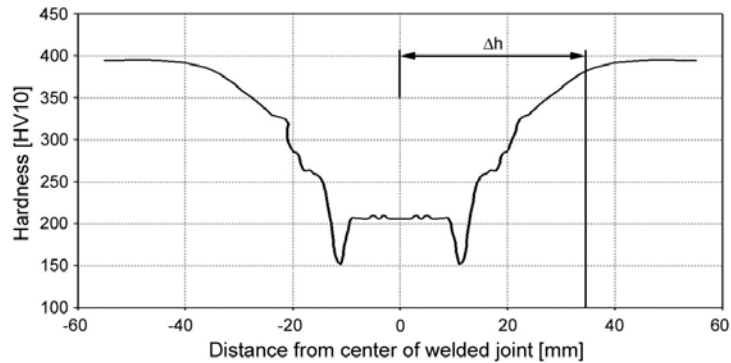


Fig. 6. Hardness changes in welded joint of Hardox 400 steel in the as delivered state:
 $\Delta h \approx 35$ mm, weld hardness ≈ 210 HV10

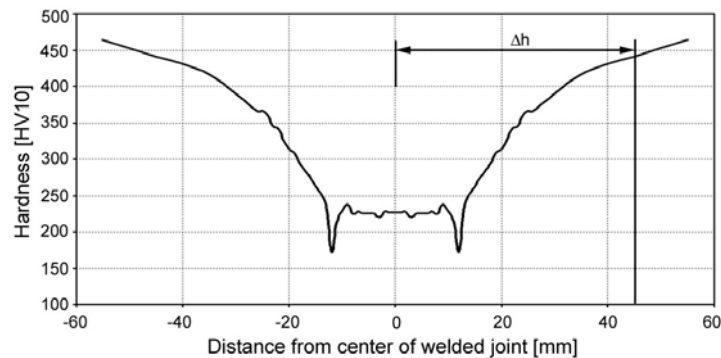


Fig. 7. Hardness changes in welded joint of Hardox 500 steel in the as delivered state:
 $\Delta h \approx 45$ mm, weld hardness ≈ 230 HV10

2.3. Structures and hardness changes in joints after heat treatment

Overview of hardness changes and joint structures after heat treatment is presented in Figures 8–16. Macro- and microscopic studies have not shown that joint failures in the form of cracks appeared as a result of the heat treatment. All joint zones (marked in Figure 5) have transformed structurally by changing towards the native material structure in the as delivered state. Data concerning extension of the lowered hardness zones have been collected in Table 5. Minimum values of hardness measurements in the as delivered state have been assumed as border of that zone.

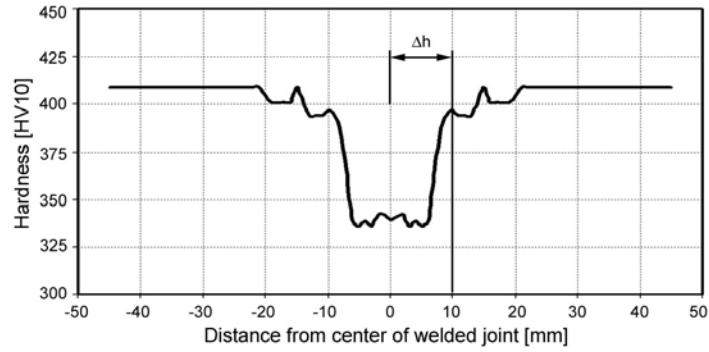


Fig. 8. Hardness changes in welded joint of Hardox 400 steel after hardening. Maximum hardness in the HAZ ≈ 410 HV10. Minimum hardness of the weld material ≈ 340 HV10

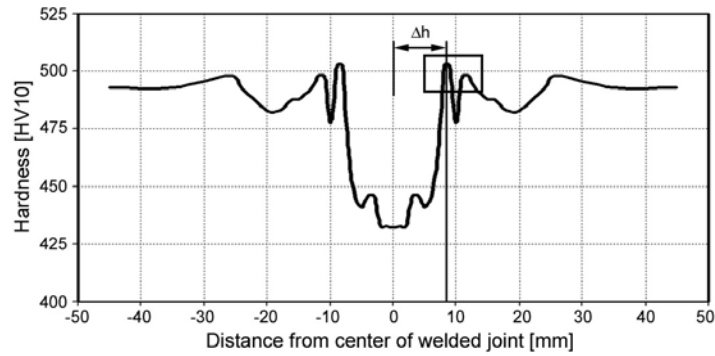


Fig. 9. Hardness changes in welded joint of Hardox 500 steel after hardening. Maximum hardness in the HAZ ≈ 503 HV10. Minimum hardness of the weld material ≈ 430 HV10

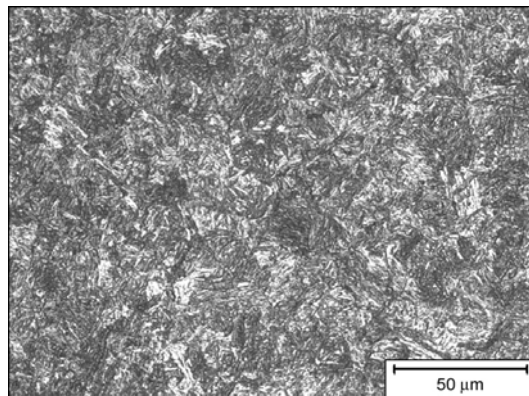


Fig. 10. Structure of welded joint of Hardox 500 steel after hardening from the area marked with frame at Figure 9. Martensitic structure of maximum hardness ≈ 503 HV10. Mi1Fe etched, LM

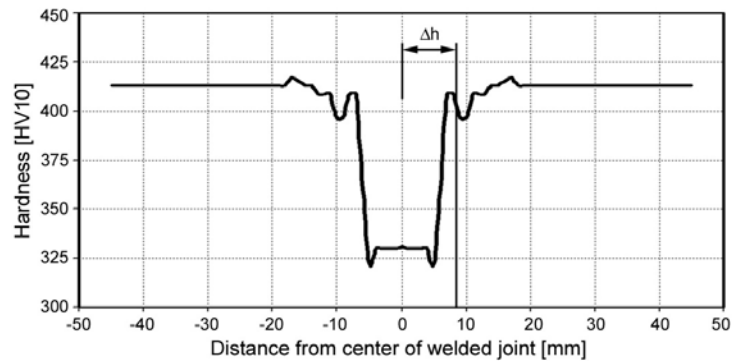


Fig. 11. Hardness changes in welded joint of Hardox 400 steel after hardening and tempering at 200 °C temperature. Maximum hardness in the HAZ \approx 416 HV10

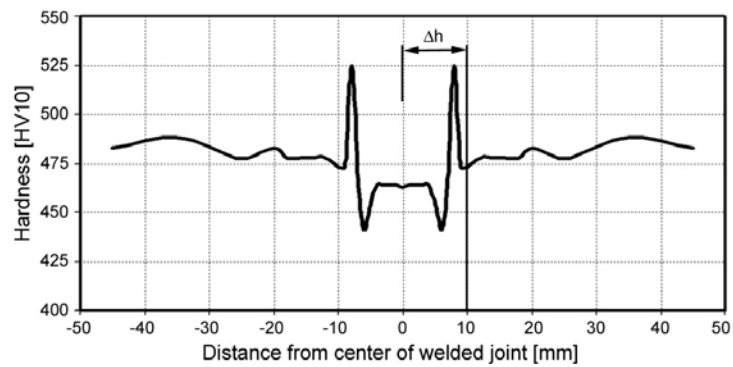


Fig. 12. Hardness changes in welded joint of Hardox 500 steel after hardening and tempering at 200 °C temperature. Maximum hardness in the HAZ \approx 523 HV10

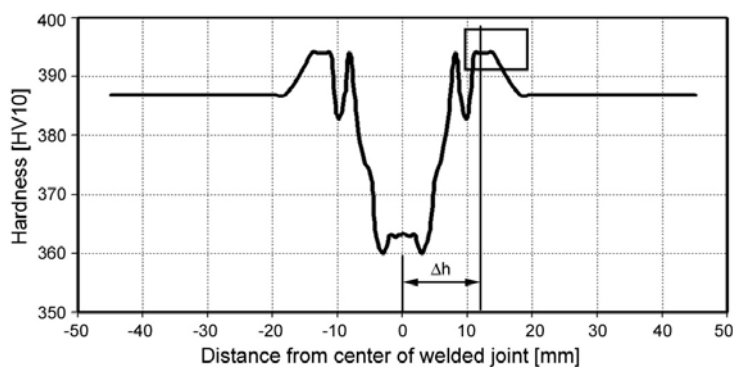


Fig. 13. Hardness changes in welded joint of Hardox 400 steel after hardening and tempering at 300 °C temperature. Maximum hardness in the HAZ \approx 393 HV10

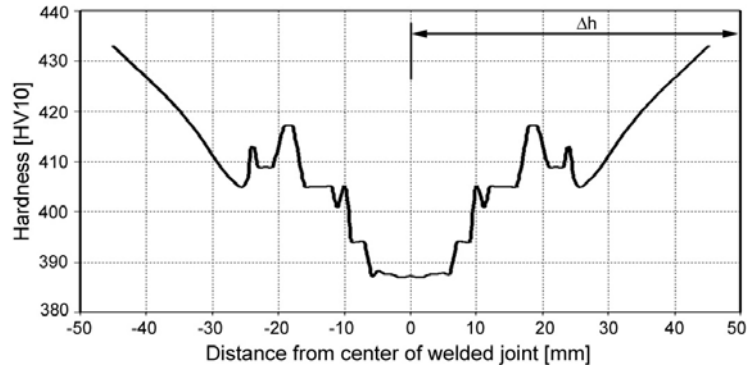


Fig. 14. Hardness changes in welded joint of Hardox 500 steel after hardening and tempering at 300 °C temperature. Maximum hardness in the HAZ \approx 417 HV10

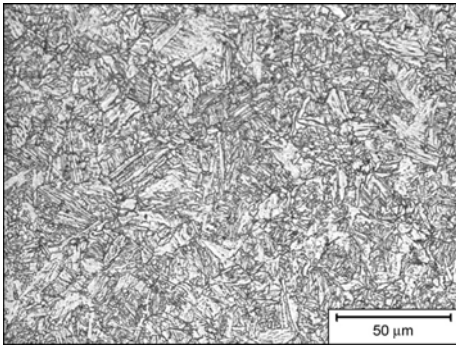


Fig. 15. Material microstructure in welded joint of Hardox 400 steel after hardening and tempering at 300 °C temperature. Sorbitic type structure. Mi1Fe etched, LM

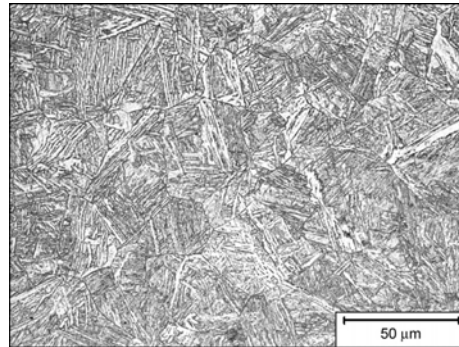


Fig. 16. Microstructure of heat-affected zone in welded joint of Hardox 400 steel after hardening and tempering at 300 °C temperature. Microstructure from area marked with frame at Figure 13. Mi1Fe etched, LM

3. Summary

Measurement results in hardness change have been collected in Table 5. The following observations result from the data:

a) Width of the lower hardness zone in HAZ in relation to that zone width in the as delivered state has been significantly limited as the result of all patterns of heat processing. Besides the case of hardening and tempering of the Hardox 500 steel at the 300 °C temperature, the areas of lowered hardness have been narrowed by 3 to 6 times.

b) As a result of heat treatment the hardness of weld material has increased significantly. In extreme cases they changed by 70% for Hardox 400, and by 90% for Hardox 500 steel. This indicates that also those areas should present higher wear resistance in relation to the as delivered state.

c) In case of welding the Hardox 500 steel hardened and tempered at 300 °C temperature the width of lower hardness zone is similar to that as delivered. Essential difference, however, constitutes a flattening of hardness change between native material and HAZ and weld material hardness. After heat treatment the $\Delta HV_{10} \approx 290$. That indicates also for probable increase in wear resistance in the welded joint structure change zone.

Table 5. Comparison of hardness measurement results

Pos.	Welded joint state	Material	Δh	HV_W	HV_{MAX}	HV_{FZ}
			[mm]	HV10	HV10	HV10
1	As delivered	Hardox 400	35	210	375	250
		Hardox 500	45	230	440	280
2	Hardened	Hardox 400	10	340	410	395
		Hardox 500	8	430	503	503
3	Hardened and tempered at 200 °C	Hardox 400	8	330	416	410
		Hardox 500	10	440	523	523
4	Hardened and tempered at 300 °C	Hardox 400	12	363	393	393
		Hardox 500	60	385	□500	417

Δh – width of lowered hardness zone, HV_W – weld material hardness,
 HV_{MAX} – maximum hardness in HAZ, HV_{FZ} – maximum hardness in fusion zone

Microscopic tests have confirmed changes in structure of particular zones of welded joints in relation to their structures at the as delivered state. The material shows structural transformations consisting in:

a) Change in weld material structure from quasieutectoid with ferrite halo at grain borders (Figure 5, area W) into a structure of low-carbon tempered martensite (Figure 15).

b) Obtaining the structure of tempered martensite in the whole heat-affected zone (Figure 16). The structure is very similar to that of Hardox 500 steel in the as delivered state (Figure 4). Moreover, as a result of heat treatment the structure variation in the fusion zone has been eliminated.

In the welded Hardox 400 steel the structural changes in various conditions of heat treatment show departures from joint structures of Hardox 500 steel. They consist in:

a) Sorbitic, and not martensitic structure of weld material.

b) Narrow zone of fine ferrite grains (from the Hardox 400 steel side) in the fusion zone.

c) Martensite structure with more advanced tempering process at the heat-affected zone than in case of Hardox 500 steel (Figure 16).

From the data contained in Table 3, it results that difference in carbon density between Hardox 400 steel and filler wire amounts to 0.03%, and between Hardox 500 steel and the wire to 0.17%. During welding, the carbon diffusion fluxes from Hardox steel to the created weld are being initiated. That way, the weld material is being enriched in that hardness improving element. In case of welding sheets of Hardox 500 steel this leads to martensitic type structures also in the weld material. Lowering the

carbon contents in the fusion zone (from the Hardox 500 steel side) is not, however, that intensive as not to allow reproduction during the heat treatment of the structure similar to the native material as delivered. In Hardox 400 steel the saturation of weld material with carbon could be lower as a result of its smaller contents in that steel. Thus, hardenability of the weld material is insufficient for obtaining the martensitic structure. A thesis could also be formulated concerning presence of a narrow strip of equilibrium ferrite (from the Hardox 400 side) in the fusion zone. From that zone, plenty of carbon passed to the weld material and, as a result, its hardenability was lowered. The effect of that phenomenon is lack of low-carbon martensite in that zone. The above assumptions could be confirmed by the results of spectral analysis of chemical composition of the weld materials. They have shown:

- average carbon contents higher by several hundredths of percent from 0.09,
- higher carbon contents in joint connecting sheets of Hardox 500 steel than that of Hardox 400.

The laboratory results indicate that in case of steel with martensitic structure a correction of joint hardness and structure is possible by means of hardening and tempering. This concerns the Hardox 400, Hardox 500 steels and, undoubtedly, the HTK 900H steel. That last one in the as delivered state has structure and hardness similar to Hardox 400. Proposals of applying such heat treatment to welded joint have to arouse some controversies and causes some technological problems. Usually (see Figure 1), the relief or normalizing annealing processes are being applied to welded joints. It has been proposed that during applying the last layer of weld a water jet followed an electrode causing hardening of the heat-affected zone (similar solution to the surface hardening). The cooling process would terminate at such point as to allow for self-tempering by heat cumulated in the material. Trials of welding and heat treatment of excavator scoop knives will be conducted in the second half of 2008. The proposal verification would follow during the operating experiment. Before such tests, metallographic studies of welded joints made at structure components of shapes and sizes corresponding to the scoop knives will be conducted.

Hardox steels, and their Polish equivalents – HTK steels, may find far wider application than before in the construction of basic machines for brown coal mining. It simply comes out from their very high mechanical properties and uniform structure at the sheet thickness (even exceeding 100 mm). The second of the features is very special one because, as opposed to the non-homogeneous padded layers, it allows for precise prediction of durability (the higher one from padding weld) of various type lining plates. As shown in the paper [1], using the Hardox steel in real conditions consists in uniform wear, without cracks and local thickness change. That is why they could be used until complete wear. The only areas of intensive wear of such steel lining are joints (stack welding) with the main structure. Should the failure be eliminated in scoop lining and knives, a new, economically justified application area of those materials emerge [1].

Justification and inspiration for works at improving the structure and properties of welded joints in Hardox and HTK steels may also be found among the modern materials for power industry. Martensitic steels, type 9-12% Cr (containing boron), are also in consideration. Since developing the first of them (TAF steel from Japan, middle of seventies in the 20th century), attempts of applying it to superheater pipes were restrained by its low elastic properties and inadequate weldability. It happened so even despite its excellent resistance to creep. It required subsequent years to develop P91 and P92 steels and apply them to steam superheater header (e.g. at the Opole Power Plant BOT). As an effect, the weight of piping dropped by some 30% and significant investments and start-up savings were achieved [14]. It is not unlikely that similar way the technology of welded joint heat processing for Hardox and HTK steels should pass for the anticipated applications.

References

- [1] Cegiel L., Konat Ł., Pawłowski T., Pękalski G.: *Hardox Steels – New generations of construction materials for surface mining machinery*, Brown Coal, Bogatynia, No. 3, 56, pp. 24–29.
- [2] Konat Ł., Pękalski G., Oskwarek M.: *Macro and microstructural properties of welded joints of Hardox 400 and Hardox 500 steels*, XIX Scientific Conference „Development Problems of Working Machines”, Technical Magazine, Zakopane, January 2006.
- [3] Oskwarek M.: *Structural features and susceptibility to cracking of welded joints of Hardox 400 and Hardox 500 steels*, Conference Proceedings, IV Scientific Conference of Students, Wrocław University of Technology Publishing House, Wrocław 2006.
- [4] Bugłacki H., Smajdor M.: *Mechanical properties of abrasion – resistant Hardox 400*, Advances in Material Science, Vol. 4, No. 2, 2003.
- [5] Haimann R., Krajczyk A., Pękalska L., Pękalski G.: *Analysis of strength changes and development of technology for optimal annealing of welded parts (caterpillar girders, caterpillar plates, a.s.o.)*, IMMT Report, series SPR 6, Wrocław University of Technology, 1986.
- [6] Haimann R., Krajczyk A., Pękalska L., Pękalski G.: *Influence of relief annealing on the structure and properties of cast steel joints with 18G2A and 12G2ANb steels*, Welding Technology Overview, 1990.
- [7] Tasak E.: *Metallurgy and structural metallurgy of welded joints*, Script AGH Kraków, 1985.
- [8] *Engineer Handbook – Welding Technology*, T1, WNT, Warszawa 2003.
- [9] Brooks J.A., Garrison Jr. W.M.: *Weld Microstructure Development and Properties of Precipitation-Strengthened Martensitic Stainless Steels*, Welding Journal, Aug. 1999.
- [10] Li D., Lu B., Zheng X.: *Fatigue Crack Initiation and Propagation in Butt Joint Welds of an Ultrahigh-Strength Steel*, Welding Journal, February 1993.
- [11] Akselsen O.M., Rorvik G., Onsoien M.I., Grong O.: *Assessment and Predictions of HAZ Tensile Properties of High-Strength Steels*, Welding Journal, September 1989.

- [12] Łętkowska B.: *Material studies of HTK – 700H, HTK – 900H and AR400 steels and potential of their application in surface mining machinery construction*, Master Diploma Thesis, Work Tutor G. Pękalski, PhD, 2007.
- [13] Welding. Hardox, Weldox, Information Materials of the SSAB-Oxelösund Steel Mill.
- [14] Hernas A.: *Creep-resistance of steels and alloys*, Silesian University of Technology Publishing House, Gliwice, 2000.

Zagadnienia zmian struktur i twardości połączeń spawanych stali Hardox i HTK

W artykule przedstawiono budowę strukturalną i zmiany twardości połączeń spawanych stali Hardox 400 i Hardox 500. Wykazano, że w wyniku spawania tych materiałów w stanie dostarczenia (o strukturze martenzytu odpuszczonego) w strefach wpływu ciepła powstają struktury obniżające odporność na zużywanie ścierne. Mają one szerokość do 90 mm, co w przewidywanych zastosowaniach powoduje ich nierównomierne i szybkie zużywanie. Na podstawie badań mikroskopowych i pomiarów twardości, zaproponowano obróbkę cieplną połączeń polegającą na hartowaniu i niskim odpuszczaniu (samoodpuszczaniu) stref wpływu ciepła. Prowadzi to do odtworzenia struktur tego obszaru zbliżonych do struktury materiału rodzimego. Różniąc się od zazwyczaj stosowanych (wyżarzanie odprężające lub normalizujące) obróbka cieplna nie wywołała w warunkach laboratoryjnych powstawania w połączeniach niezgodności spawalniczych (pęknięć).



Thermo-mechanical processing of high-manganese austenitic TWIP-type steels

A. GRAJCAR, W. BOREK

Silesian University of Technology, Konarskiego 18a, 44-100 Gliwice, Poland

The high-manganese austenitic steels are an answer for new demands of automotive industry concerning the safety of passengers by the use of materials absorbing high values of energy during collisions. The chemical compositions of two high-manganese austenitic steels containing various Al and Si concentrations were developed. Additionally, the steels were microalloyed by Nb and Ti in order to control the grain growth under hot-working conditions. The influence of hot-working conditions on recrystallization behaviour was investigated. On the basis of initial investigations realized by hot upsetting the thermo-mechanical conditions resulting in a fine-grained structure were designed. The σ - ε curves and identification of thermally activated processes controlling work-hardening by the use of the Gleeble simulator were determined. It was found that the thermo-mechanical treatment conditions influence a phase composition of the investigated steels after solution heat treatment.

Keywords: *hot-working, thermo-mechanical processing, TWIP steel, dynamic recrystallization, ε martensite*

1. Introduction

Higher and higher demands of automotive industry referring to fuel consumption and emission of harmful exhaust gas limiting and especially improvement of car users' safety can be met by steels with austenitic microstructure. In the last few years an increased interest in high-manganese austenitic steels has been observed. High-manganese austenitic steels consist of 15 to 30% of manganese, from 0.02 to 0.1% of carbon and around 3% of aluminium and 3% of silicon. These steels achieve profitable group of mechanical properties, i.e. UTS = 600–900 MPa, $YS_{0.2}$ = 250–450 MPa, UEI = 35–80% which strongly depends on chemical composition, especially concentration of Mn [1–3].

Within a framework of numerous works the behaviour of high-manganese steels in cold plastic deformation conditions is investigated [2–4]. It was found that processes forming structure and mechanical properties of high-manganese steels depend on the stacking fault energy of austenite, depended on a chemical composition of the alloy and deformation temperature [1, 5]. Therefore, plastic deformation is realized in a wide range of temperature from -200 °C to 400 °C [3–6]. According to many works it was found that mechanical twinning is deciding mechanism about final properties of alloys with $SFE > 60$ mJm⁻². Decreasing the SFE from 60 to 20 mJm⁻² has prevalent significance on the course of mechanical twinning connected with TWIP effect (Twinning Induced Plasticity). With further decreasing the SFE below about 20 mJm⁻² essential meaning for improving the ductility of the steel has TRIP effect (Transformation Induced Plasticity).

Developing the technology of production of high-manganese austenitic steels requires knowledge about their behaviour during hot-working. There is a shortage of sufficient information in science publications. In the work [7], the influence of initial grain size and deformation parameters on plasticity characteristics obtained in hot torsion tests for 18Cr-8Ni and 18Cr-17Mn-0.5C steels was investigated. It was found that Cr-Mn steel characterizes with much higher intensity of strain hardening than Cr-Ni steel, which makes more difficulties during plastic deformation. Higher intensity of strengthening of the steel with addition of manganese causes occurrence of maximal flow stress for smaller ε_{\max} value. It gives opportunity for the refinement of structure by dynamic recrystallization. This phenomenon was investigated by Hamada et. al. [4] in 25Mn and 25Mn3Al steels in a temperature range from 900 to 1100 °C. It was found that maximal flow stress at a temperature of 1100 °C for 25Mn steel occurs for $\varepsilon_{\max} = 0.17$.

Application of thermo-mechanical treatment consisting in immediate cooling of products from a finishing temperature of hot-working in controlled conditions should increase mechanical properties [8]. Thermo-mechanical treatment of Hadfield's steel was investigated by Król [9] where was found that dynamic recrystallization can occur after deformation with 30% reduction at a temperature of 800 °C. Introduction of Nb and Ti microadditions to steels could be the reason for additional strain hardening of high-manganese steels and allows forming a fine-grained microstructure in successive hot-working stages. This problem is a main subject of the work.

2. Experimental procedure

Investigations were carried out on two high-manganese austenitic Mn-Si-Al steels containing Nb and Ti microadditions (Table 1). Melts were realized in the Balzers VSG-50 inductive vacuum furnace. Ingots with a mass of 25 kg were submitted open die forging on flats with a width of 220 mm and a thickness of 20 mm. Then, cylindrical samples $\varnothing 10 \times 12$ mm were made. Preliminary tests consisted in hot upsetting in a temperature of 900 and 1000 °C with 20, 40 and 60% reduction. Upsetting was carried out using the PMS 50 eccentric press with a strain rate of about 30 s^{-1} .

Table 1. Chemical composition of the investigated steels, mass fraction

Designation	C	Mn	Si	Al	P	S	Nb	Ti	N
27Mn-4Si-2Al-Nb-Ti	0.040	27.5	4.18	1.96	0.002	0.017	0.033	0.009	0.0028
26Mn-3Si-3Al-Nb-Ti	0.065	26.0	3.08	2.87	0.004	0.013	0.034	0.009	0.0028

On the basis of preliminary tests worked out the time-temperature conditions of hot-working which should cause a formation of fine-grained recrystallized austenite before cooling of samples from a temperature of final deformation. A selected sequence of deformations and time between particular deformations correspond to designed hot-rolling of steel (Table 2). Thermo-mechanical treatment was realized using the Gleeble 3800 thermo-mechanical simulator.

Metallographic examinations of samples were carried out using the LEICA MEF4A light microscope. In order to reveal austenite grain boundaries, the samples etched in a mixture of nitrous and hydrochloric acid in various proportions. Identification of the phase composition of steels in the initial state and after thermo-mechanical treatment achieved using the X'Pert PRO diffractometer with X'Celerator detector. The lamp with Co anode was applied.

Table 2. Parameters of the thermo-mechanical treatment realized in the Gleeble simulator

No	T_A , °C	Deformation I			Cooling I - II		Deformation II			Cooling II - III		Deformation III			Cooling III - IV		Deformation IV			t_{isother} at 850°C, s	Final cooling
		T_1 °C	φ_1	$\dot{\varphi}_1$ s ⁻¹	V_1 °C/s	t_1 s	T_2 °C	φ_2	$\dot{\varphi}_2$ s ⁻¹	V_2 °C/s	t_2 s	T_3 °C	φ_3	$\dot{\varphi}_3$ s ⁻¹	V_3 °C/s	t_3 s	T_4 °C	φ_4	$\dot{\varphi}_4$ s ⁻¹		
1-5	1100	1100	0.29	7	4	12.5	1050	0.29	8	8	12.5	950	0.29	9	10	10	850	0.29	10	0-64	Water
6	1100	1100	0.29	7	4	12.5	1050	0.29	8	8	12.5	950	0.29	9	10	10	-	-	-	-	

T_A – austenitizing temperature, T_1 – T_4 – deformation temperatures, φ_1 – φ_4 – true strains, V_1 – V_4 – cooling rates between deformations, t_1 – t_3 – times between deformations, t_{isother} – time of the isothermal holding of specimens at a temperature of 850°C

3. Results

Melted steels possess diversified initial structures presented in Figures 1 and 2. The 27Mn-4Si-2Al-Nb-Ti steel is characterized with the austenitic structure with a content of about 12% of ϵ martensite, whereas 26Mn-3Si-3Al-Nb-Ti steel possesses a pure austenitic structure. Both steels have comparable grain size in a range from 100 to 150 μm . Numerous annealing twins and non-metallic inclusions can be observed.

Application of plastic strain at a temperature of 1000 °C allowed identifying a mechanism controlling the work-hardening of steel. The structures of the 27Mn-4Si-2Al-Nb-Ti steel solution heat-treated from a temperature of 900 °C after deformation with 20, 40 and 60% reduction are shown in Figures 3–5. Effect of the dynamic recrystallization is visible by refinement of structures after applying 40 and 60% reduction. Deformation of the steel at 1000 °C with a reduction of 20% does not lead to initiate dynamic recrystallization. Whereas, applying deformation with a reduction of 40%, causes dynamic recrystallization (Figure 6).

Work-hardening curves of steels are presented in Figure 7. It can be useful to estimate force-energetic parameters of hot rolling. It was established that finish rolling will be realized in four passes at a temperature range from 1100 to 850 °C. It is apparent from Figure 7, that for applied parameters of plastic deformation, dynamic recrystallization is a process controlling work-hardening in a whole temperature range of hot-working. The steel containing 3% Si and 3% Al possesses a little higher value of flow stress. Strain value ϵ_{max} corresponding to maximum flow stress for particular stages amounts from 0.19 to 0.27. Additionally, maximum stress moves towards higher stress value for the 26Mn-3Si-3Al steel.

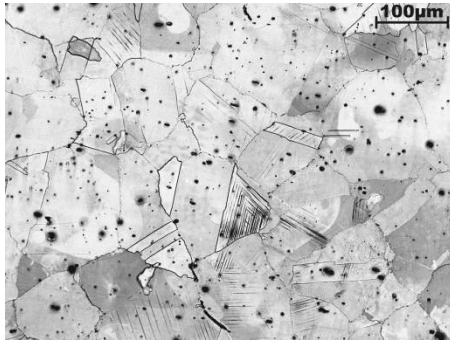


Fig. 1. Initial structure of 27Mn-4Si-2Al steel containing ϵ martensite in austenitic matrix

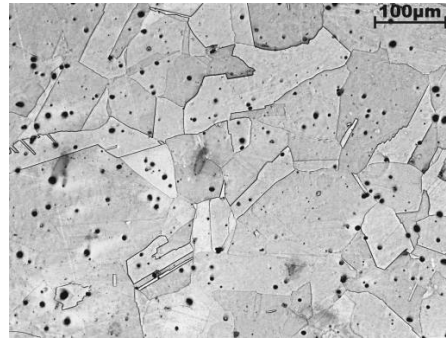


Fig. 2. Initial structure of austenitic 26Mn-3Si-3Al steel



Fig. 3. Structure of 27Mn-4Si-2Al steel solution heat-treated from a temperature of 900 °C after deformation with reduction 20%



Fig. 4. Refined structure of 27Mn-4Si-2Al steel solution heat-treated from a temperature of 900 °C after deformation with reduction 40%

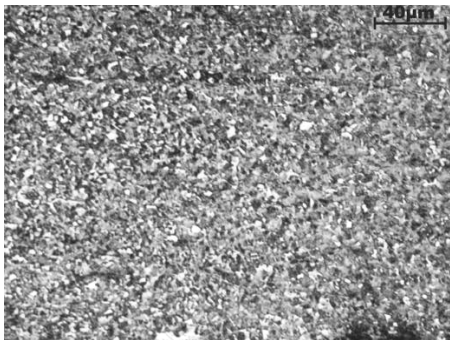


Fig. 5. Refined structure of 27Mn-4Si-2Al steel solution heat-treated from a temperature of 900 °C after deformation with reduction 60%



Fig. 6. Refined structure of 27Mn-4Si-2Al steel solution heat-treated from a temperature of 1000 °C after deformation with reduction 40%

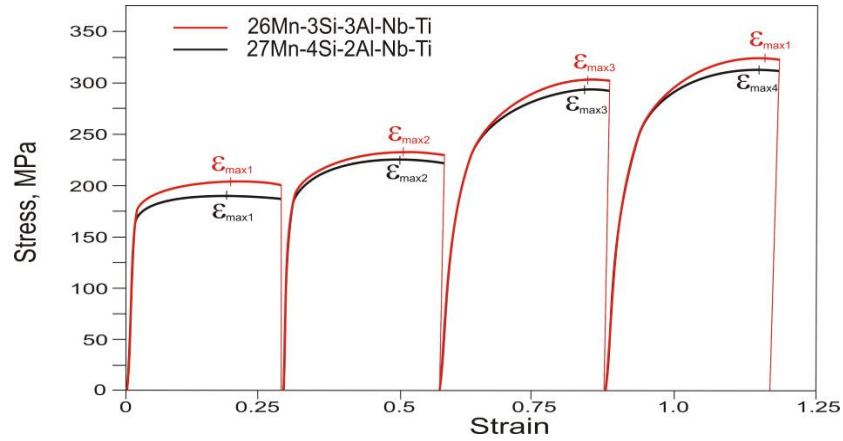


Fig. 7. Changes of flow stress as a function of strain in successive deformation stages

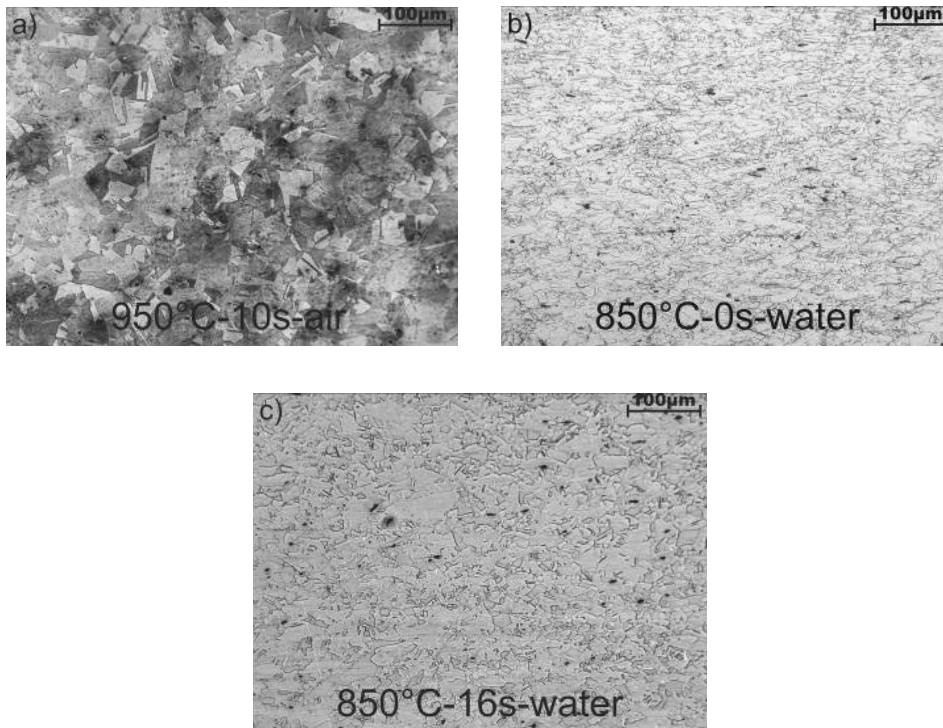


Fig. 8. Structure development of 27Mn-4Si-2Al-Nb-Ti steel in successive stages of the plastic deformation; a) solution heat treatment from a temperature of 850 °C before final deformation, b) solution heat treatment directly after final deformation, c) solution heat treatment after isothermal holding steel for 16s at a temperature of 850 °C

Development of the structure for the 27Mn-4Si-2Al-Nb-Ti steel after thermo-mechanical treatment is presented in Figure 8a–c. Before the final deformation simulated input into a last roll pass, the steel is characterized by the uniform structure of metadynamic recrystallized grains with a size of 10 to 20 μm (Figure 8a). Solution heat treatment of steel directly after the last deformation causes a significant refinement of structure due to dynamic recrystallization. The steel has austenitic structure with dynamic recovered grains with a size from 15 to 25 μm and fine dynamic recrystallized grains (Figure 8b). Application of isothermal holding for 16 s at 850 $^{\circ}\text{C}$ causes the further refinement of dynamic recovered grains, keeping dynamic recrystallized grains on a level up to about 7 μm (Figure 8c).

The structure of 26Mn-3Si-3Al-Nb-Ti steel is very comparable before a final deformation (Figure 9a), and also obtains the maximal refinement after isothermal holding for 16 s at 850 $^{\circ}\text{C}$ (Figure 9b). Further isothermal holding of steel up to 64 s causes a grain growth in a result of metadynamic and static recrystallization (Figure 9c).

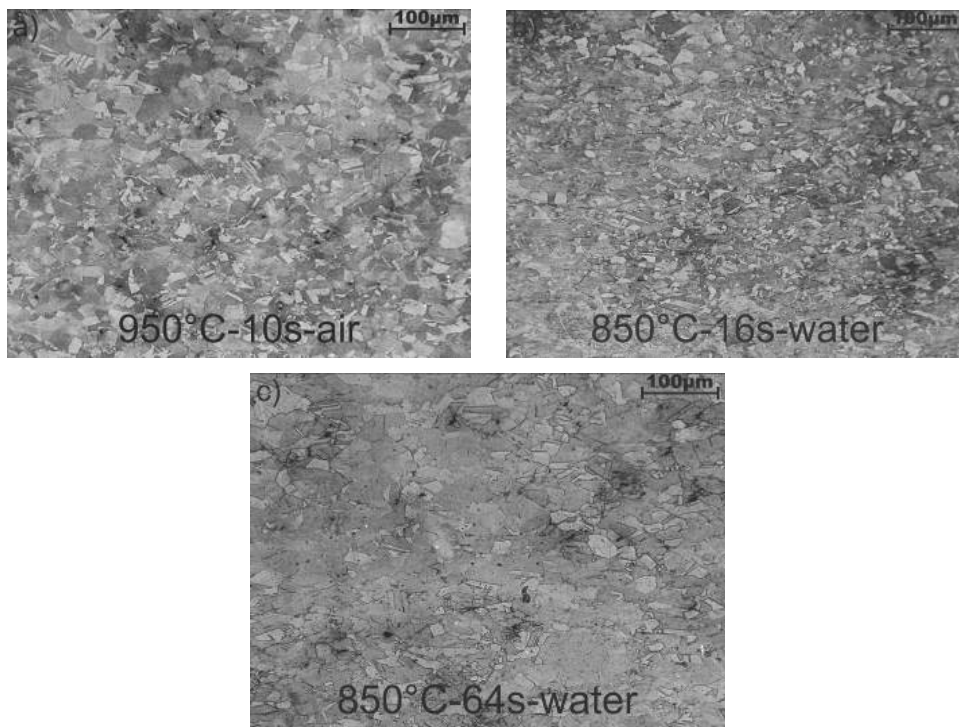


Fig. 9. Structure development of 26Mn-3Si-3Al-Nb-Ti steel in successive stages of the plastic deformation; a) solution heat treatment from a temperature of 850 $^{\circ}\text{C}$ before final deformation, b) solution heat treatment after isothermal holding steel for 16 s at a temperature of 850 $^{\circ}\text{C}$, c) solution heat treatment after isothermal holding steel for 64 s at a temperature of 850 $^{\circ}\text{C}$

It is important that in the steel with the $\gamma+\varepsilon$ initial structure any martensite was not observed. The confirmation of this fact is the X-ray diffraction pattern shown in Figure 10.

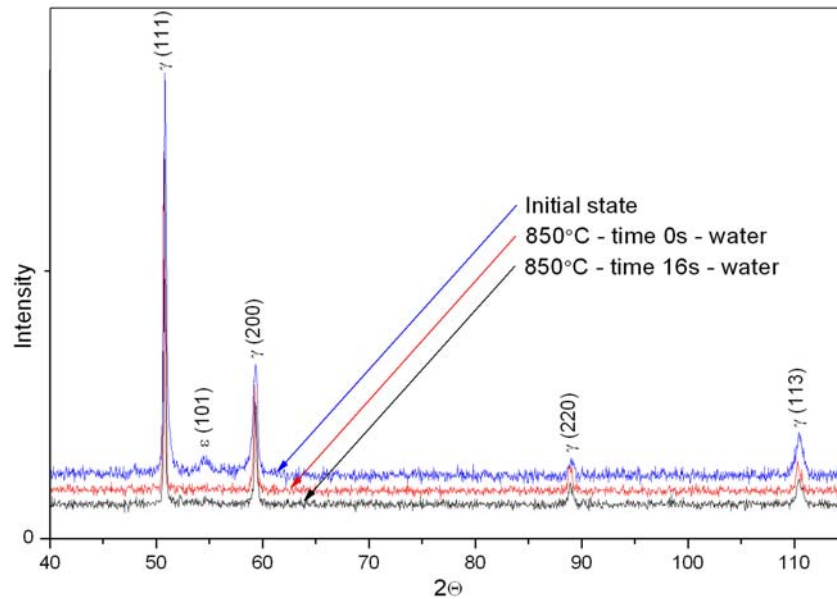


Fig. 10. X-ray diffraction patterns for 27Mn-4Si-2Al steel in the initial state and after thermo-mechanical treatment with isothermal holding of specimens for 0 and 16s at a temperature of 850 °C

4. Discussion

Investigated steels obtained diversified initial structures (Figures 1, 2). The presence of ε martensite in the structure of steel containing 4% Si is a result of the element influence on decreasing the stacking fault energy (SFE) of austenite [1–3]. Decreasing the contents of silicon up to 3% with simultaneous increasing concentration of aluminium from 2 to 3% caused increasing the SFE, what stabilized the austenite. Differences in chemical composition do not have the significant influence on the behaviour of steels in conditions of hot-working. Dynamic recovery is a process controlling strain hardening in both steels during plastic strain with a reduction of 20% at a temperature of 900 °C (Figure 3). Dynamic recrystallization is a main mechanism removing work-hardening of the steel after increasing reduction up to 40% (Figure 4). In reality, should be supposed that it will be initiated at a lower true strain in a range between 0.2–0.4. Further increasing of the reduction up to 60% caused obtaining a very refined and uniform austenitic structure (Figure 5). Increasing the plastic strain temperature up to 1000 °C does not change essentially deformation values initiating the

dynamic recrystallization (Figure 6). Refinement of the steel structure due to dynamic recrystallization with relatively low values of deformation, gives a reason to design a rolling process controlled by the dynamic recrystallization.

Multi-pass deformation tests allow to found out that investigated steels make difficulties during deformation. The flow stress values in the initial deformation stages are slightly higher than in the IF, DP and TRIP steels [8, 10], and also higher than austenitic Cr-Ni and Cr-Mn steels [7]. It is a result of hardening due to high concentration of Mn, Si, Al and Nb and Ti microadditions in steels. Applied deformation conditions cause that work-hardening in a whole range of deformation temperature is controlled by dynamic recrystallization (Figure 7), and softening of the structure during the time between passes proceeds by metadynamic recrystallization (Figures 8a, 9a). In result was achieved relatively not high increase of flow stress in the final stadium of deformation, even for the lowest temperature of plastic strain (850 °C). The data show that investigated steels in spite of higher initial deformation resistance could be produced using conventional technological lines.

The stress-strain curve (Figure 7) indicates, that applying a smaller reduction in a final pass than applied true strain 0.29, should probably cause also dynamic recrystallization and refining of the steel structure. Further hypothetical decreasing of true strain below about 0.25 and maintaining refinement of austenitic structure before solution heat treatment, will require application of isothermal holding at a temperature of 850 °C for time about 16s, which is needed to obtain some fraction of recrystallized austenite in a metadynamic process (Figures 8c, 9b). It is interested that applied thermo-mechanical treatment caused obtaining the austenitic structure for the steel with the initial two-phase structure $\gamma+\varepsilon$ (Figure 10). It is probably connected with a significant structure refinement in comparison with an initial state and with hampering influence of grain boundaries on a growth of ε martensite plates during cooling process of the steel. Similar effects were found in the work [11] for Fe-21Mn steel and in the work [4] for Fe-25Mn steel.

5. Conclusions

The carried out multi-stages compression tests allowed to determine the behaviour of developed high-manganese Mn-Si-Al steels with Nb and Ti microadditions during hot-working, simulating final passes in the thermo-mechanical rolling. Applied parameters of plastic deformation allow to found out, that the process controlling the work-hardening in a whole temperature range of hot-working is dynamic recrystallization. Metadynamic recrystallization is a process decreasing the work-hardening in the time between successive deformation stages. These processes allow to carry out the hot-working with flow stresses slightly higher comparing to DP and TRIP steels and lead to obtain the fine-grained steel structure with a grain size up to about 10 μm . The fine-grained structure has influence on a phase composition of steel and should increase mechanical properties during subsequent cold plastic deformations.

Acknowledgment

Scientific work financed from the science funds in a period of 2006-2008 in the framework of project No. 3 T08A 080 30.

References

- [1] Frommeyer G., Grässel O.: *High strength TRIP/TWIP and superplastic steels: development, properties, application*, La Revue de Metallurgie-CIT, No. 10, 1998, pp. 1299–1310.
- [2] Frommeyer G., Brück U., Neumann P.: *Supra-ductile and high-strength manganese-TRIP/TWIP steels for high energy absorption purposes*, ISIJ International, Vol. 43, No. 3, 2003, pp. 438–446.
- [3] Vercammen S., Blanpain B., De Cooman B.C., Wollants P.: *Mechanical behaviour of an austenitic Fe-30Mn-3Al-3Si and the importance of deformation twinning*, Acta Materialia, Vol. 52, 2004, pp. 2005–2012.
- [4] Hamada A.S., Karjalainen L.P., Somani M.C.: *The influence of aluminium on hot deformation behaviour and tensile properties of high-Mn TWIP steels*, Materials Science and Engineering A, Vol. 467, 2007, pp. 114–124.
- [5] Allain S., Chateau J.P., Bouaziz O., Migot S., Guelton N.: *Correlations between the calculated stacking fault energy and the plasticity mechanisms in Fe-Mn-C alloys*, Materials Science and Engineering A, Vol. 387–389, 2004, pp. 158–162.
- [6] Grässel O., Krüger L., Frommeyer G., Meyer L.W.: *High strength Fe-Mn-(Al, Si) TRIP/TWIP steels development – properties – application*, International Journal of Plasticity, Vol. 16, 2000, pp. 1391–1409.
- [7] Niewielski G., Hetmańczyk M., Kuc D.: *Wpływ struktury wyjściowej i warunków odkształcania na właściwości stali austenitycznych odkształczanych na gorąco*, Inżynieria Materiałowa, Vol. 24, No. 6, 2003, pp. 795–798.
- [8] Adamczyk J., Grajcar A.: *Obróbka cieplno – mechaniczna blach umacnianych przez efekt TRIP*, 12. Międzynarodni Vedecka Konferencje Forming'2005, Lednice, 2005, pp. 1–6.
- [9] Król S.: *Wpływ obróbki cieplno – mechanicznej i starzenia na strukturę i własności mechaniczne stali Hadfielda 11G12*, Praca doktorska, Politechnika Śląska, Wydział Mechaniczny Technologiczny, Gliwice, 1974.
- [10] Adamczyk M., Hadasik E., Niewielski G., Kuc D.: *Symulacja procesu walcowania na gorąco stali przeznaczonych na karoserie*, Inż. Materiałowa, Vol. 27, 2007, pp. 737–740.
- [11] Jee K.K., Han J.H., Jang W.Y.: *Measurement of volume fraction of ϵ martensite in Fe-Mn based alloys*, Materials Science and Engineering A, Vol. 378, 2004, pp. 319–322.

Obróbka cieplno – mechaniczna wysokomanganowych stali austenitycznych typu TWIP

Wysokomanganowe stale austenityczne stanowią odpowiedź dla nowych zadań przemysłu motoryzacyjnego dotyczących bezpieczeństwa pasażerów przez zastosowanie materiałów absorbujących dużą ilość energii w warunkach kolizji. Opracowano składy chemiczne dwóch wysokomanganowych stali austenitycznych zawierających różne stężenie Al i Si. Dodatkowo, w celu kontroli rozrostu ziaren w warunkach obróbki plastycznej na gorąco stale zawierają mikrododatki Nb i Ti. Zbadano wpływ warunków obróbki plastycznej na gorąco na przebieg re-

krystalizacji. Na podstawie badań wstępnych zrealizowanych przez spęczanie na gorąco zaprojektowano warunki obróbki cieplno – mechanicznej prowadzące do uzyskania drobnoziarnistej struktury. Przy zastosowaniu symulatora Gleeble wyznaczono krzywe σ – ε oraz aktywowane ciepłnie procesy kontrolujące umocnienie odkształceniowe. Stwierdzono, że warunki obróbki cieplno – mechanicznej mają wpływ na skład fazowy badanych stali po przesycaaniu.

Numerical modeling of flow through moving water-control gates by vortex method. Part II – calculation result

S. W. Kostecki^a

^aWrocław University of Technology, Wybrzeże Wyspiańskiego 25, 50-370 Wrocław

Numerical results are presented for uniform approach flow past emergency gate model, placed in a 2-D channel with free water surface, for two cases: (1) fixed gate and (2) gate moving perpendicular to the water flow. The calculations were made in the dimensionless system, for the assumed Reynolds number $Re=10^6$. The velocity field and vorticity field were determined by vortex method. On this basis the pressure distribution profile and hydrodynamic force were determined by means of boundary elements method. The vortex structures and the evolution of vortex shedding are illustrated by velocity field of vortex blobs for both cases– fixed and movable gate. We also presented the distribution of the pressure coefficient alongside the gate edge as well as the derivative lift and drag coefficients. The average force coefficients agree very well with the experimental values. The movement of downward of the gate substantially increases the calculated value of the lift coefficient.

Keywords: *hydraulic gates, turbulence flow, hydrodynamic force, vortex method, moving boundary*

1. Introduction

This paper presents the results of numerical modeling of the flow around a hydraulic gate. This problem is of practical significance when determining the hydrodynamic force acting on an emergency gate immersed in a stream of fast-flowing water. The movement of lowering the gate in a stream of fast-flowing water makes the distribution of velocity vectors under and behind the gate affects the pressure of the gate surface. In result, the hydrodynamic force is changed and also some instability of the flow might appear. The in stability might, subsequently, cause gate vibrations. This phenomenon was investigated into and described by Naudascher [8], Thang [11] and Billeter [2,3], focusing more on the gate vibrations. Aydin [1] researched experimentally the time-averaged pressure on the surface of a flat lift gate in conduit in which the space was submerged and pressurized when opening and closing it.

As mentioned before, the emergency gate used on dam spillways and weirs has been used as the calculation example. This gate works occasionally, taking over the role of the main gate in an emergency. Unlike a repair gate, an emergency gate is installed in flowing water, which causes a change of the load system. This needs to be taken into account when dimensioning. For spillways, an emergency gate is composed

of a few elements shaped like a flat gate or beam, in outlet conduit, an emergency gate is usually the same as the regulating one (Fig. 1). An emergency gate is placed upstream it moves on wheel in pile slots.

Numerical modeling of the flow velocity and pressure distribution on movable hydraulic gates is very complex, which stems from a strong flow turbulence and a complicated procedure of taking into account the boundary conditions. In moving boundary the condition of concordance of edge and adjacent fluid velocity must be fulfilled. Moreover, if gate movement or a big amplitude vibration is to take place, the conservation of mass must be met in the circumstances of change of the calculation area topology.

In order to solve this problem for a flat flow, the author applied the discrete vortex method, which describes the convective and diffusive transport of vorticity and corresponds to solution of viscous liquid flow described by Navier-Stokes equations. The solution with this method consists of describing the movement of the particles transporting vorticity, the so-called vortex blobs in the Lagrange system. The time is discretized using a finite difference procedure. The vortex method description, special emphasis laid on a moving edge problem, was presented by the author, in his paper [7] which constitutes the first part hereof.

The present paper is aimed at numerical modeling of the distribution of velocity, vorticity, the stream function and hydrodynamic force for a moving (lowered) emergency beam-shaped gate and a comparison of the results with those for a fixed gate. The diagram of the free water surface gate under consideration and the coordinate system has been presented in Figure 2.

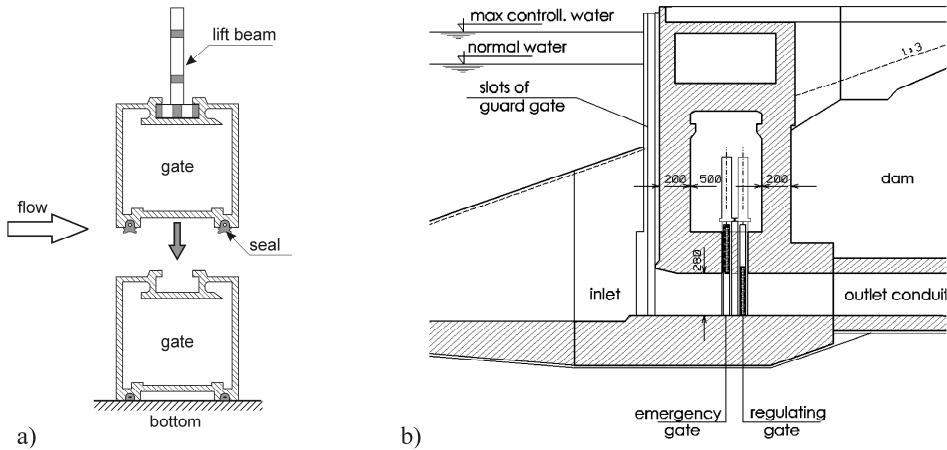


Figure 1. Examples of emergency gates: a) free surface –beam, b) high head – vertical lift

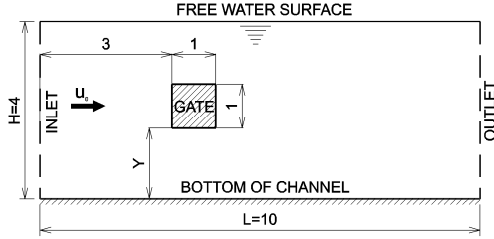


Figure 2. Model of a channel with a gate

2. Pressure and hydrodynamic forces determination

The problem of pressure in a viscous liquid flow in area D , limited with edge S , should be determined from the Navier-Stokes equation [7]. The effective way of solving this problem is applying the divergence operation to the Navier-Stokes equation, which transforms it into the Poisson equation for pressure [5], [10]:

$$\nabla^2 P = -\nabla \cdot \left(\frac{\partial \mathbf{u}}{\partial t} + \mathbf{u} \cdot \nabla \mathbf{u} - \nu \nabla^2 \mathbf{u} \right) = -\nabla \cdot \mathbf{B} \quad \text{in } D \quad (1)$$

where $\mathbf{u} = [u_1, u_2]$ velocity vector, $P = p/\rho$ – kinematic pressure, ρ – liquid density, ν – kinematic viscosity coefficient.

To solve this equation, it is necessary to know vector \mathbf{B} , which depends on the velocity field, and a boundary condition. By defining the Neumann-type condition

$$\frac{\partial P}{\partial n} = -\mathbf{B} \cdot \mathbf{n} \quad \text{on } S \quad (2)$$

we can solve expression (1)–(2) by the boundary elements method, using the following relation, derived in paper [6]:

$$c(\xi)P(\xi) + \int_S P \frac{\partial P^*(\mathbf{x}, \xi)}{\partial \mathbf{n}} dS(\mathbf{x}) + \int_S P^*(\mathbf{x}, \xi) \frac{\partial \mathbf{u}}{\partial t} \cdot \mathbf{n} dS(\mathbf{x}) = -\sum_{j=1}^M \left\{ \sum_{k=1}^{N_g} [\mathbf{r}_k w_k] A_j \right\},$$

$$\mathbf{r}_k = \left(\nabla \left(\frac{\mathbf{u}^2}{2} \right) \cdot \nabla_x P^*(\mathbf{x}, \xi) + \boldsymbol{\omega} (\mathbf{u} \times \nabla_x P^*(\mathbf{x}, \xi)) - \nu (\nabla \times \boldsymbol{\omega}) \cdot \nabla_x P^*(\mathbf{x}, \xi) \right)_k, \quad (3)$$

$$P^*(\mathbf{x}, \xi) = -\frac{1}{2\pi} \ln |\mathbf{x} - \xi|, \quad \xi, \mathbf{x} \in \mathbb{R}^2$$

where: ξ – source point, M – number of finite elements of area A_j which domain D was divided into, N_g – number of points (nodes) of numerical integration for each element, w_k – weights of numerical quadrature, $c(\xi)$ – coefficient depends on smoothness of the boundary, for regular boundary $c(\xi) = 1/2$. Vorticity field ω and velocity \mathbf{u} were determined by vortex method, according to the methodology specified in the first part of the paper [7].

The hydrodynamic force can be defined in the form of the sum of the normal and tangent components:

$$\mathbf{F} = \mathbf{F}_n + \mathbf{F}_t \quad (4)$$

The first component depends on pressure, the second on viscous friction on the surface flow around:

$$\mathbf{F}_n = \int_{S(t)} p \mathbf{n} dS, \quad \mathbf{F}_t = - \int_S \mu \mathbf{\Pi} \cdot \mathbf{n} dS \quad (5)$$

where: $\mathbf{n} = [n_1, n_2]$ – unit external vector, normal to the edge flow around, μ – dynamic viscosity coefficient, $\mathbf{\Pi}$ – rate of deformation tensor. In flows that show a big Reynolds number, the force evoked by viscous friction is small compared to the force that results from pressure and it is neglected herein.

The components of the hydrodynamic force:

$$F_i = - \int_S p n_i dS \quad (6)$$

in aerodynamics they are called vertical lift and horizontal drag forces.

3. Physical state and calculation parameters

For calculations we assumed a flat steady flow with a free horizontal surface. In the stream there is an emergency gate, which can move with a fixed speed towards the bottom of the channel.

The calculations were performed in a dimensionless system, assuming all distances to be normalized along the gate side of a square cross-section $d = 1$. The unit velocity at the inlet is assumed $\mathbf{u}_0 = [1, 0]$. Time is also normalized with d / u_0 . The sizes of the channel are as follows: length 10, depth 4, the gate is placed 3 from the inlet. Two cases are considered:

Case (1) – fixed gate, placed subsequently $Y=2.6, 1.6, 0.6, 0$ over the channel bottom. The calculations consisted on positioning the vortices, determining fields of vorticity, velocity and pressure.

Case (2) – gate fixed in the upper position $Y=2.8$ by time $t=23$ (time step $kt=460$), and then the gate closing movement begins, with velocity $\mathbf{v} = [v_1, v_2] = [0, 0.1]$. In each calculation step, in the algorithm the change of the gate position and the occurrence of velocity component v_2 on its edge was taken into account, according to the description of the moving boundary condition contained in [7]. The calculation method described takes into account the separation of the flow under and over the gate as well as the effect of velocity v_2 on the shape of vortex trajectories and vortex generation. The calculation schema for the two cases is presented in Figure 3.

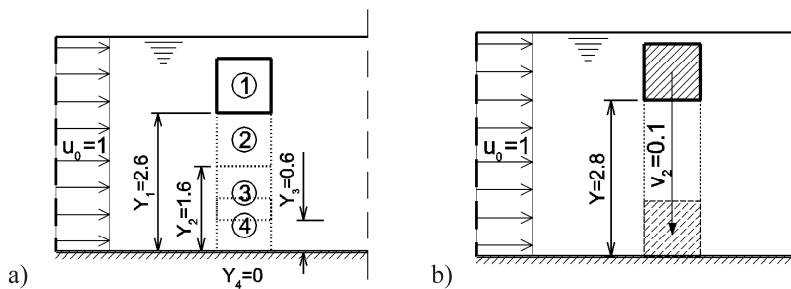


Figure 3. Calculation schema for gates: a) fixed, b) movable

The vortex-method calculations were made for the following calculation parameters:

- Division of the edge into sections to determine the intensity of the vorticity layer: $h=0.05$;
- cut radius $\varepsilon = h^{0.95} = 0.058$;
- time step $dt=0.05$; such an assumption makes sure that the displacement of a vortex drop in a single time step is comparable to h -value;
- number of time steps for each simulation $kt=1000$.

3. Numerical result

The numerical analysis of the flow was performed for a fixed gate in three positions $Y=2.6, 1.6, 0.6$ and a gate moving downwards. The calculation parameters have been chosen in such a way that in that same time moment both gates are in the same positions, which allows for result comparison.

Modeling results of vorticity field evolution by vortex method are presented in Figure 4 in the form of vortex blobs – vorticity carriers.

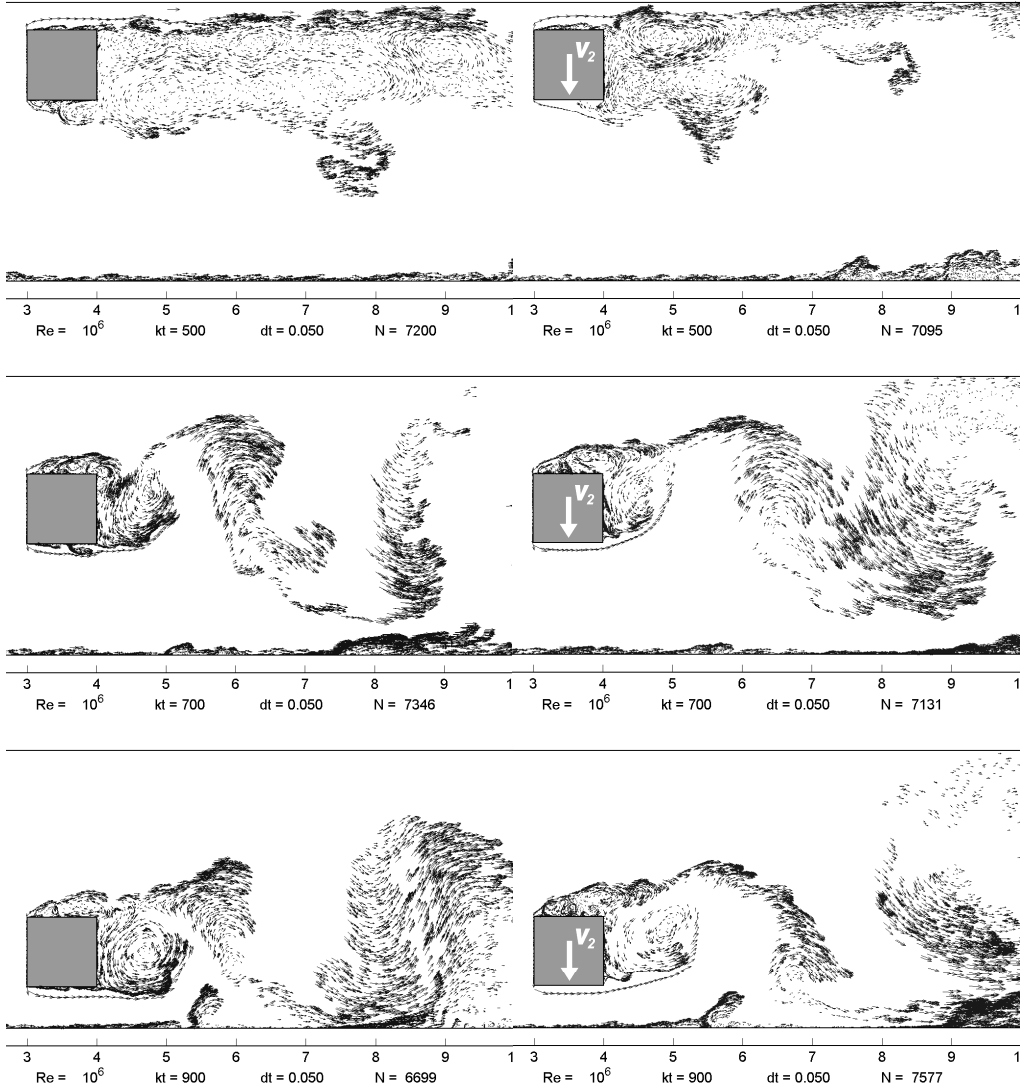


Figure 4. Comparison of vortex blobs dynamics for a fixed and movable gate, for the same positions and time instants $Y=2.1, t=25$; $Y=1.1, t=35$; $Y=0.5, t=45$; $Y=0, t=50$. Movable gate on the right.

Behind the fixed gate there emerges a regular Kármán vortex path, forming out of big coherent vortex structures, detaching alternately from the upper and from the lower edges of the gate. The downward closing movement makes the vortex blob velocity vectors deflect upwards. Then the vortices do not separate from the lower edge of the gate, but tend to be eliminated since their trajectories cross with the moving edge, which is observable in Figure 4.

Differences in vortex blob trajectories cause differences in the flow velocity vectors. In Figure 5, a comparison of the calculated velocity field around fixed and movable gates is presented for position $Y=1.6$.

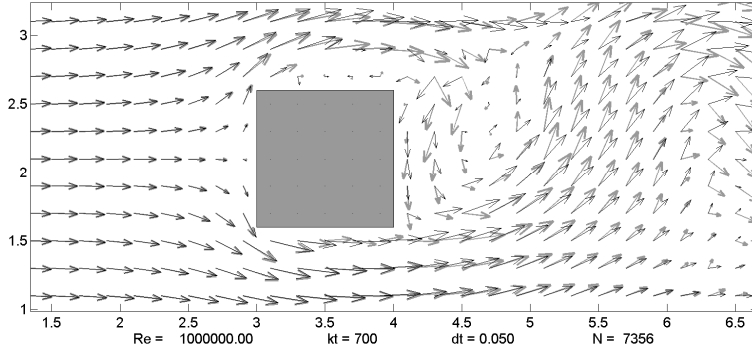


Figure 5. A comparison of velocity field around fixed and movable gates for $kt=700$, the grey arrows denote a fixed gate, black arrows show the moving one

Figure 6 shows a comparison of distribution of the pressure coefficient, C_p , on the gate model flown around, for fixed and movable gates. The pressure coefficient results from the dimensionless variable assumed in the calculations and is expressed by the formula:

$$C_p = \frac{2p}{\rho |\mathbf{u}_0|^2} \quad (7)$$

The essential difference can be observed on the lower edge flown around. In the fixed gate, strong negative values of C_p occur, which stems from the separation of the boundary layer from this edge and generating of vortex structures. When the gate is moving downwards, the phenomenon of vortex and recirculation zone formation fails to occur, what affects a bigger value of this coefficient.

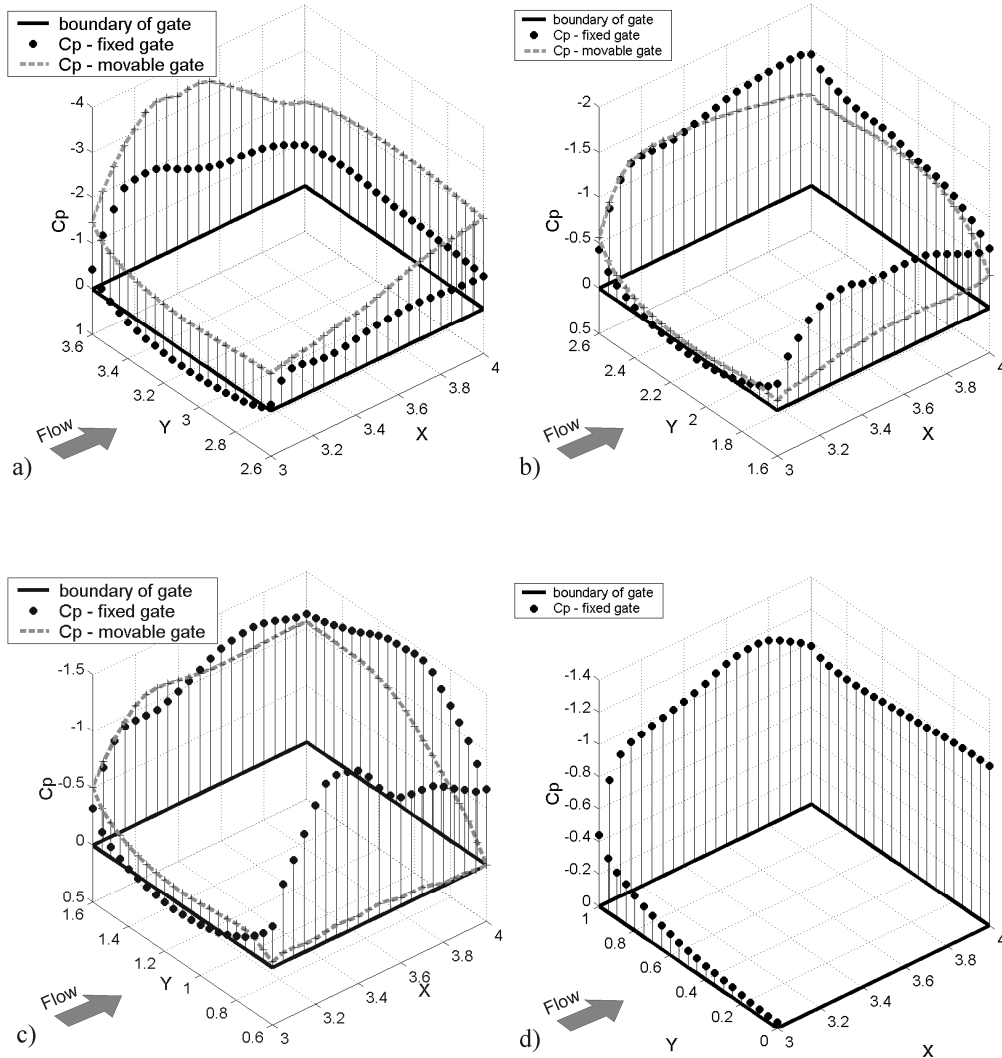


Figure 6. Distribution of the pressure coefficient, C_p , for fixed and movable gates for the same simulation times and gate positions: a) $Y=2.1, t=25$; b) $Y=1.1, t=35$; c) $Y=0.5, t=45$; d) $Y=0, t=50$

On the basis of relations (6) and (7) the lift force C_L and drag C_D coefficients were determined, which makes normalized values of hydrodynamic force components. For a fixed gate, the lift force is periodically variable and shows a steady amplitude, which is observable in Figure 7. This results from the regular detachments of the Kármán vortices intermittently from the upper and lower edges. The average value of this force coefficient $C_L=0.25$. It is different from zero as the boundary conditions for the flow are different. On the upper surface the vortex-generating phenomenon does not occur whereas along the canal bottom the vortices are generated, which is the cause of the

differences of vorticity and velocity distribution along the lower and upper edges of the gate. The drag coefficient's value is positive and stems from a low over-pressure on the front edge of the gate flown around and a considerable under-pressure on the rear edge, which is evoked by the vortex structures carried by the flow. The averaged value of the drag force coefficient $C_D=2.18$ scarcely differs from the experimental studies by Delaney and Sorenson [], who – for $Re=10^6$ – obtained the value $C_D=2.0$ and the studies by Obasaju, who obtained the C_D – value of 2.17.

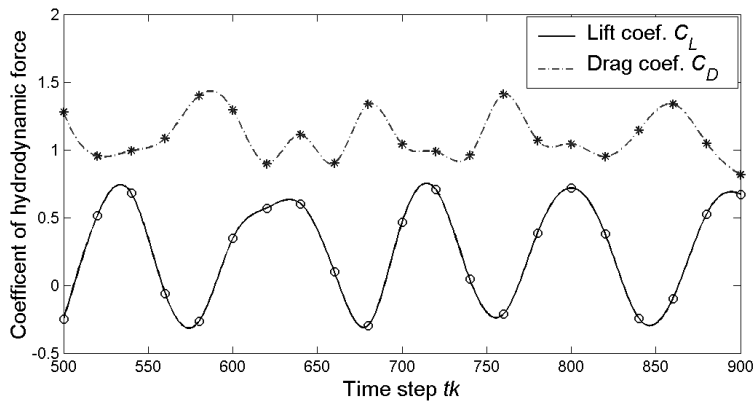


Figure 7. Lift and drag coefficient for a fixed gate

During the analysis of the time distribution of the hydrodynamic force for a movable gate it was observed that the downward movement of gate is the cause of a lower value of the averaged C_L and C_D as the gate is lowering. This proves an increasing effect of vorticity generated along the lower edge of the canal. Because the pressure from the top is much lower than that from the bottom of the gate, the resultant normalized hydrodynamic force is directed upwards. It is periodical and shows a high variability of the amplitude, which can be observed in Figure 8.

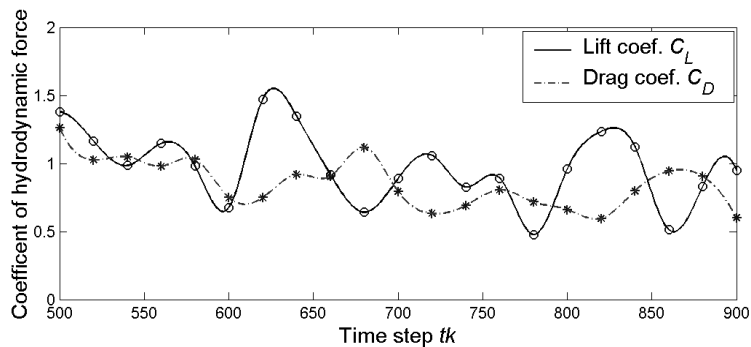


Figure 8. Lift and drag coefficient for a movable gate

5. Conclusions

Emergency gates are installed in flowing water and, for this reason, they are subject to different hydrodynamic loads. In order to analyze them, a method was worked out consisting of determining vorticity and velocity distribution in a flow area and, in this basis, determining the pressure distribution on the gate edges. The results of the calculations of a square cross-section beam-shaped gate moving at a speed of 0.1 of the water flow velocity imply a significant growth of the average value of the lift force in comparison with a fixed gate. For a fixed gate, it was directed downwards and its average dimensionless value $\bar{C}_L = 0.25$. When the gate was being lowered, this force was directed upwards and its value dropped from 1.2 to 0.8. The drop of the lift force was due to the vorticity effect, the vortices being generated along the channel bottom. The maximum value of the lift coefficient $C_L = 0.9$ for a fixed gate and $C_L = 1.5$ for a gate being lowered, accordingly. These values are smaller from the coefficient recommended for designing, which is $C_L = 2$.

The conformity of the drag coefficient value $C_D=2.18$ obtained for a fixed gate with the results of experimental shows that the proposed method is a good representation of the changes of the vortex path and can be used in the simulation of separation–reattachment dominated flows past blunt bodies.

References

1.	AYDIN I., TELCI I., DUNDAR O., Prediction of downpull on closing high head gates, J. Hydraul. Res. IAHR, Vol. 44 (6) (2006) 822-831.
2.	BILLETER P. (2000), Flow-Inducted Multiple-Mode Vibrations of Gates with Submerged Discharge, Journal of Fluids and Structures, Vol. 14, pp. 323-338.
3.	BILLETER P., (2004), Properties of single shear layer instabilities and vortex-induced excitation mechanisms of thick plates, Journal of Fluids and Structures, Vol. 19, pp. 335-348.
4.	DELANEY N. K., SORENSON N. E., Low-speed drag of cylinders of various shapes. NACA Tech. Note 3038 (1953)
5.	GRESHO, Ph. M., SANI, R., On Pressure Boundary Conditions for The Incompressible Navier-Stokes Equations, Int. J. Num. Meth. Fluids, Vol. 7 (1987) 1111-1145.
6.	KOSTECKI S., Numerical Determination of the Hydrodynamic Pressure Acting on a Hydraulic Gate, Polish J. of Environ. Stud., Vol. 16 , No 6B (2007) 39-45.
7.	KOSTECKI S., Numerical modeling of flow through moving water-control gates by vortex method. Part I – theoretical approach, Archives of Civil and Mechanical Engineering, ...
8.	NAUDASCHER E., ROCKWELL, D., Flow – Induced Vibrations., An Engineering Guide, A.A.Balkema, 1994.

9.	OBASAJU E. D., On the effects of end plate on the mean forces on square sectioned cylinders. <i>Journal Industrial Aerodynamics</i> , Vol.5 (1979) 179.
10.	PETERSSON N.A., Stability of Pressure Boundary Conditions for Stokes and Navier-Stokes Equations, <i>J. Comput. Phys.</i> , Vol. 172 (2001) 40-70.
11.	THANG N.D., Gate Vibrations due to Unstable Flow Separation, <i>J. Hydr. Eng.</i> , Vol. 116, No. 3 (1984) 342-361.

Numeryczne modelowanie przepływu przez ruchome zamknięcia wodne metodą wirów. Część II – wyniki obliczeń numerycznych

Zaprezentowano wyniki obliczeń numerycznych przepływu równomiernego przez model zamknięcia awaryjnego, umieszczonego w 2-wymiarowym kanale ze swobodną powierzchnią wody, dla dwóch przypadków: (1) zamknięcia nieruchomego i (2) przemieszczającego się w kierunku prostopadłym do kierunku prędkości wody. Obliczenia wykonano w układzie bezwymiarowym dla przyjętej liczby Reynoldsa $Re=10^6$. Pole prędkości i wirowości określano przez rozwiązanie metody wirów, na ich podstawie wyznaczano rozkład ciśnienia i siłę hydrodynamiczną za pomocą metody elementów brzegowych. Struktury wirowe i ewolucja ścieżki wirowej zostały zilustrowane za pomocą pola prędkości kropel wirowych dla obydwu przypadków – nieruchomego i ruchomego zamknięcia. Przedstawiono również rozkład współczynnika ciśnienia wzdłuż krawędzi zamknięcia oraz wynikające z niego współczynniki siły unoszenia i oporu. Uśredniona wartość tych współczynników pozostaje w dużej zgodności z wynikami badań eksperymentalnych. Ruch zamknięcia ku dołowi istotnie zwiększa obliczoną wartość współczynnika siły unoszenia.



Overview on the state of development and the application potential of dieless mechanical joining processes

R. NEUGEBAUER, M. TODTERMUSCHKE, R. MAUERMANN, F. RIEDEL
Fraunhofer Institute for Machine Tools and Forming Technology (IWU), Reichenhainer Str. 88, 09126 Chemnitz, Germany

In the course of ongoing development of mechanical joining technologies, different technologies were developed in the last years, where often the necessary die as contrary die was substituted by a flat anvil. Using the example of dieless clinching, the full potential of such process alternatives is visible. If the tools, as the punch or the blank-holder are modified and the necessary die is substituted by a flat anvil, then several advantages for the process alternative – the dieless clinching – emerges. For example, it is possible to produce a one-sided flat connection, which is not producible with any other joining technology. Additionally it is possible to enlarge the application potential of mechanical joining technologies as for example semi-finished parts made of magnesium can be partially heated and directly joined without an increase in process time or a reduction in the process stability. The tool's costs, the necessary tolerances and the tool wear are significantly reduced. The publication includes an overview over the state of the development and the application potential with practical examples of different process alternatives.

Keywords: *mechanical joining, clinching, riveting, flat-clinch-connection, dieless-clinching, dieless-riveting, aluminium, multi-material-design, simulation*

1. Introduction

Modern joining by forming technologies such as riveting or clinching is used increasingly in sheet-metal-processing industries because of their many advantages. Moreover these technologies are often interesting joining alternatives of new developed products with multi-material design [1–3]. Their biggest advantages are:

- high economic viability,
- wide variety of materials which can be joined similar or dissimilar,
- the absence of temperature influences to the base material in comparison to mostly used thermal technologies such as welding or brazing.

A special benefit of clinch connections is the possibility of joining without ancillary joining elements, such as rivets.

The reasons for developing dieless mechanical joining processes were manifold. The major motives are:

1. Gain improvements in process technology
 - no need of coaxial alignment between punch and die,
 - possibility to directly heat up components fast and easy by pushing them against the pre-heated flat anvil, to join even brittle materials, such as magnesium,

- reduction of space requirements inside of structures to be joined (no axial movement of die is necessary to pull out the protrusion of the die),
 - reduction of tool and process costs
 - die shape (see Figure 1) is expensive to manufacture and has higher tool wear than flat anvils, because flat anvil can be as hard as possible, e.g. carbide materials,
 - no dependence between tool shape and joining task (material, thickness)
2. Optimization of connection properties:
- facilitated cleaning and painting of surfaces,
 - reducing efforts at preparation of component flanges e.g. for sealing strips or wetting,
 - especially for flat clinch connections (see Figure 2e): manufacturing of one-sided completely flat connections allows a use of connection in visible areas or for piling up identical parts.



Fig. 1. conventional dies for clinch process: a) solid die, b) die with moving blades versus c) flat anvil as counter tool

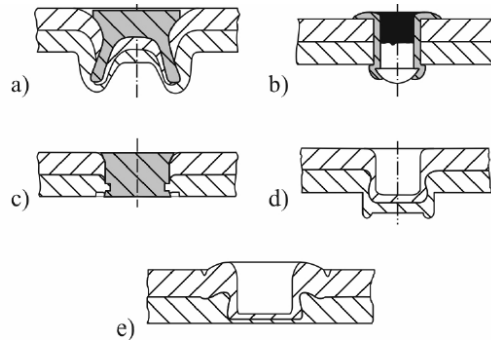


Fig. 2. Different kinds of mechanical joining Connections: a) hollow-self-pierce punch-rivet, b) blind-rivet, c) solid self-pierce punch-rivet, d) clinch, e) flat-clinch-connection

So far 4 different mechanical joining technologies have been developed and investigated, which use flat anvils as counter tool to create a form- and force-closed connection between two metal sheets. Figure 3 shows a classification of dieless joining technologies. They can be divided into processes with and without the need of ancillary parts, with or without material cutting inside of the connection and divided into connections with or without protrusions on anvil-sided component part.

The main objective was to realize a comparable technology with conventional processes with a die as counter tool, to keep the high economic efficiency and to be able to use similar joining machines. All shown technologies require an overlapping zone of the component parts for joining and at least three different tools which interact to create a mechanical joined connection. For dieless clinching [4–6], see Figure 4, in the beginning the component parts (1) and (2) are appropriate positioned between a punch (4), a blank-holder (5) and a flat counter tool – the anvil (3).

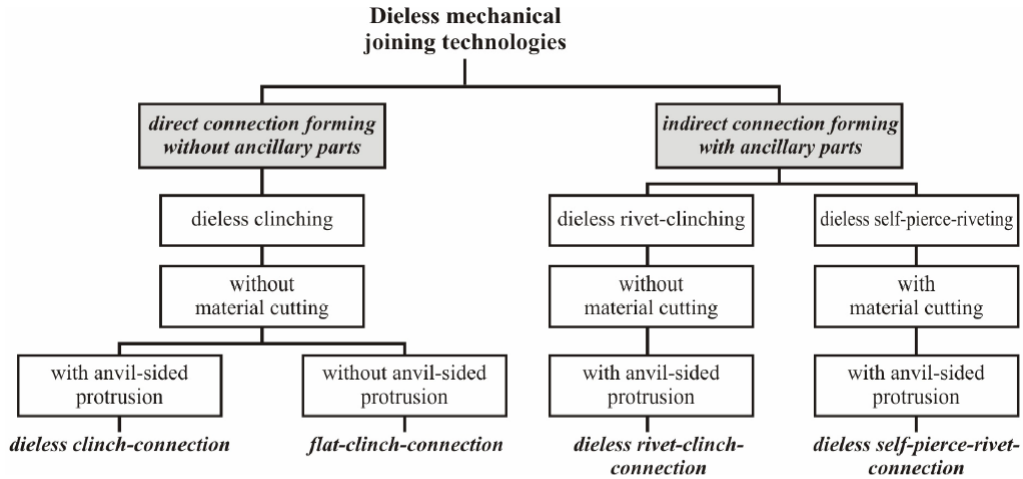


Fig. 3. Classification of dieless mechanical joining technologies

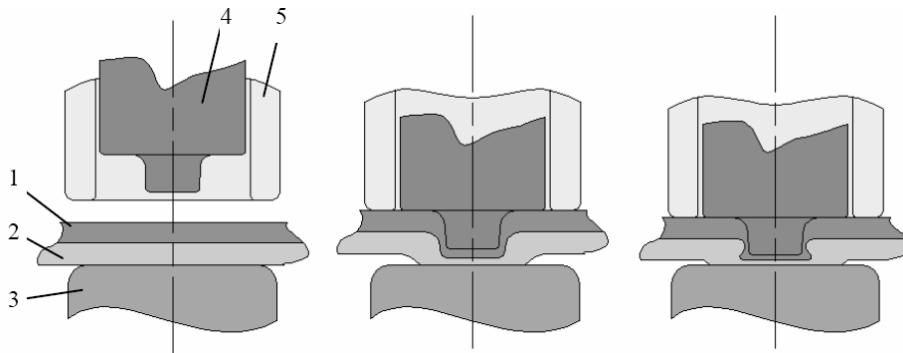


Fig. 4. Process principle of joining a dieless clinch-connection

To produce the connection, the punch and the blank-holder are then moved toward the components. With the blank-holder a defined retaining force is applied to the components. The punch is pressed with high force into the components. The material of the components in the joining area is displaced locally and moves first radially outwards and then, controlled by the blank-holder, upwards in opposite direction to the punch movement, similar to a can-reverse-extrusion-process. At this stage the material around the joining area will be lifted off from the anvil and creates a protrusion as conventional clinch connections have, see Figure 4-middle.

After contact of punch-sided material with the punch-shoulder further movement of the material in opposite punch-direction is obstructed. The formed protrusion will be reduced in its height with further feed of the punch and the material, which is still present under the shoulder of the punch, must flow radially outward. At this point a form closure – the interlocking f (see Figure 5) – inside the connection will be created, see

Figure 4-right. Depending on the material of the component parts, its combination and the length of the punch tap a bulging of the neck range inside the connection is possible, which leads to an slight increase in neck thickness t_n .

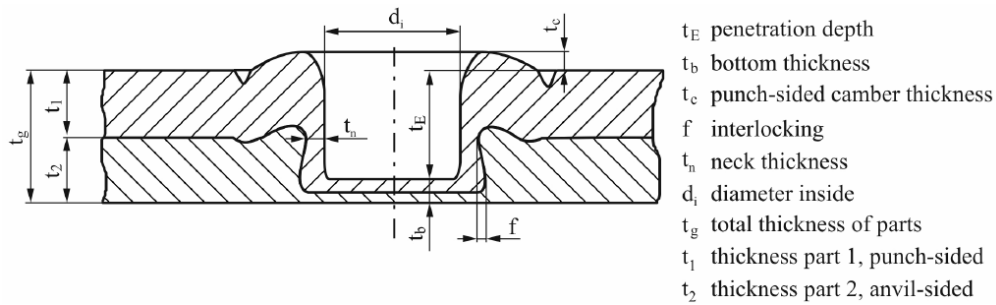


Fig. 5. Characteristic values of flat-clinch-connections

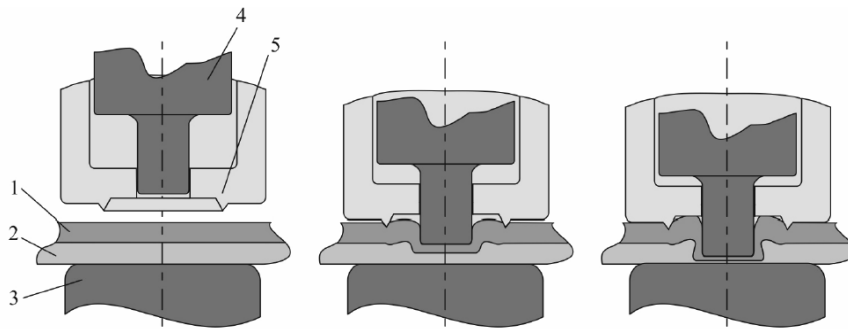


Fig. 6. Process principle of joining a flat-clinch-connection

The main difference between dieless and flat-clinch-connections is the complete avoidance of an anvil-sided protrusion [7–9]. This can be reached by increasing the blank-holder-force, which keeps the component parts flat on the anvil (3) during penetration of the punch, see Figure 6. Nevertheless to control the material flow including the creation of form-closed interlocking inside the connection the blank-holder (5) has a specific front face, which can be shaped with various elements. Suitable shapes are one or more circular rings with a triangular cross section or fillet radius at the inner diameter. As for dieless clinch connections the punch (4) penetrates the component parts and leads to a radial movement of material, especially in the anvil-sided part (2). Radial material distortion of punch-sided part (1) will be prevented by a circular profile. Instead of radial flow material can be transformed in opposite direction to punch feed into spaces of the blank-holder between the circular profiles and the punch. This material flow leads to a creation of interlocking, but without an anvil-sided protrusion. Nevertheless depending on material strength and combination a slight texture or groove at the anvil sided part can be found.

Dieless rivet-clinching (Figure 7) can be understood as a dieless clinching process with a “lost punch” [10, 11]. Instead of a clinch punch, the rivet (6) with a specific initial shape and material properties will be driven into the component parts (1) and (2) against the anvil (3) using a bigger rivet punch (4) and a blank holder (5). The rivet transforms the material but does not cut it at any stage and leads to a radial flow of it. As for dieless clinching an anvil-sided protrusion is created during the process, which will be reduced in height when the rivet punch pushes the material further after getting in contact with the punch-sided part. At this stage the interlocking will be created. Depending on material strength of rivet and component parts the rivet could be transformed as well.

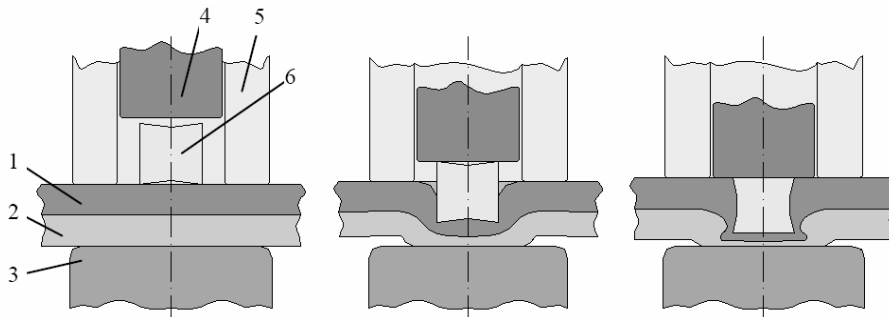


Fig. 7. Process principle of joining a dieless rivet-clinch-connection

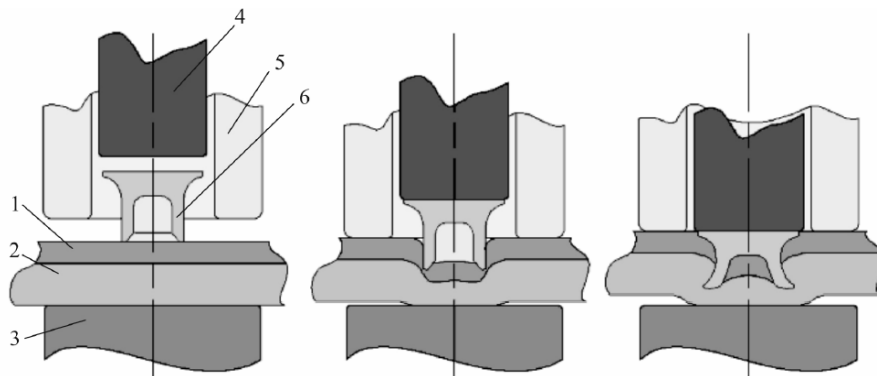


Fig. 8. Process principle of joining a self-pierce-rivet-connection

Another process, see Figure 8 which has a flat anvil (3) as counter tool but uses self-pierce rivets (6) is patented in [12]. In contrast to rivet-clinch-connections the punch sided material (1) will be cut during the process by the rivet but not the anvil-sided component (2). Conventional rivets as well as special geometries can be used. The whole joining process is very similar to dieless rivet-clinching.

2. Influencing parameters and characteristic values

To develop a new kind of connection its mechanical and geometrical properties must be considered. Geometrical shaping of the dieless clinch and rivet-clinch connections determines the mechanical and strength properties particularly. Considering practical investigations and complementary numerical simulations (see Figure 9) in-

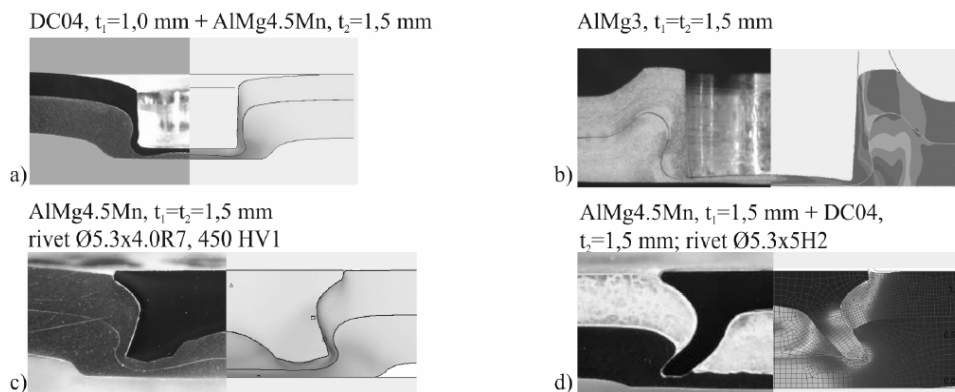


Fig. 9. Comparison of practical determined and numerical calculated cross sections of dieless mechanical connections; a) dieless clinch-connection, b) flat-clinch-connection, c) dieless rivet-clinch-connection, d) dieless self-pierce-rivet-connection

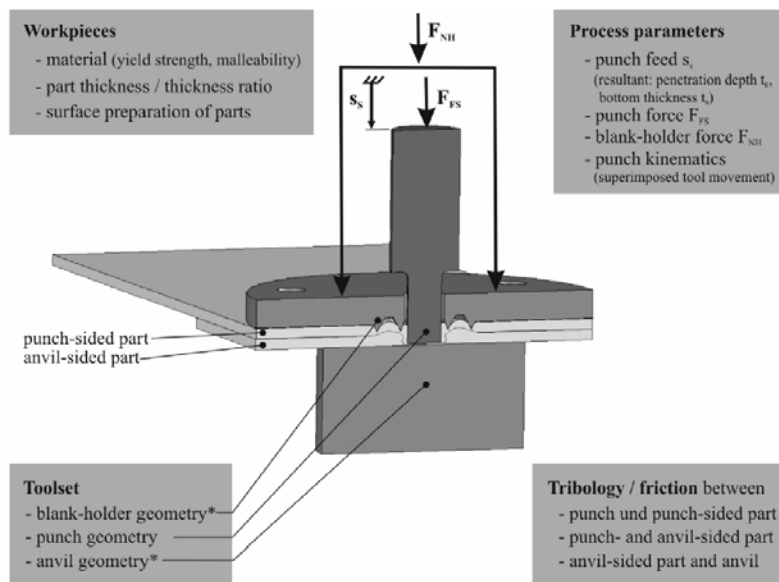


Fig. 10. Influencing variables to the manufacturing process of dieless and flat-clinch-connections
*flat-clinch connection only

terlocking and neck thickness are the most significant characteristic values. Essentially, characteristic values depending each other and are affected by the influencing parameters of the joining process. The most important influencing variables of manufacturing and mechanical properties of dieless and flat-clinch connections are shown in Figure 10.

In addition to these parameters for dieless rivet- and rivet-clinch-connections the following variables could be analyzed:

- material of rivet (yield strength, hardness, malleability),
- initial geometrical shape of rivet.

3. Experimental investigations and application examples

Extensive experimental investigations have been carried out for dieless clinch-, flat-clinch- and dieless rivet-clinch-technologies. Some of the results are shown next.

3.1. Dieless clinch-connections

One of the biggest advantages of dieless joining procedures is the much easier possibility to heat the component parts by thermal conduction compared to other mechanical joining technologies using a die as counter tool. By clamping parts shortly between blank-holder and flat anvil a fast and easy heating of whole joining area of the parts is possible, which results in a very short heating time. This procedure and the fact that inside of dieless clinch connections mainly compressive stress predominates enables this technology to join even brittle materials, such as magnesium. Figure 11 shows a cross-section and the anvil-sided view of a dieless clinch connection where the anvil-sided part is magnesium. Recognizable is a big interlocking without cracks inside the connection, what could not be reached without heating the magnesium.

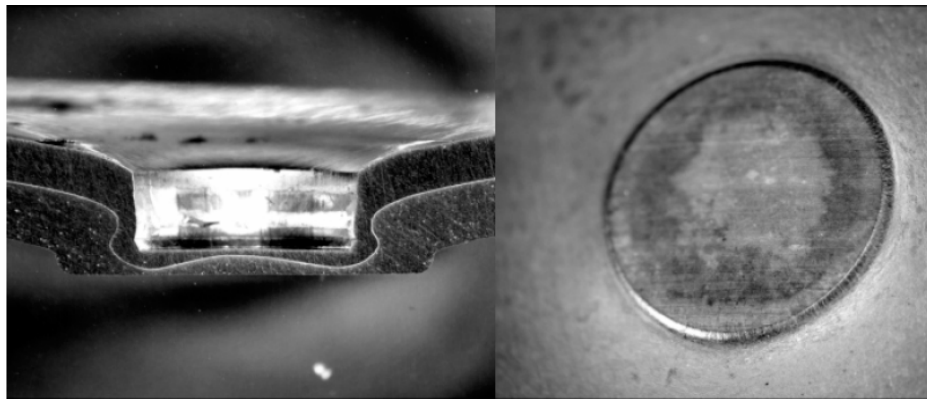


Fig. 11. Cross section and anvil-sided view of a dieless clinch-connection of AlMg3 ($t_1 = 1.0$ mm) with magnesium AZ31 ($t_2 = 1.3$ mm) – joined with heated anvil

3.2. Flat-clinch-connections

The creation of interlocking needs the well-directed control of material flow inside the part thickness. This can be realized by using special punch- and blank-holder geometries. Figure 12 shows examples of experimental investigated punch and blank-holder geometries. A view of a connection manufactured with angular shaped punch is shown in Figure 13. Anvil-sided a slight texturing is visible, but flatness of less than 50 μm in height is reachable with this technology, depending on component materials, their combination and thicknesses.

Applications for this type of connection are cases where protrusions are visibly or functionally disturbing, e.g. to apply sealing strips (welting) or piling up the joined parts.

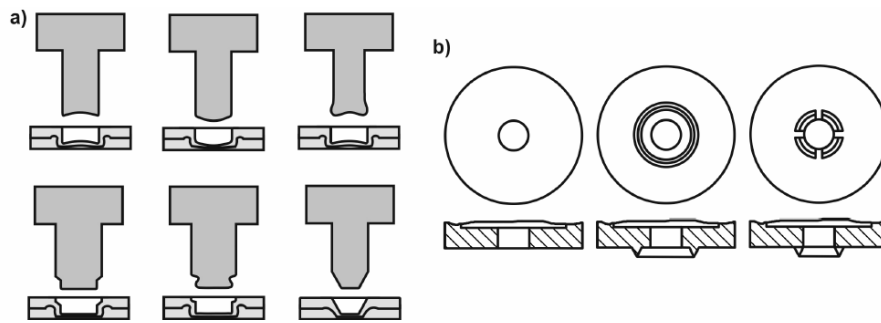


Fig. 12. Examples of a) punch and b) blank-holder geometries of experimental investigations

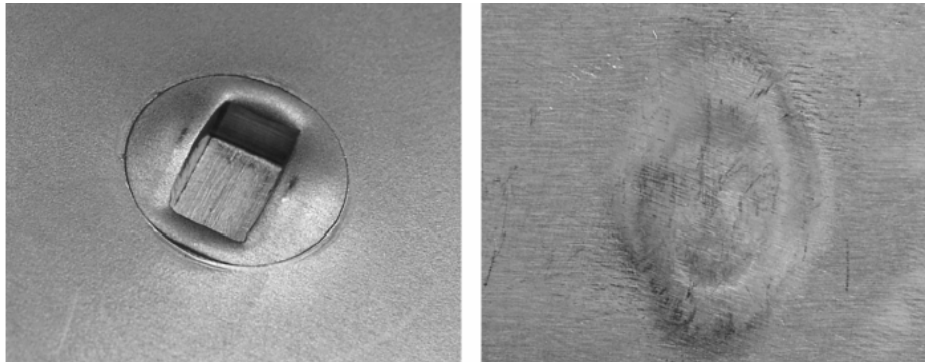


Fig. 13. View of punch-side (left) and anvil-side (right) of a flat-clinch-connection at AlMg3 (2.0 mm)

3.3. Dieless rivet-clinch connections

Investigations of dieless rivet-clinch connections are related to the development of an optimal shape and hardness of the rivets taking into consideration best connection

properties (e.g. interlocking, connection strength). Figure 14 shows dependency of interlocking on hardness for 3 different rivet shapes.

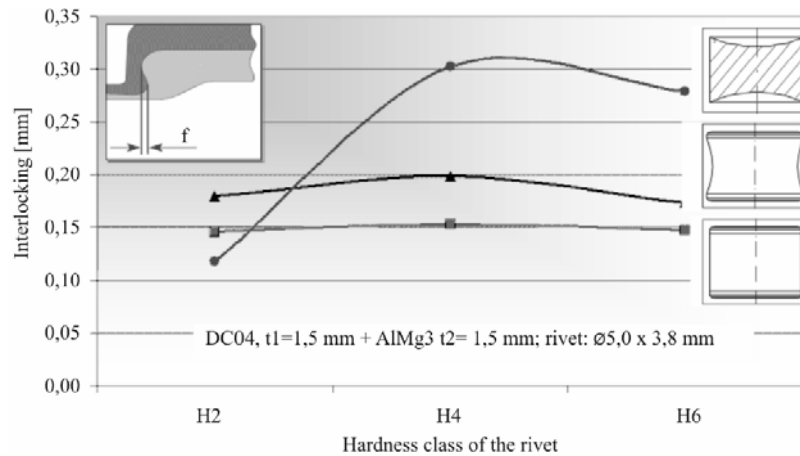


Fig. 14. Dependence of connection interlocking on the hardness class of the rivet of dieless rivet-clinch connections

4. Conclusion

State-of-the-art joining by forming methods (such as clinching or self-pierce riveting) is usually working with a contoured die as a counter tool. In contrast to them the shown dieless joining by forming methods has various advantages. It is possible to create connections without anvil-sided protrusions, what makes them suitable for functional component areas. Dieless clinching allows even joining of brittle magnesium by locally heating it. The necessary heating time can be reduced considerably in comparison to conventional joining by forming operations with contoured die. But most important fact is that all shown technologies have equivalent economic efficiency compared to the conventional mechanical joining processes using a die.

References

- [1] Ruther, M.: *Fügetechnische Herausforderungen im Fahrzeugbau durch neue Werkstoffe*, [Challenges of joining at automotive industry because of new materials], DVS-Berichte, Band 232, Düsseldorf: DVS-Verlag, 2004, pp. 276–282.
- [2] N.N.: *Neue Werkstoffe verändern die Fügetechnik*, [New materials changing joining technology], In: *Blech, Rohre, Profile*, Band 53, 2006, 4, pp. 53–54.
- [3] Büdgam, S., Freitag, V., Hahn, O., Ruther, M.: *Fügesystemoptimierung für Mischbauweisen im Karosseriebau*, [Optimization of joining systems for multi material design in car body manufacturing], In: *Automobiltechnische Zeitschrift – ATZ*, Band 106, 2004, 12, pp. 1132–1136.

- [4] Neugebauer, R., Mauermann, R., Dietrich, S.: *Chances and challenges in joining by forming with a flat countertool*, 11th International Conference on Sheet Metal, Erlangen, 5–8. April, 2005, pp. 203–208.
- [5] Dietrich, S.: *Grundlagenuntersuchungen zu neuen matrizenlosen Umformfügeverfahren*, [Basic investigations of new dieless mechanical joining technologies. PhD-work], Dissertationsschrift, Chemnitz University of Technology, 2007.
- [6] Neugebauer, R., Dietrich, S., Kraus, C.: *Joining by forming with a flat counter tool – A new way of joining magnesium components*, In: Materials Science Forum 2007, 539–543, pp. 3949–3954.
- [7] Matthes, K.-J., Riedel, F., Todtermuschke, M.: *Verfahren und Einrichtung zur Herstellung einer Verbindung zwischen sich überlappenden plattenförmigen Bauteilen*, [Process and device for manufacturing connections between overlapping component parts], Patent: DE 101 30 726 C2, Deutsches Patent- und Markenamt, 2003.
- [8] Todtermuschke, M.: *Verfahrensoptimierung zur Herstellung einer punktförmigen, mechanisch gefügten, einseitig ebenen Verbindung ohne Verbindungselement*, [Optimization of technology for manufacturing dot-shaped, mechanical joined one-sided flat connections without ancillary parts], PhD-work, Chemnitz University of Technology, 2006.
- [9] Riedel, F., Todtermuschke, M., Awiszus, B., Beyer, U.: *Flat-clinch connection - a new connection with plane surface of die side*, 2nd International Conference on New Forming Technology (ICNFT), Bremen, 20–21. September, 2007, pp. 441–450.
- [10] Dietrich, S., Mauermann, R., Jesche, F., Lachmann, L.: *Verfahren, Vorrichtung und Hilfsfügeteil zum Fügen von mindestens zwei Bauteilen*, [Process, device and ancillary part for joining of at least two component parts], Unexamined laid-open patent application no.: DE 102 13 793 A1, Deutsches Patent- und Markenamt, date of filing 27th March, 2002.
- [11] Neugebauer, R.; Dietrich, S.; Kraus, C.: *Dieless clinching and dieless rivet-clinching of magnesium*, In: Key Engineering Materials, 2007, 344, pp. 693–698.
- [12] Hollerung, T.: *Verfahren und Vorrichtung zum Verbinden von Werkstoffen durch Stanznieten*, [Process and device for joining materials by self-piercer riveting. Patent], No.: DE 199 05 528 B4, Deutsches Patent- und Markenamt, 2007.

Przegląd rozwoju i zastosowań bezmatrycowych mechanicznych procesów łączenia

Publikacja zawiera przegląd rozwoju i potencjalnego zastosowania mechanicznego łączenia z praktycznymi przykładami. Obecnie intensywnie rozwijane są różne technologie mechanicznego łączenia, gdzie matryca jako przeciwstempel (wypychacz) została zastąpiona przez płaskie kowadło. Używając bezmatrycowego klinczowania, pojawia się kilka korzyści dla alternatywnych procesów, na przykład możliwe jest wyprodukowanie jednostronnych płaskich połączeń. Dodatkowo zastosowanie technologii mechanicznych połączeń może zostać rozszerzone na elementy z magnezu, które mogą zostać częściowo podgrzane i bezpośrednio połączone. Koszty narzędzi i ich zużycie jest znacząco mniejsze niż w innych metodach łączenia.



Linear analysis of laminated multilayered plates with the application of zig-zag function

A. SABIK, I. KREJA

Gdańsk University of Technology, G. Narutowicza 11/12, 80-952 Gdańsk, Poland

An Equivalent Single Layer Model for linear static analysis of multilayered plates is considered in the paper. The displacements field of the First Order Shear Deformation Theory is supplemented with the Murakami's function to emulate the zig-zag effect. The applied Reissner's Mixed Variational Theorem allows to assume an independent shear stress field of parabolic distribution in each layer and to satisfy the equilibrium conditions at the layer interfaces. The Finite Element implementation of the model is based on the application of the 9-node Lagrangian element with a selective reduced integration. Two numerical examples of symmetrically laminated plates are presented to illustrate the accuracy of presented approach.

Keywords: *multilayered plates, zig-zag effect, interlaminar continuity*

1. Introduction

A high strength, a light weight, good thermal insulation and a superior durability are the most characteristic attributes of multilayered plates. These features are very desirable in many branches of industry. Initially, the technology of these heterogeneous structures was developed with intent to meet the particular requirements of the aeronautic engineering. However, decreasing cost of their production in recent years is the reason behind the popularity of multilayered plates in other branches, also in the civil engineering. Therefore, the problem of modelling such structures is a usual task of many structural engineers of today.

The formulation of mechanical model of multilayered plates causes however more difficulties in comparison with the case of homogeneous plates. For example, a question arises how to describe the changes of material properties over the cross-section. Is it necessary to assume independent displacement and stress fields for each layer, or maybe, it is possible to replace the sequence of the laminas by some equivalent single layer? In addition, due to low and different transverse stiffness of adjacent layers, the cross-section's deformation takes the form of a zig-zag. This is known as the 'zig-zag effect' [1, 2], a recognized problem related to modelling of multilayered structures. Consequently, the assumption of linear deformation of the cross-section is inadequate here. Furthermore, due to the assumption of the perfect bond between the layers, the fulfilment of equilibrium conditions at the layer interfaces is required. It means that the distribution of transverse stresses along the plate thickness should be described by continuous functions. Literature known this as the 'interlaminar continuity' [1].

The above facts complicate the formulation of computational models for multilayered structures. In the literature, one can find a multitude of approaches to overcome these difficulties. Some of them are: the three-dimensional formulations, the so called ‘Layer-Wise’ (LW) [3] approach where independent displacement and stress fields for each layer are assumed, or ‘Equivalent Single Layer Models’ (ESL) [3], where a single layer with a resultant stiffness is applied. Another classification follows from computational technique applied to solve the governing equations. Nowadays the most popular tool is the Finite Element Method (FEM). Here, the differences among various concepts result from the underlying weak formulation of the problem, for instance virtual displacements or multi-field variational principle. For the systematic review – see references [4, 5].

The aim of the present paper is to outline the formulation of the model (see, [6] for details) that belongs to the family of ESL formulations. Starting from the First Order Shear Deformation Theory (FSDT) additional assumptions are made in order to account for both the ‘zig-zag effect’ and the ‘interlaminar continuity’. In the computations, the Finite Element Method is applied. To illustrate the performance of the model in linear static analysis, two numerical examples are presented.

2. Characteristic of the model

As mentioned above, the presented formulation belongs to the group of ESL models. This approach is based on reduction of a three-dimensional solid to a two-dimensional midsurface, as in case of homogeneous plates. This means that only one displacement field and one stress field are assumed for the whole cross-section.

2.1. Displacement field

The displacement distribution through the plate thickness is a sum of linear distribution (FSDT) and Murakami’s zig-zag function (Figure 1). The Murakami’s function is defined as follows:

$$f(z) = (-1)^k \cdot \zeta_k,$$

$$\zeta_k = 2z_k/h_k, \tag{1}$$

$$k = 1, 2 \dots N_L.$$

where ζ_k , z_k are non-dimensional and dimensional coordinate of the layer k , respectively, h_k is the thickness of the layer k , and N_L stands for the number of layers.

It can be clearly seen, that the function (1) changes the slope at the layer interfaces. Its introduction to the displacement field is a simple way to simulate the ‘zig-zag

effect'. More details about properties of Murakami's function can be found in [1]. Other approaches used to describe the 'zig-zag effect' are discussed in [7].

As a result, the standard five-parameter displacement field of FSDT, is enhanced by two additional variables:

$$\begin{aligned} u(x, y, z) &= u_o(x, y) + \varphi_x(x, y) + (-1)^k \cdot \zeta_k \cdot D_x(x, y), \\ v(x, y, z) &= v_o(x, y) + \varphi_y(x, y) + (-1)^k \cdot \zeta_k \cdot D_y(x, y), \\ w(x, y, z) &= w_o(x, y), \end{aligned} \quad (2)$$

where u_o , v_o , w_o are translations of midsurface points in x , y and z -axis direction, respectively (Figure 2), φ_x , φ_y are rotations in x - z and y - z surfaces. The additional parameters D_x , D_y can be interpreted as amplitudes of the Murakami's function. It can be seen from (2) that the transverse normal strain effect is omitted.

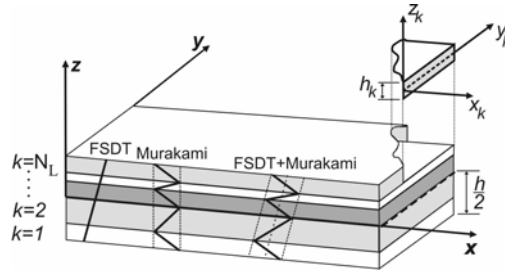


Fig. 1. Displacement field

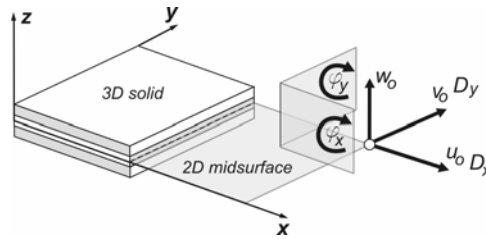


Fig. 2. Coordinate system and degrees of freedom

2.2. Stress field

Bending stresses are evaluated following standard displacement formulation. However, there is a necessity to adopt an independent field of transverse stresses to satisfy the required equilibrium conditions at layer interfaces. Since the effect of transverse normal strain is not taken into account, the assumption of an independent field is made

only with the reference to the transverse shear stresses. The shear stress field for each layer is determined by six unknowns assembled in vector $\mathbf{X}_{\sigma,k}$:

$$\mathbf{X}_{\sigma,k}^T = \left\{ \sigma_{xz}^t \quad \sigma_{yz}^t \quad R_{xz} \quad R_{yz} \quad \sigma_{xz}^b \quad \sigma_{yz}^b \right\}_k^T, \quad (3)$$

where indices t , b denote the top and bottom surface of layer k , respectively and R_{xz} , R_{yz} are stress resultants given by:

$$R_{iz} = \int_{h_k} \sigma_{iz} dz, \quad i = x, y. \quad (4)$$

The distribution of shear stresses in layer k follows from interpolation scheme

$$\boldsymbol{\sigma}_{s,k} = \left\{ \begin{matrix} \sigma_{xz} \\ \sigma_{yz} \end{matrix} \right\}_k = \begin{bmatrix} F_o & 0 & F_1 & 0 & F_2 & 0 \\ 0 & F_o & 0 & F_1 & 0 & F_2 \end{bmatrix}_k \cdot \mathbf{X}_{\sigma,k}, \quad (5)$$

where $\mathbf{X}_{\sigma,k}$ are given in (3) and the interpolating functions are defined as:

$$\begin{aligned} F_o(\xi_k) &= -\frac{1}{4} + \frac{\xi_k}{2} + \frac{3}{4}\xi_k^2, \\ F_1(\xi_k) &= \frac{3 \cdot (1 - \xi_k^2)}{2 \cdot h_k}, \\ F_2(\xi_k) &= -\frac{1}{4} - \frac{\xi_k}{2} + \frac{3}{4}\xi_k^2. \end{aligned} \quad (6)$$

Due to the stress continuity requirements, the distribution of the stress field through the whole cross-section need to satisfy the following conditions:

$$\begin{aligned} \sigma_{xz,k}^t &= \sigma_{xz,k+1}, \\ \sigma_{yz,k}^t &= \sigma_{yz,k+1}^b, \end{aligned} \quad (7)$$

$$k = 1, 2, \dots, N_L - 1.$$

Moreover, additional assumptions are made regarding the transverse shear stresses at the top and the bottom surfaces:

$$\begin{aligned}\sigma_{xz}(z = \pm h/2) &= 0, \\ \sigma_{yz}(z = \pm h/2) &= 0.\end{aligned}\quad (8)$$

Figure 3 illustrates the projections of assumed shear stress distribution through the cross-section:

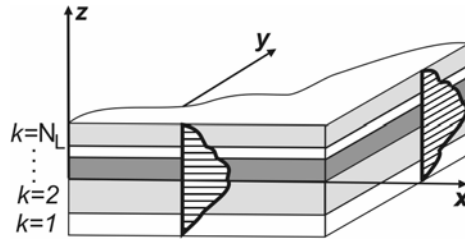


Fig. 3. Assumed shear stresses distribution σ_{xz} , σ_{yz}

2.3. Variational principle

A usual basis of any FEM model is some weak formulation of a particular mechanical problem. When the principle of minimum total potential energy [8] or virtual displacement method is applied as the weak form then the basic unknowns are displacements. An alternative way can be adopting the principle of minimum complementary energy or virtual forces method. In this case, the stresses are initial unknowns [3]. There is also another way, namely by applying mixed variational principles, e.g. Hellinger-Reissner or Hu-Washizu principle [9].

The internal energy functional W_{in} used in the present formulation reads [3]:

$$W_{in} = \int_A \left(\sum_{k=1}^{N_L} \int_{h_k} (\delta \boldsymbol{\varepsilon}_{\mathbf{b}}^T \cdot \boldsymbol{\sigma}_{\mathbf{b},H,k} + \delta \boldsymbol{\varepsilon}_{\mathbf{s}}^T \cdot \boldsymbol{\sigma}_{\mathbf{s},k} + \delta \boldsymbol{\sigma}_{\mathbf{s},k}^T \cdot (\boldsymbol{\varepsilon}_{\mathbf{s}} - \boldsymbol{\varepsilon}_{\mathbf{s},H})) \right) dz dA, \quad (9)$$

where $\boldsymbol{\varepsilon}$, $\boldsymbol{\sigma}$ are strain and stress vectors, respectively; indices \mathbf{b} , \mathbf{s} denote correspondingly bending and shear terms; k is the layer number, A is midsurface area and H indicates terms obtained from the Hooke's law. Transverse shear stresses are computed as described in paragraph 2.2. Bending and shear energy are the first and the second term respectively. The last term in (9) represents the condition of shear stress compatibility at layer interfaces. The form of the relation in parenthesis results from simple transformations based on the assumption that

$$\boldsymbol{\sigma}_{s,k,H} = \mathbf{D}_k \boldsymbol{\varepsilon}_s \text{ and } \boldsymbol{\varepsilon}_{s,H} = \mathbf{D}_k^{-1} \boldsymbol{\sigma}_{s,k}, \quad (10)$$

what allows to write

$$\boldsymbol{\sigma}_{s,k} = \boldsymbol{\sigma}_{s,k,H} \Rightarrow \boldsymbol{\varepsilon}_{s,H} = \boldsymbol{\varepsilon}_s \Rightarrow \int_{h_k} \delta \boldsymbol{\sigma}_{s,k}^T \cdot (\boldsymbol{\varepsilon}_s - \boldsymbol{\varepsilon}_{s,H}) dz = 0. \quad (11)$$

A proper classification of the variational principle (9) is somewhat problematic, because at first there are two kinds of unknowns, namely displacements and shear stresses, but due to the condition (11) stresses are eliminated from unknowns. This approach was proposed by Eric Reissner in the 1980' and therefore is known as Reissner's Mixed Variational Theorem (RMVT) [3]. It should be noticed that the stress elimination must be carried out on cross-section level satisfying conditions (7) and (8) (compare [6]).

3. Numerical examples and discussion

Two numerical examples are given below to illustrate the performance of the considered model. As discussed in 2.3, the resulting finite element formulation based on the above assumptions possesses only seven kinematical degrees of freedom, given in (2). In the analysis, the 9-node Lagrangian element was applied. In order to avoid locking effect [8], the selective reduced integration [10] was used to obtain element's matrices. The results obtained within the framework of the present formulation are taken from [11].

3.1. Simple supported square sandwich plate

Following [5] a square, simply supported sandwich plate under uniform distributed load q is investigated (Figure 4).

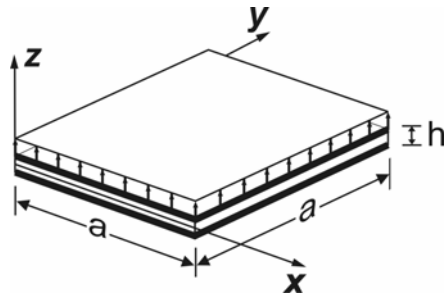


Fig. 4. Square sandwich plate

The layers have following parameters: skins – $h_o = 0.1h$, $E_1/E_2 = 25$, $G_{12}/E_2 = G_{13}/E_2 = 0.5$, $G_{23}/E_2 = 0.2$, $\nu_{12} = 0.25$; inner layer – $h_w = 0.8h$, $E_1/E_2 = 1$, $G_{13}/E_2 = G_{23}/E_2 = 0.06$, $G_{12}/E_2 = 0.016$, $\nu_{12} = 0.25$. Maximal values of deflection, normal and shear stresses were obtained for various a/h ratios. Shear stresses are evaluated by integrating three-dimensional equilibrium equations as follows:

$$\begin{aligned}\sigma_{xz} &= -\sum_{k=1}^{N_l} \int_{h_k} (\sigma_{xy,y} + \sigma_{xx,x}) dz, \\ \sigma_{yz} &= -\sum_{k=1}^{N_l} \int_{h_k} (\sigma_{xy,x} + \sigma_{yy,y}) dz.\end{aligned}\tag{12}$$

Non-dimensional values are introduced as:

$$w^* = w \cdot 100 \cdot E_2 \cdot h^3 / (q \cdot a^4),$$

$$\sigma_{xx}^* = \sigma_{xx} / (q \cdot (a/h)^2),$$

$$\sigma_{xz}^* = \sigma_{xz} / (q \cdot (a/h)).$$

To discuss the effectiveness of the presented formulation the obtained solutions are compared in Tables 1, 2 and 3 with results calculated with other models. The error value in Tables 1, 2 and 3 ($\varepsilon = |w^* - w_{ref}^*| / w_{ref}^* \cdot 100\%$) is evaluated with respect to the reference solution obtained using the LW-type approach LM4 [5], which is basing on the variational formulation (9) but using the fourth order polynomial description of the displacement and transverse stress distribution through the layer thickness. ED4 and FSDT denote ESL only displacement formulations with displacement field given by fourth and first order polynomial, respectively. It should be noticed that LM4 and ED4 take into account the transverse normal deformability of the plate. ‘Zig-zag effect’ and ‘interlaminar continuity’ are satisfied only by the LM4 and the present model.

Table 1. Comparison of deflection results for sandwich plate

Model	$w^*(x = a/2, y = a/2) [-]$					
	$a/h = 4$	ε	$a/h = 10$	ε	$a/h = 100$	ε
		[%]		[%]		[%]
LM4 [5]	10.682		3.083		1.262	
ED4 [5]	9.909	7.24	2.923	5.19	1.260	0.16
FSDT [5]	5.636	47.24	1.984	35.65	1.218	3.49
Present results	10.698	0.15	3.087	0.13	1.262	0.00

Table 2. Comparison of normal stresses results for sandwich plate

Model	$\sigma_{xx}^* (x = a/2, y = a/2, z = h/2) [-]$					
	$a/h = 4$	ε	$a/h = 10$	ε	$a/h = 100$	ε
		[%]		[%]		[%]
LM4 [5]	1.902		1.509		1.505	
ED4 [5]	1.929	1.42	1.519	0.66	1.506	0.07
FSDT [5]	1.168	38.59	1.391	7.82	1.476	1.93
Present results	1.905	0.13	1.503	0.40	1.506	0.07

Table 3. Comparison of shear stresses results for sandwich plate

Model	$\sigma_{xz}^* (x = 0, y = a/2, z = 0) [-]$					
	$a/h = 4$	ε	$a/h = 10$	ε	$a/h = 100$	ε
		[%]		[%]		[%]
LM4 [5]	0.4074		0.5276		0.5889	
ED4 [5]	0.3574	12.27	0.5104	3.26	0.5881	0.14
FSDT [5]	0.5249	28.84	0.5716	8.34	0.5876	0.22
Present results	0.3949	3.07	0.5245	0.59	0.5968	1.34

The contents of the Tables 1, 2 and 3 allow one to conclude that the accuracy of the present solutions is very satisfying. Only the shear stress result in the case of the thin plate ($a/h=100$) is less precise than values evaluated from ED4 and FSDT. However, the received error level in this case is still quite low. The significant differences between the present solutions and FSDT [5] emphasize the importance of consideration both the ‘zig-zag effect’ and ‘interlaminar continuity’ in modeling of multilayered structures. It can be also observed, that presented approach is more effective than ED4 [5]. High accuracy (low relative error ε) in the case of thick plate could be a consequence of low transverse normal deformability of the cross-section.

3.2. Simple supported square cross-ply plate

This is a classical benchmark proposed by Pagano and Hatfield [12] and investigated by many other authors (see e.g. [13]). Displacement and stress state of 9-layers (0/90/0/90/0/90/0/90/0), simply supported, square plate are analysed (Figure 5).

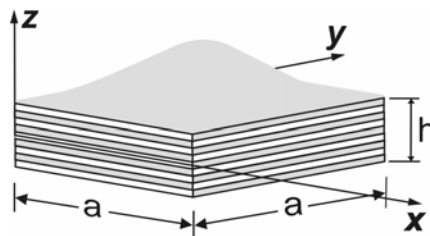


Fig. 5. Square cross-ply plate

The parameters of each lamina are following: $E_L = 172.375E6$ kPa, $E_T = 68.95E5$ kPa, $G_{LT} = 3.4475E6$ kPa, $G_{TT} = 1.379E6$ kPa, $\nu_{LT} = \nu_{TT} = 0.25$. The layers of the same orientation have equal thickness. The total thickness of 0° and 90° laminas is identical. The study was made with respect to several proportions a/h . The plate is loaded by bi-sinusoidal pressure:

$$p = p_o \cdot \sin\left(\frac{\pi x}{a}\right) \cdot \sin\left(\frac{\pi y}{a}\right).$$

The results are given in non-dimensional form according to:

$$w^* = \pi^4 Q_w / (12S^4 h p_o), \quad \sigma_{xx}^* = \sigma_{xx} / (p_o S^2), \quad \sigma_{xz}^* = \sigma_{xz} / (p_o S), \quad S = a/h,$$

$$Q = 4G_{LT} + [E_L + E_T(1 + 2\nu_{TT})] / (1 - \nu_{LT}\nu_{TL}).$$

Tables 4, 5 and 6 include present results confronted with the 3D solution given by Pagano and Hatfield [12].

Table 4. Comparison of deflection results for cross-ply plate

Model	$w^*(x = a/2, y = a/2) [-]$					
	$a/h = 10$	ε	$a/h = 20$	ε	$a/h = 50$	ε
		[%]		[%]		[%]
3D [12]	1.512		1.129		1.021	
Present results	1.441	4.70	1.112	1.51	1.018	0.29

Table 5. Comparison of normal stresses results for cross-ply plate

Model	$\sigma_{xx}^*(x = a/2, y = a/2, z = h/2) [-]$					
	$a/h = 10$	ε	$a/h = 20$	ε	$a/h = 50$	ε
		[%]		[%]		[%]
3D [12]	0.551		0.541		0.539	0.551
Present results	0.516	6.35	0.531	1.85	0.537	0.37

Table 6. Comparison of shear stresses results for cross-ply plate

Model	$\sigma_{xz}^*(x = 0, y = a/2, z = 0) [-]$					
	$a/h = 10$	ε	$a/h = 20$	ε	$a/h = 50$	ε
		[%]		[%]		[%]
3D [12]	0.247		0.255		0.258	
Present results	0.243	1.62	0.254	0.39	0.258	0.00

The comparison given in Tables 4, 5 and 6 seems to confirm the good accuracy of the presented formulation in the analysis of thin and moderately thick symmetrically laminated plates similarly, as observed in the previous example 3.1. Nevertheless, here

the discrepancies between the present results and the reference solution are more pronounced. This may be attributed to the fact that the reference solution is a three-dimensional one. In addition, the differences may result from poor spatial approximation of the load in case of present computations. By comparing error values in Tables 4, 5 and 6, one can easily observe that the effectiveness of the model is lowest in the case of normal stresses. This is noteworthy, because normal stresses are evaluated according to the displacement field (from Hooke's law). Furthermore, following (12), shear stresses depend on normal stress results. Nevertheless, it should be reminded that the both stress fields in FEM-computations are obtained by using different derivatives of shape functions. Maybe this fact could be an explanation for this significant error distribution. Moreover, this example illustrates clearly that the accuracy of the presented model deteriorates with the decreasing ratio a/h . One can make conclusion that the correctness of this formulation in the case of thick plates depends strictly on the intensity of transverse normal strain effect (see 3.1).

4. Conclusions

The paper presents theoretical foundations and numerical investigations of two-dimensional FEM model for multilayered plates. The basis of the demonstrated approach is the First Order Shear Deformation Theory (FSDT). Two additional degrees of freedom of piecewise continuous distribution through the plate thickness are introduced to simulate the 'zig-zag effect'. The formulation accounts for the 'interlaminar continuity' requirement by means of the two-field variational principle, commonly known as the Reissner's Mixed Variational Theorem (RMVT). Due to the shear stress continuity condition the stress' unknowns are eliminated at element level. Therefore, the resulting finite element possesses only kinematical degrees of freedom. Two numerical examples of symmetrically laminated plates are presented to demonstrate the efficiency of the model. A 9-node Lagrangian element with seven degrees of freedom in each node is used in computations. The obtained results prove that the presented approach can be very effective tool in investigations of thin and moderately thick symmetrically laminated plates.

References

- [1] Demasi L.: *Refined multilayered plate elements based on Murakami zig-zag functions*, Composite Structures, Vol. 70, 2005, pp. 308–316.
- [2] Carrera E.: *Historical review of Zig-Zag theories for multilayered plates and shells*, Appl. Mech. Rev., Vol. 56, 2003, pp. 287–308.
- [3] Carrera E.: *Developments, ideas, and evaluations based upon Reissner's Mixed Variational Theorem in the modeling of multilayered plates and shells*, Appl. Mech. Rev., Vol. 54, 2001, pp. 301–329.

- [4] Rohwer K., Friedrichs S., Wehmeyer J.N.: *Analyzing Laminated Structures from Fibre-Reinforced Composite Material – An Assessment*, Technische Mechanik, Vol. 25, 2005, pp. 59–79.
- [5] Carrera E., Ciuffreda A.: *A unified formulation to assess theories of multilayered plates for various bending problems*, Composite Structures, Vol. 69, 2005, pp. 271–293.
- [6] Brank B., Carrera E.: *Multilayered shell finite element with interlaminar continuous shear stresses: a refinement of the Reissner-Mindlin formulation*, International Journal for Numerical Methods in Engineering, Vol. 48, 2000, pp. 843–874.
- [7] Di S., Rothert H.: *Solution of a laminated cylindrical shell using an unconstrained third-order theory*, Computers and Structures, Vol. 69, 1998, pp. 291–303.
- [8] Reddy J.N.: *Energy Principles and Variational Methods in Applied Mechanics*, John Wiley & Sons Canada, Ltd., Toronto, 2001.
- [9] Ramm E.: *From Reissner plate theory to three dimensions in large deformations shell analysis*, Zeitschrift für Angewandte Mathematik und Mechanik, Vol. 80, 2000, pp. 61–68.
- [10] Zienkiewicz O.C., Taylor R.L., Too J.M.: *Reduced Integration Technique in general analysis of plates and shells*, International Journal for Numerical Methods in Engineering, Vol. 3, 1971, pp. 275–290.
- [11] Witkowska(-Sabik) A.: *Numerical model of the multilayered plate with the use of zig-zag function (in Polish)*, M.Sc. thesis, supervisor I. Kreja, Faculty of Civil and Environmental Engineering, Gdansk University of Technology, Gdańsk, 2006.
- [12] Pagano N.J., Hatfield S. J.: *Elastic behaviour of multilayered bidirectional composites*, American Institute of Aeronautics and Astronautics Journal, Vol. 10, 1972, pp. 931–933.
- [13] Bogdanovich A.E., Yushmanov S.P.: *Three-dimensional variational analysis of Pagano's problems for laminated composite plates*, Composites Science and Technology, Vol. 60, 2000, pp. 2407–2425.

Analiza liniowa laminowanych płyt warstwowych z zastosowaniem funkcji zig-zag

W pracy analizowany jest dwuwymiarowy model MES płyty warstwowej bazujący na teorii ścinania pierwszego rzędu, w którego sformułowaniu uwzględnione są dodatkowo efekt zig-zag oraz warunki równowagi międzywarstwowej. Zygzakowa deformacja przekroju modelowana jest poprzez wzbogacenie liniowego rozkładu przemieszczeń teorii ścinania pierwszego rzędu kawałkami ciągłą funkcją Murakami'ego. Pole przemieszczeń w prezentowanym sformułowaniu jest określone poprzez siedem stopni swobody. Spełnienie warunków równowagi na granicach warstw jest możliwe dzięki przyjęciu niezależnego, ciągłego w przekroju płyty rozkładu naprężeń poprzecznego ścinania. Efekt poprzecznego rozciągania jest w modelu pominięty. Dodatkowy warunek zgodności naprężeń na stykach warstw umożliwia wyeliminowanie niewiadomych naprężeniowych z zestawu niewiadomych. Eliminacja przeprowadzana jest na poziomie całego przekroju przy uwzględnieniu warunków ciągłości naprężeń na granicach warstw oraz ich braku na zewnętrznych powierzchniach płyty. Odpowiadający element skończony posiada jedynie kinematyczne stopnie swobody.

W artykule przedstawiono podstawy teoretyczne modelu z odniesieniem do traktujących o nim pozycji literatury. Zawarto dwa zaczerpnięte z dostępnych źródeł przykłady numeryczne, na podstawie, których przeprowadzono dyskusję efektywności prezentowanego podej-

ścia w zakresie statycznej analizy liniowej płyt symetrycznie uwarstwionych. Wyniki własne otrzymano przy zastosowaniu 9-węzłowego elementu Lagrange'a. Ponieważ elementy skończone zbudowane na bazie założeń prezentowanego modelu nie są wolne od efektu blokady, podczas całkowania macierzy sztywności elementów stosowano technikę całkowania selektywnie zredukowanego. Z porównania uzyskanych wyników z rozwiązaniami odniesienia wynika, że badany model bardzo skutecznie oddaje zachowanie cienkich i umiarkowanie grubych symetrycznie uwarstwionych płyt warstwowych.



Application of artificial neural networks in predicting earthmoving machinery effectiveness ratios

K. SCHABOWICZ, B. HOŁA

Wrocław University of Technology, Wybrzeże Wyspiańskiego 27, 50-370 Wrocław

Many constructional processes are carried out by machines working together and forming technological systems. An example here can be an earthmoving machinery set made up of excavators and means of transport. For process design purposes most important are the effectiveness ratios relating to the profits and losses stemming from system use, i.e. the system efficiency per unit work ratio $W_{(N)}$; the index of losses due to the idle times of the machines working in the system S_j ; the output transport unit cost index K_j . This paper presents the results of applying neural networks in predicting effectiveness ratios, i.e. $W_{(N)}$, S_j and K_j for earthmoving machinery systems consisting of c excavators and N means of transport. It is showing the relevance to practitioners and researchers industry. The values of the characteristics can form a standard basis for designing construction earthworks. Having a dataset consisting of the technical parameters of earthmoving machinery systems and the corresponding effectiveness ratios one can train neural networks and then use the latter for the reliable prediction of $W_{(N)}$, S_j and K_j .

Keywords: *earthwork, efficiency, losses, costs, neural networks*

1. Introduction

Many constructional processes are carried out by machines working together and forming technological systems (also referred to as technological sequences or chains). An example here can be an earthmoving machinery set made up of excavators and means of transport [14, 16]. The actual amount of work needed to carry out a specific task depends on, among other things, the number and configuration of the machines involved, their technical parameters and the influence of the external environment on the system. The machines operating in a system should be selected with regard to their number and technical parameters so that their work is harmonized in terms of efficiency, reliability, place and time.

The interaction between the machines in most sets of machinery found on a building site can be analysed from a systemic perspective, using queuing theory [4, 5]. A systemic analysis of constructional processes allows one to assess the effectiveness of an investigated process, taking into account the probabilistic nature of operation execution time. A system operation effectiveness assessment can be made if one knows the following characteristics [3, 8]: service channel occupancy times, the number of arrivals serviced during service channel occupancy, the time the arrivals wait for service and the number of arrivals waiting to be serviced.

For process design purposes most important are the effectiveness ratios relating to the profits and losses stemming from system use, i.e.

- the system efficiency per unit work ratio, $W_{(N)}$,
- the index of losses due to the idle times of the machines working in the system, S_j ,
- the output transport unit cost index, K_j .

The analytical solutions of queuing system models are relatively simple when the latter are single-phase models (with one or many service channels), the flow of arrivals is of the Poisson type and the distribution of service durations is exponential or of the Erlang type [8]. In order to use such models one needs to have proper computer software capable of performing a large number of calculations in a short time for different configurations of machines operating in a system. If, however, the distribution of service times and interarrival times is an arbitrary distribution, the single-phase models are solved by simulation methods [8, 15, 21]. In latter case, the computer program simulating the system's operation is much more complicated and the computation time is much longer.

It is essential that the type of service and interarrival time distribution be determined by time studies. The introduction of new sets of machinery or the realization of the works in different environmental conditions makes it necessary (for both the analytical model and the simulation model) to carry out new laborious studies of input and service times. This may pose a problem since it is often impossible to carry out such studies at the work design stage.

The above problem can be solved by employing artificial neural networks (ANNs), which through training can acquire an ability to predict – on the basis of exclusively the training data – output signals for designing sets of earthmoving machinery [1, 7, 19, 20, 22]. One should note that the basic feature which distinguishes ANNs from programs that algorithmically process information is their ability to generalize knowledge for new (previously unknown) data, i.e. data not presented during their training.

This paper presents the results of applying artificial neural networks in predicting effectiveness ratios, i.e. $W_{(N)}$, S_j and K_j , for earthmoving machinery systems consisting of c excavators and N means of transport. The values of the characteristics can form a standard basis for designing construction earthworks. It is showing the relevance to practitioners and researchers industry.

2. Research methodology

The methodology schematically shown in Figure 1 was used demonstrate the usefulness of artificial neural networks for identifying efficiency $W_{(N)}$, unit cost K_j and unit loss S_j of earthmoving machinery systems.

According to Figure 1, the research consisted of two main stages. Stage 1 covered on-site investigations carried out for selected earthmoving machinery sets made up of excavators and haulers transporting spoil from the building site to an unloading site.

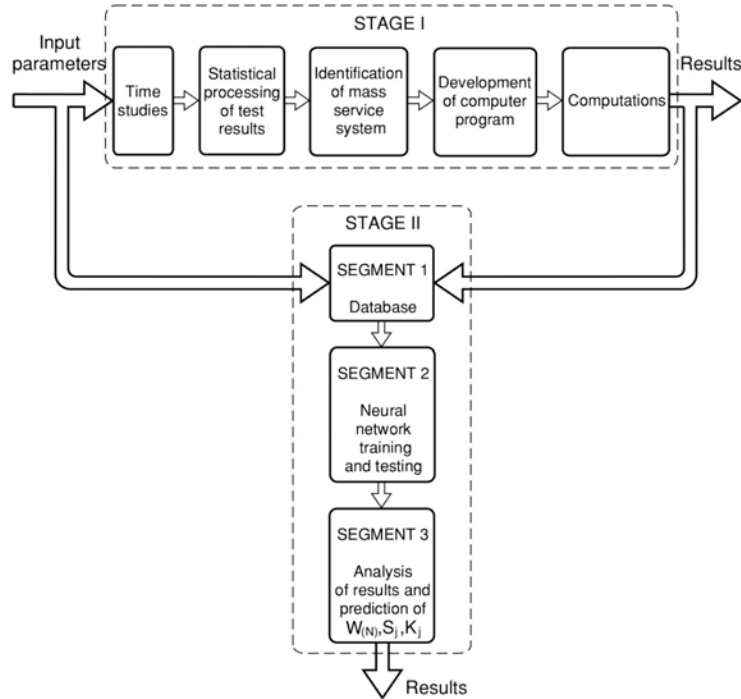


Fig. 1. Schema of research methodology

The investigations consisted in measuring excavator work cycle time t_z and hauler work cycle times t_j . The track loading platform capacity P_{jt} , excavator bucket capacity g_k , output transport distance L , type of road surface K_d , excavator work cycle time t_z , hauler work cycle time t_j , excavator work cost K_z , means of transport work cost K_s , number of excavators c and number of means of transport N operating in the system were the input parameters for this stage which included:

- studies of loading times and transport cycle times,
- statistical processing of time study results,
- identification of the process as a queuing system,
- construction of a computer simulator,
- computer computations which yielded effectiveness ratios: system efficiency $W_{(N)}$, unit loss S_j and unit cost K_j .

A single-phase, multichannel mass service system with: a Poisson arrival flow, an exponential distribution of service durations, a closed cycle of arrivals and *FIFO* queue rules was adopted. A diagram of the system is shown in Figure 2.

The system's efficiency is expressed by the formula:

$$W_{(N)} = c(1 - WP_{(A)})\mu P_{jt} t_i. \quad (1)$$

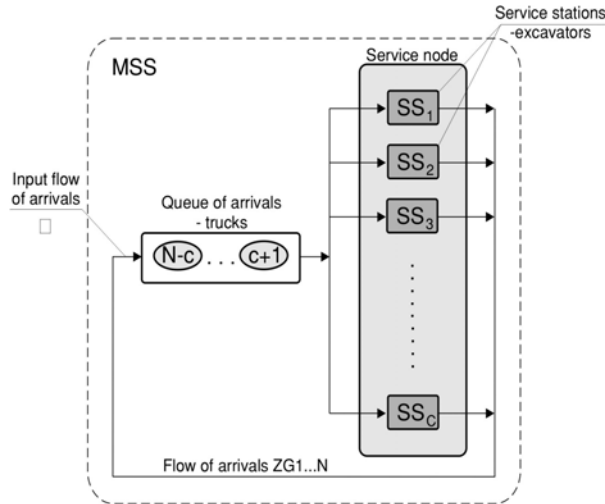


Fig. 2. Diagram of mass service system considered

The unit loss due to excavator and means of transport downtimes is given by the relation:

$$S_j = WP_{(A)}K_z + E(N)K_s \quad (2)$$

The output digging and transport unit cost is expressed by the relation:

$$K_j = (cK_z + NK_s) / cW_{(N)} \quad (3)$$

where:

μ – the average service rate,

P_{jt} – the truck loading platform capacity,

c – the number of excavators,

t_i – time instant i ,

N – the number of trucks,

K_s – means of transport work cost,

K_z – excavator work cost,

$WP_{(A)}$ – an excavator idle time coefficient,

EN_k – the average number of means of transport queuing up for all the service channels.

Knowing the values of the above characteristics for different sets of machinery and external environmental effects one can choose an optimal set. The values of the characteristics can be obtained from an analysis of the system's permissible states in the conducted process.

Stage II covered the construction of an artificial neural network, its training and testing and an analysis of the results. In order to design a system of ANNs for a particular task one needs to specify the network structure, i.e. determine the number of layers and the number of neurons in each layer, the parameter weights and the activation function coefficients.

A database made up of the technical parameters of the machinery systems (for which time studies had been carried out and the values of efficiency $W_{(N)}$, unit loss S_j and unit cost K_j had been calculated from relations (1), (2) and (3), was used to train the network. The database was divided into five sets. The division criterion was output transport distance which amounted to: 1, 2, 3, 5 and 7 km. The data sets were written to a computer file constituting segment 1 of stage II and then entered as input parameters for the neural networks into segment 2. Each data set was divided into two parts: a training set and a testing set.

Segment 2 of stage II (Figure 1) is the *MATLAB* computer program used for network simulations. A neural network type was chosen and a neural network was designed by experimentally determining its structure. The training patterns were fed randomly. The neural network training and testing results, including the network structure and the weight values, were saved to a file. The output data from segment 2 were analysed in segment 3 (Figure 1). First the data which the neural network was trained on were input and the ability to reproduce the training patterns was tested. Then the testing data were input and the identification was checked for correctness. The identified effectiveness ratios: $W_{(N)}$, S_j and K_j were obtained at the segment's output.

3. Structure of artificial neural network

The effectiveness of a mass service system depends on many technical parameters of its components and on the operating conditions. The main factors having a bearing on the system's effectiveness ratios include: transport unit loading time, transport unit work cycle time, the excavator bucket capacity, the transport unit loading platform capacity, the transport unit driving speed, the excavator bucket working speed, the kind of road surface, the category of the ground, the number of excavators working in the system, the number of transport units working in the system, the excavator work cost and the transport unit work cost.

Some of the input parameters were eliminated during the training process in order to obtain an optimal result. Ultimately, to train the neural network we adopted the following vectors:

$$W_{(N)} = \{c, N, g_k, P_{jt}, K_d\}, \quad (4)$$

$$S_j = \{c, N, g_k, P_{jt}, K_d\}, \quad (5)$$

$$K_j = \{c, N, g_k, P_{jt}, K_d\}, \quad (6)$$

where:

g_k – the excavator bucket capacity,

K_d – type of road surface.

As a result of training and testing, a network consisting of three unidirectional multilayer error back propagation networks with a conjugate gradient algorithm (BPNN-CGB) was constructed (Figure 3). This type of network was chosen since it is the most suitable for solving the considered problem [2, 6, 9–13, 23]. A nonlinear sigmoidal activation function was adopted. Each of the networks generated one result, i.e. the first network – $W_{(N)}$, the second network – S_j and the third network – K_j .

Table 1 shows exemplary values of the technical parameters of the machinery systems for which the time studies were carried out and the corresponding effectiveness ratio values yielded by the model simulating the working together of the machines. The values were used to predict efficiency $W_{(N)}$, unit loss S_j and unit cost K_j for an output transport distance of 2 km. The structural components of the adopted BPNN-CGB neural network are shown in table 2 [9–13]. The network structure is used to identify in turn: $W_{(N)}$, S_j and K_j at the particular output transport distances.

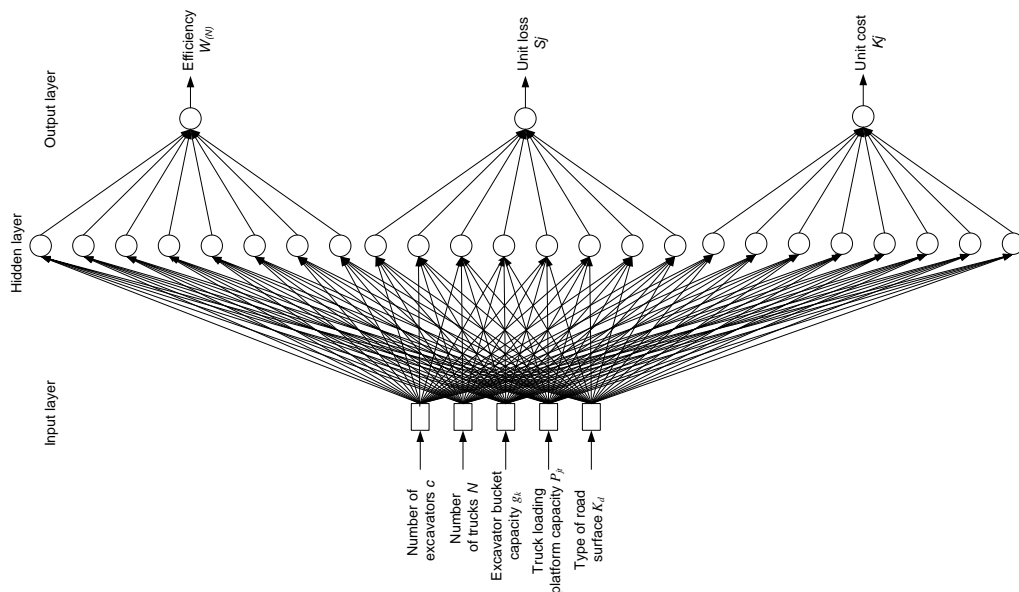


Fig. 3. Structure of adopted unidirectional multilayer error back propagation network with conjugate gradient algorithm (BPNN-CGB)

Since it was impossible to determine which parameters and modifications would give the best result, the different network elements were selected through training and testing. The following quantities: the number of hidden layers, the number of neurons in the hidden layer, the error threshold value and the number of training epochs were

modelled [9–13]. One should note that 200 patterns – 170 for training and 30 for testing – were used for each neural network.

During network modelling the so-called stop criteria were applied to the training process [9–13]. A network was considered well trained when:

- the values of the training and testing errors were the same or similar,
- the number of epochs at the assumed error value was the smallest,
- the correlation coefficient for data mapping was close to 1,
- the training and testing errors were below 15%,
- the standard deviation was below 12%.

Table 1. Exemplary values of parameters for predicting: efficiency $W_{(N)}$, unit loss S_j and unit cost K_j for output transport distance of 2 km

No.	Number of excavators $C [-]$	Number of trucks $N [-]$	Bucket capacity $g_k [m^3]$	Truck capacity $P_{jt} [m^3]$	Type of road category $K_d [-]$	Efficiency $W_{(N)} [m^3/h]$	Unit loss $S_j [zł/m^3]$	Unit cost $K_j [zł/m^3]$
1	2	6	2.5	12	2	133.33	670.68	18.83
2	3	38	2.5	12	2	392	5966	18.95
3	4	21	2.5	12	2	232.36	524.25	15.74
4	5	15	2.5	12	2	134.26	649.41	18.7
5	1	2	3.4	12	2	76.04	245.95	17.89
6	1	4	3.4	12	2	134.46	410.05	17.7
7	1	20	3.4	12	2	187.56	7792.07	56.2
8	2	2	5.6	12	2	42.89	723.4	31.71
9	2	4	5.6	12	2	85.36	608.1	21.91
10	2	14	5.6	12	2	254.78	1179.37	17.35
.
200	2	17	5.6	12	2	276.73	2122.53	18.74

Table 2. Adopted structural components of BPNN-CGB neural network for identifying in turn: efficiency $W_{(N)}$, unit loss S_j and unit cost K_j at specified output transport distances.

Distance [km]	Network structural components				
	number of inputs	number of hidden layers	number of neurons in hidden layer	number of outputs	number of epochs
1	5	1	8	1	200
2	5	1	8	1	200
3	5	1	8	1	200
5	5	1	8	1	200
7	5	1	8	1	200

The error value which determined the degree of learning of a given network was the principal criterion for ending the process. The root of the mean square error:

$$RMSE(P) = \sqrt{\frac{1}{P} \sum_{p=1}^P (z_i - y_i)^2}, \quad (7)$$

where:

y_i – the computed network output vector,

z_i – the target output vector,

P – the number of samples in the database, was used as the measure. The error was computed simultaneously for the training and testing data during the training of the particular neural networks.

4. Network training and testing results

Figure 4 illustrates the relation between the value yielded by the model simulating the operation of the machinery system and the value predicted by the BPNN-CGB neural network for an output transport distance of 1 km. The results prove that the BPNN-CGB neural network correctly maps the training data and correctly identifies the testing data – as evidenced by the location of the points close to the centre line corresponding to the ideal mapping and by the fact that very high values of correlation coefficient R (Figure 4) were obtained for both training and testing.

Figure 5 shows graphs of the training and testing $RMSE$ s versus the number of epochs for the adopted neural network for respectively: efficiency $W_{(N)}$, unit loss S_j and unit cost K_j at an output transport distance of 1 km. It follows from the figures that $RMSE$ rapidly decreases with the increasing number of epochs.

The correlation coefficient and $RMSE$ values for the BPNN-CGB network for identifying efficiency $W_{(N)}$, unit loss S_j and unit cost K_j at the particular output transport distances are compiled in Tables 3–5.

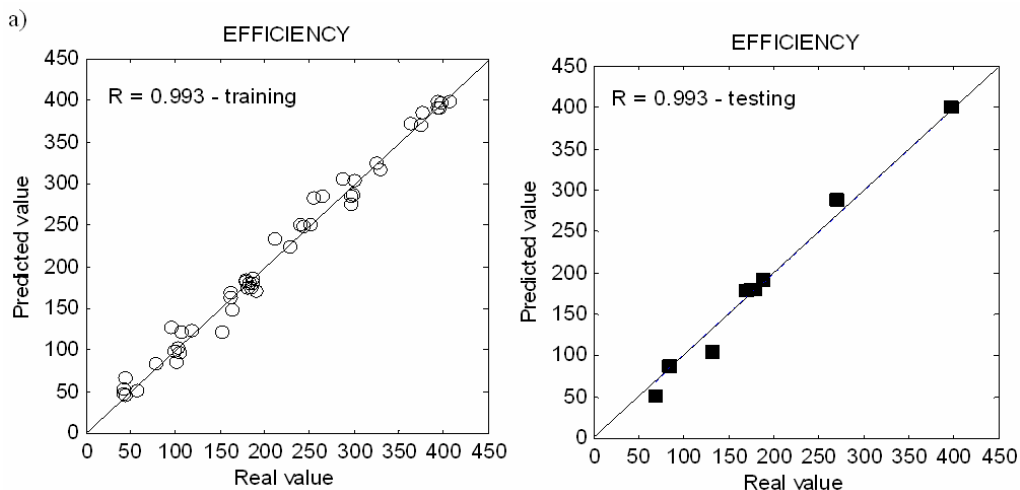


Fig. 4a. Relation between value yielded by model simulating operation of machinery system and value predicted by neural network (for training and testing sets) for: a) efficiency $W_{(N)}$

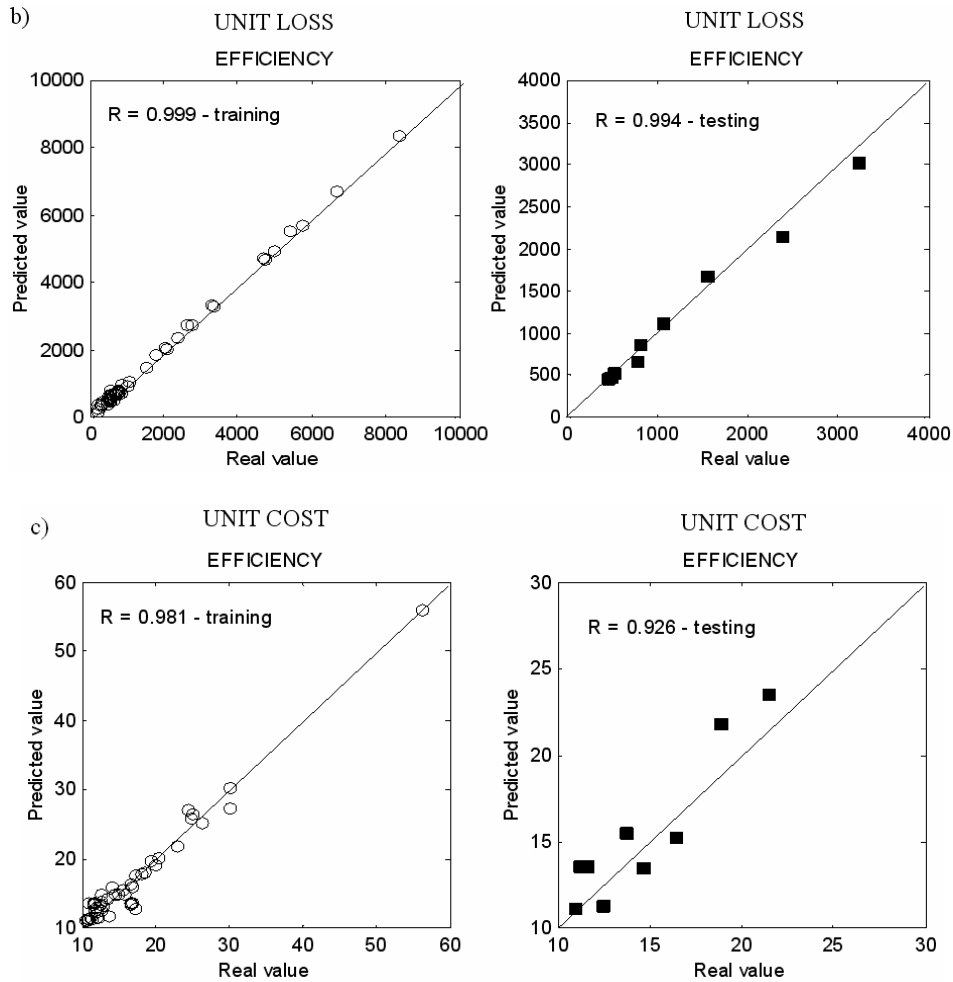


Fig. 4b,c. Relation between value yielded by model simulating operation of machinery system and value predicted by neural network (for training and testing sets) for: b) unit loss S_j , c) unit cost K_j and output transport distance of 1 km

Table 3. Correlation coefficient and $RMSE$ values for BPNN-CGB for identifying efficiency $W_{(N)}$ at specified output transport distances

Distance [km]	Correlation coefficient R [-]		Root Mean Square Error $RMSE$ [-]	
	training	testing	training	testing
1	0.993	0.993	0.0128	0.0148
2	0.988	0.993	0.0232	0.0240
3	0.992	0.989	0.0159	0.0232
5	0.994	0.989	0.0109	0.0188
7	0.996	0.995	0.0070	0.0132

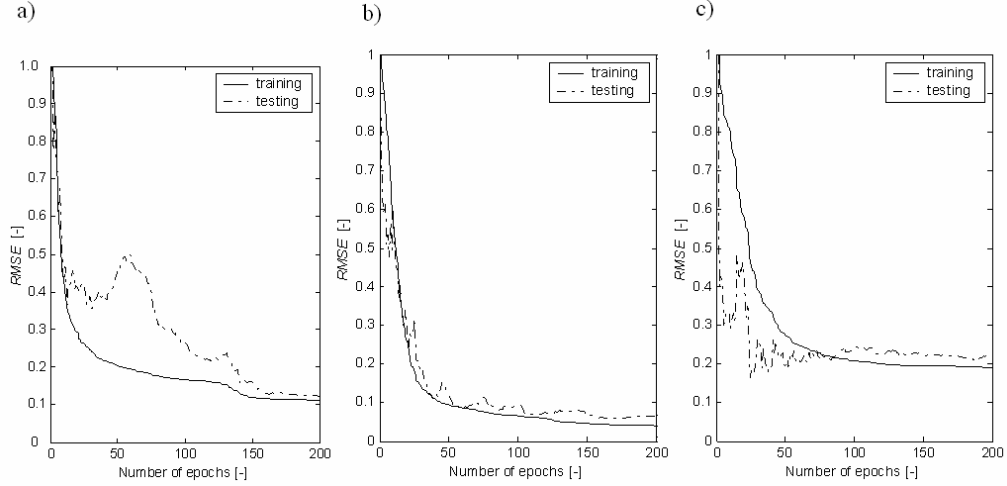


Fig. 5. $RMSE$ (for neural network training and testing) versus number of epochs for: a) efficiency $W_{(N)}$, b) unit loss S_j , c) unit cost K_j and output transport distance of 1 km

Table 4. Correlation coefficient and $RMSE$ values for BPNN-CGB for identifying unit loss S_j at specified output transport distances

Distance in [km]	Correlation coefficient R [-]		Root Mean Square Error $RMSE$ [-]	
	training	testing	training	testing
1	0.999	0.994	0.0016	0.0043
2	0.9806	0.9799	0.0383	0.0515
3	0.998	0.996	0.0047	0.0089
5	0.984	0.858	0.0321	0.0414
7	0.996	0.994	0.0077	0.0077

Table 5. Correlation coefficient and $RMSE$ values for BPNN-CGB for identifying unit cost K_j at specified output transport distances

Distance [km]	Correlation coefficient R [-]		Root Mean Square Error $RMSE$ [-]	
	training	testing	training	testing
1	2	3	4	5
1	0.981	0.926	0.0360	0.0518
2	0.995	0.801	0.0092	0.0067
3	0.984	0.944	0.0323	0.0294
5	0.990	0.884	0.0200	0.0239
7	0.999	0.556	0.0200	0.001

5. Conclusions

The results presented confirm the suitability of unidirectional multilayer error back propagation neural networks with a conjugate gradient algorithm (BPNN-CGB) for predicting such effectiveness ratios as: efficiency $W_{(N)}$, unit loss S_j and unit cost K_j of

systems of earthmoving machines working together, as evidenced by the low network training and testing $RMSE$ values and the high values of correlation coefficient R for testing. This has been demonstrated for different configurations of machines operating in a system consisting of c excavators and N means of transport at different output transport distances of 1, 2, 3, 5 i 7 km. Therefore it can be concluded that having a data set consisting of the technical parameters of earthmoving machinery systems and the corresponding effectiveness ratios obtained for different output transport distances one can train artificial neural networks and then use the latter for the reliable prediction of efficiency $W_{(N)}$, unit loss S_j and unit cost K_j .

References

- [1] Boussabaine A.H.: *The use of artificial neural networks in construction management: A review*, Construction Management & Economics, 14, 1996, pp. 427–436.
- [2] Fausett L.: *Fundamentals of neural networks – architectures*, Algorithms and Application. Prentice Hall Inc., Englewood Cliffs, New Jersey, 1994.
- [3] Filipowicz B.: *Stochastic models in operations research* (in Polish), WNT, Warsaw, 1996.
- [4] Gross D., Carl M. H.: *Fundamentals of queuing theory*, Wiley, 1998, pp. 439.
- [5] Gonnzalez-Quevedo A.A., AbouRizk S.M., Iseley D.T., Halpin D.W.: *Methodologies in Construction*, Journal of Civil Engineering and Management, ASCE, 119, 3, 1993, pp. 573–589.
- [6] Haykin S.: *Neural networks a comprehensive foundation*, MacMillan Pub.Co., New York, 1999.
- [7] Hegazy T., Ayed A.: *Neural network model for parametric cost estimation of highway projects*, Journal of Construction Engineering & Management, ASCE, 124, 3, 1998, pp. 210–218.
- [8] Hoła B., Mrozowicz J.: *Modelling of constructional processes having random character* (in Polish), Dolnośląskie Wydawnictwo Edukacyjne, Wrocław, 2003.
- [9] Hoła J., Kapelko A., Schabowicz K.: *Nondestructive assessment of the strength of self-compacting concrete*, Proc., 4th International Conference Techsta, Prague, 2004, pp. 38.
- [10] Hoła J., Schabowicz K.: *Application of artificial neural networks to determine concrete compressive strength based on non-destructive tests*, Journal of Civil Engineering and Management, 11, 1, 2005, pp. 23–32.
- [11] Hoła J., Schabowicz, K.: *Beurteilung der Betonfestigkeit unter Nutzung der kunstlichen Neuronalen Netze aufgrund zerstörungsfreier untersuchungen* (in German), Beton-Stahl-betonbau, 5, 2005, pp. 416–421.
- [12] Hoła J., Schabowicz K.: *Methodology of the neural identification of the strength of concrete*, ACI Materials Journal, 102, 6, 2005, pp. 459–464.
- [13] Hoła J., Schabowicz K.: *New technique of nondestructive assessment of concrete strength using artificial intelligence*. NDT & E International, 38, 4, 2005, pp. 251–259.
- [14] Marzouk M., Moselhi O.: *Simulation optimization for earthmoving operations using genetic algorithms*, Construction Management and Economics, 20, 6, 2002, pp. 535–543.

- [15] Marzouk M., Moselhi O.: *Object-oriented simulation model for earthmoving operations*, Journal of Construction Engineering and Management, ASCE, 129, 2, 2003, pp. 173–181.
- [16] Marzouk M., Moselhi O.: *Multiobjective optimization for earthmoving operations*, Journal of Construction Engineering and Management, 130, 1, 2004, pp. 105–113.
- [17] Schabowicz K., Hoła J.: *Artificial neural networks as applied to identification of the HPC strength using NDT*, Proc., Fifth Inter. Conference, ACI, Cancun, Mexico, 2002, pp. 300–317.
- [18] Schabowicz K.: *Neural networks in the NDT identification of the strength of concrete*. Archives of Civil Engineering, 51, 3, 2005, pp. 371–382.
- [19] Schabowicz K., Hoła, B.: *Mathematical-Neural model for assessing productivity of earthmoving machinery*. Journal of Civil Engineering and Management, Vol. XIII, No. 1, 2007, pp. 47–54.
- [20] Shi J.J.: *A neural network based system for predicting earthmoving production*, Construction Management & Economics, 17, 1999, pp. 463–471.
- [21] Smith S. D., Osborne J.R., Forde M.C.: *Analysis of Earth – moving Systems using discrete-event simulation*, Journal of Construction Engineering and Management, ASCE, 121, 4, 1995, pp. 388–396.
- [22] Tam C.M., Tong T.K.L., Tse S.L.: *Artificial neural networks model for predicting excavator productivity*, Engineering Construction & Architectural Management, Vol. 9, 5–6, 2002, pp. 446–452.
- [23] Waszczyszyn Z.: *Neural networks in the analysis and design of structures*, CISM Courses and Lectures No. 404, Springer, Wien-New York, 1999.

Zastosowanie sztucznych sieci neuronowych do predykcji wskaźników efektywności układów maszyn do robót ziemnych

Wiele procesów budowlanych realizowanych jest przy pomocy współpracujących ze sobą maszyn tworzących układy technologiczne zwane również ciągami lub łańcuchami technologicznymi. Przykładem takiego technologicznego układu może być zestaw maszyn do robót ziemnych składający się z koparek oraz środków transportowych. W pracy przedstawiono zastosowanie sztucznych sieci neuronowych do predykcji takich wskaźników efektywności jak: wydajność $W_{(N)}$, straty jednostkowe S_j oraz koszty jednostkowe K_j układów współpracujących maszyn do robót ziemnych. Z rezultatów badań wynika, że dysponując zbiorem danych składającym się z parametrów technicznych układów maszyn do robót ziemnych oraz odpowiadającym tym parametrom wartościom wskaźników efektywności, można nauczyć sztuczne sieci neuronowe, a następnie wykorzystać je do wiarygodnego neuronowego predykowania $W_{(N)}$, S_j oraz K_j .



Drop forging of HSLA steel with application of thermomechanical treatment

P. SKUBISZ, A. ŁUKASZEK-SOŁEK, J. SIŃCZAK, S. BEDNAREK

AGH – University of Science and Technology, al. Mickiewicza 30, 30-059 Kraków, Poland

Problems of realization of thermomechanical treatment for microalloyed-steel forgings are presented. The issue is discussed on the example of high-pressure-pump crankshaft. On the strength of numerical analysis results conditions for favourable strain and temperature distribution were determined. In addition, by means of numerical modelling proper perform geometry was designed, which allowed elimination of costly trials in industrial conditions, necessary especially for this part due to inclination to fold formation. The knowledge of precipitation kinetics in the analysed steel in combination with the obtained profiles of temperature made it possible to determine appropriate forging temperature, time, rate and a scheme of cooling. The experimental tests run in industrial conditions confirmed reasonability of assumed technology. Mechanical testing proved required high ultimate strength and yield stress and ductility.

Keywords: *thermomechanical treatment, controlled cooling, mechanical properties, numerical modelling, hardness, yield stress*

1. Introduction

The needs of automotive industry and the economics of processing industry induced research for new grades of steels characterized by high strength, high yield stress, crack resistance and good weldability [1]. Traditionally, forgings of components of transmission systems, suspension or crankshafts used to be made of carbon steels subjected to quenching-tempering treatment. Additions of alloying elements and controlled processing depending on a synergic combination of plastic deformation and heat treatment is now a common way of reducing manufacturing costs to improve mechanical properties of steel [2, 3].

Efforts to introduce Nb into steel for hot-rolled sheets gave rise to development of important group of microalloyed steel, important for technical and economical reasons [4]. Benefits of microadditions in steel were fully revealed in High Strength Low Alloy steels (HSLA). Their final properties are provided directly after deformation process as a result of controlled cooling [5].

The first tests of air-cooling directly from hot-working temperature date back to the seventies, which resulted in producing so-called 1st generation microalloyed steels. The most common steel of this group, 49MnVS3 – medium-carbon steel with vanadium additions, was used for manufacture of responsible components such as crankshafts. Despite relatively high level of strength, hardness of those steels was relatively

low. To increase hardness silicon in content of 0.5% was added and simultaneously carbon was reduced to 0.38–0.27%. These additions were also to improve weldability and castability. The decrease in strength was compensated with high manganese (>1%), with minor content of nitrides and carbides forming elements. In following years new steels group was developed, giving rise to so called 2nd generation of microalloyed steels. Steel 38MnSiV5 may be referred to as a representative of this group [6, 7]. Since then, constant development in this field has been witnessed, with steel precipitation hardened during controlled cooling directly from the deformation temperature. Vast majority of application of these grades involved hot-rolling processes, while in forging processes, on account of more complex determination of process parameters, these steels were not so readily used.

This days stale “SiV” steels are produced, which exhibit high strength and hardness, as well as good crack resistance and weldability associated with low carbon content. These steels have ferrite-perlite structure. Currently, contribution of products made of microalloyed steels in well-developed countries reaches 50% of the total amount of steel used in automotive industry and still an ever-increasing tendency is observed [9]. It is estimated that utilization of these sorts of steels with thermomechanical processing in the manufacture of automotive forged parts brought manufacture savings of about 20%. What is more, structural components of HSLA steel, as compared to traditional structural steels can bear the same loads at smaller cross-sections.

To benefit from thermomechanical treatment (TMT) in a forging process some technological setbacks must be overcome. They arise from diversity of shapes and sizes of forged parts, which calls for the necessity of determination unique forging and cooling process parameters [3]. The mechanical properties of forged components made of microalloyed steels are obtained by proper determination of forging process conditions, such as preheating temperature, forging temperature, dwell time and time of intervals between consecutive operations, as well as cooling conditions after completing the forging operations. Additional issue is a preheating temperature which must provide good forgeability as to obtain desired geometry at minimum number of blocker impressions and, on the other hand, appropriate temperature from the microstructure standpoint; keeping some of carbides undissolved and preventing from grain growth.

As-forged material condition is reflected by the condition of microstructure resultant from strain distribution and temperature gradients in the volume. The nature of the forging process itself introduces additional variables which contribute to possible non-uniformity of obtained microstructure after forging. In case of complex parts, some sections significantly differ in thickness, causing both nonuniform distribution of deformation and local increase in strain rate, and in result, significant amount of deformation heat. Complex geometry produces a metal flow pattern resulting in completely different time of contact of deformed metal with tool surface. Although the temperature differences diminish during subsequent stages before cooling, such as trimming

operation, in the aftermath of the temperature and strain gradients, local differences of microstructure occur, for instance in the form of grain size variations [8].

In the work, the possibility of utilization thermomechanical treatment in forging high-pressure pump crankshaft of steel 38MnSiVS6 is investigated. To take possible advantage of the benefits offered by combination of microalloyed steel application and utilization of heat attained after forging knowledge of actual temperature profile and strain gradients in characteristic cross-section of the part can be expected is necessary. For this reason numerical calculations of the whole technological cycle is needed, which in combination of the knowledge of included in numerous literature sources, data on precipitation kinetics form a sort of input data for controlled cooling parameters. In addition to determination of temperature and strain fields, numerical modelling was aimed at design of proper technology, which allowed elimination of costly trials in industrial conditions, necessary especially for this part due to high sensitivity of the geometry to fold formation.

2. Numerical modelling

The main goal of the research was determination of technological conditions for manufacture of drop forgings of elongated shape and changing cross-section, meeting following requirements: ultimate strength 820 MPa, yield stress 550 MPa, elongation to fracture 12%, area reduction at fracture – 22%. Accomplishment of the goal was realized for the forging of a high-pressure pump crankshaft with utilization of 38MnSiVS6 type microalloyed steel (Table) dispersion hardened with application of BY thermomechanical treatment.

The first part of the research depended on design of the most convenient manner to carry out the forging, with a focus on finding the proper billet dimensions to fill up varying in transverse dimensions die impression (Figure 1b) without excessive flash, and proper kinematics of forging equipment. It was assumed that the process should involve minimum forging stages, most favourable single-stage forging, and throughout the whole length of the part length uniform degree of deformation in the cross-section is produced. This stage of the work was based on numerical calculations of the processes conducted on mechanical press and a forging air-steam hammer. Forging billet preheating temperature was determined with a concern of proper initial structure and as such, 1050 °C was assumed. The remaining boundary conditions were corresponding to the conditions of the industrial tests (tool temperature 300 °C, friction factor 0.4 (graphite based lubricant), rotation per minute 40 for 320 mm crank radius (mechanical press). The numerical calculations were carried out with use of commercial code QForm3D on the assumption of viscoplastic model of a deformed body and rigid dies.

Table. Chemical composition of the steel used in the study (steel 38MnSiVS6)

Element	C	Si	Mn	P	S	V	Al
Content, %	0.36	0.56	1.35	0.008	0.055	0.08	0.012

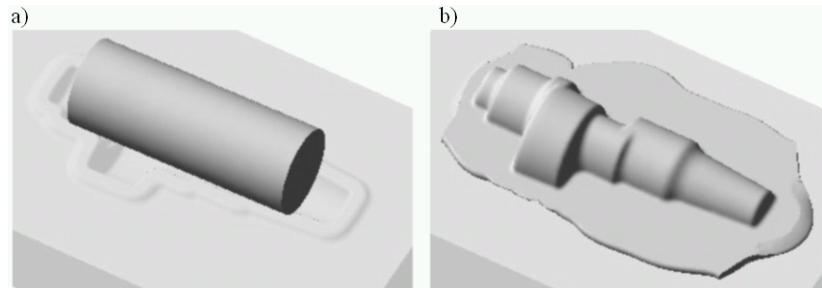


Fig. 1. Simulation of drop forging process of high-pressure pump shaft:
a – placement of the billet, b – end of the process

In the result of the analysis of cross-sections diagram of the rough part two diameters of a billet were proposed: 50 mm and 45 mm (Figure 1a). From the material saving standpoint it was concluded that billet of diameter 45 mm is more advisable as it ensures fill up of the impression with less material excess in a flash. The numerical calculation showed also that the billet used is too sensitive to laps formation and underfilling occurrence in the parting plane area when forged on hammer (Figure 2a). As forging on hammer requires a few blows there is a risk of unstable billet placement in-between. These problems did not occur in forging on mechanical press (Figure 2b).

Furthermore, which is of more significance, the process carried out on a hammer is less effective and hard to automate and as such does not provide full consistency of produced pieces, especially in a crucial aspect of temperature distribution prior to controlled cooling. Because of high speed (high strain rate), in cross-sections of higher deformation large amount of deformation heat was produced as compared to those of bigger diameter, which led to large temperature gradients. Therefore, mechanical press was used in the experiment.

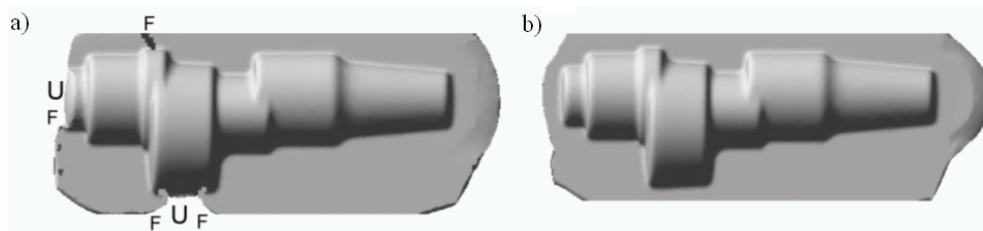


Fig. 2. Fill up of die impression in forging the shaft:
a – forging hammer, b – mechanical press (*U* – underfilling, *F* – fold)

In the geometry of the analysed shaft six characteristic cross-sections can be distinguished (Figure 3a). For these sections maps of effective strain distribution (Figure 3b) were determined, based on the results of computer simulation of part forged from 45 mm billet. It was concluded that in all of the cross-sections the character of strain

distribution is uniform. Also variations in the level of effective strain values between individual cross-sections were not significant. As expected, the largest values were observed for smaller diameters and in a cross-section, maximum values were in the vicinity of the flash. Through the whole length of the part, in the axis of the shaft insignificant fluctuations in the level of deformation occurred. Minimum value of effective strain in the axis of the part was 0.7 (Figure 3, cross-section E). Thus it can be concluded, that proposed single-stage technology of forging directly from a cylindrical billet is appropriate and should provide uniform distribution of final mechanical properties after controlled cooling.

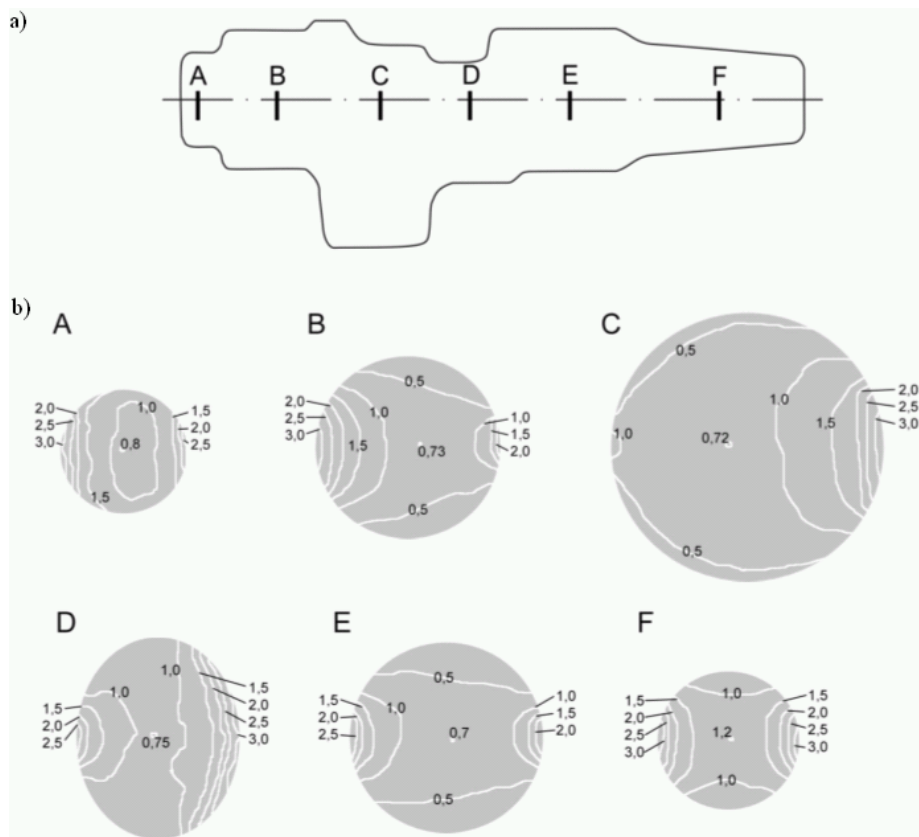


Fig. 3. Effective strain distribution ($A-F$) in characteristic cross-sections (a)

3. Results of experiments

Controlled cooling was carried out directly after forging in a special isolated assembly (Figure 4), which included six cooling stations (S_1-S_6). Each of the stations was independently controlled with possibility of linear control of the intensity of

cooling, as well as the time of subject to the action of a cooling medium, which enables provision of unique cooling conditions for given part configuration. In order to obtain the required temperature, estimated numerically prior to the tests, variations in the working parameters of three first stations were applied. Eventually, two considerable variants were obtained, resulting in temperature plots shown in Figure 5.

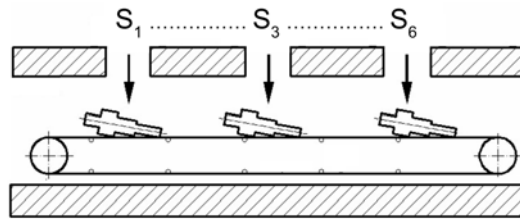


Fig. 4. Scheme of the controlled cooling line, S_1 – S_6 – cooling zones

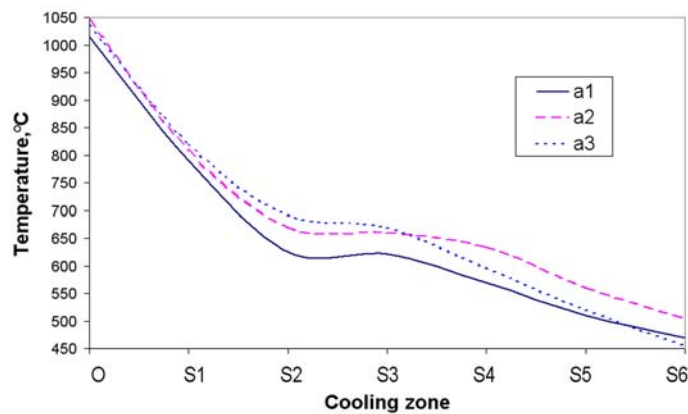


Fig. 5. Temperature of the part during a cooling: a_1 , a_2 , a_3 – variants of cooling, O – end of forging temperature, S_1 – S_6 – cooling zones

As mentioned, in the research a several variants were carried out, differing in cooling conditions. From the obtained parts samples for mechanical testing were taken out. Results of three of them giving the best strength and plasticity indices are presented in Figures 6 through 8. The first two tests (curves a and b in Figure 5) gave increased plasticity, but did not fulfill the assumptions of reaching minimum required ultimate tensile strength (Figure 6), which called for rearrangement of settings of the cooling stations. Therefore next attempts were made, with increased cooling intensity at station III. Introduction of the additional cooling station with modified parameters of the first two stations gave satisfactory results (column 3 in Figures 6–8) meeting the requirements of minimum ultimate tensile strength (800 MPa) and tensile yield stress (550 MPa) – reaching $R_m = 820$ MPa and $R_e = 560$ MPa, respectively.

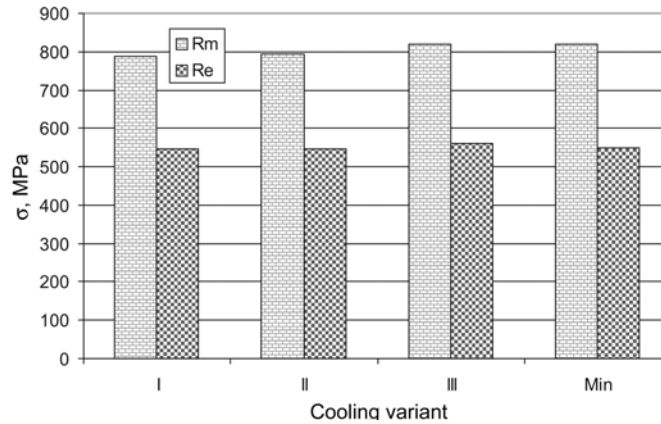


Fig. 6. Ultimate tensile strength and tensile yield stress of forgings made of steel 38MnSiVS6 with utilization of controlled cooling

Plasticity indices – area reduction at fracture (Z) and elongation at fracture (A5) from the first two variants significantly exceeded the required minimum (Figure 7). In the third variant of cooling (column III, Figure 7) a slight decrease of plasticity in relation to variants I and II was observed, however, still significant surplus over the required level was attained (column Min in Figure 7).

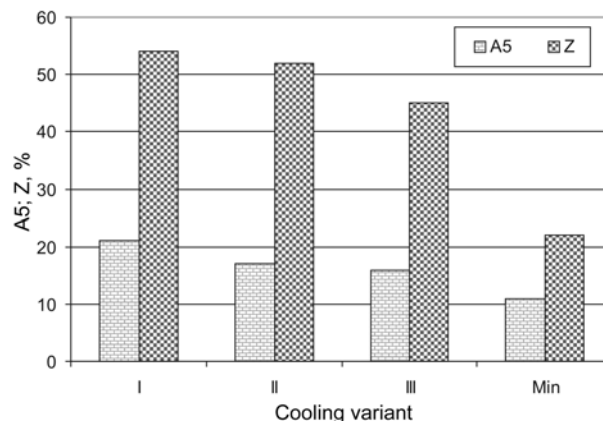


Fig. 7. Elongation and area reduction-at-fracture values obtained from mechanical testing of forgings made of steel 38MnSiVS6 with utilization of controlled cooling

In order to investigate effect of strain and temperature on the uniformity of the mechanical properties indicated by uniform distribution of effective strain in numerical calculation, hardness measurements in the longitudinal section of the part were made. The measurements were carried out for two cases of cooling scheme in five points marked with numbers 1 to 5 (Figure 8). The results indicate fluctuation throughout the

length of the part. However, character of these fluctuations exhibit a tendency corresponding to cross-sectional dimensions of individual location, which proves effect of cooling rate, both during the filling of the cavities and final continuous cooling.

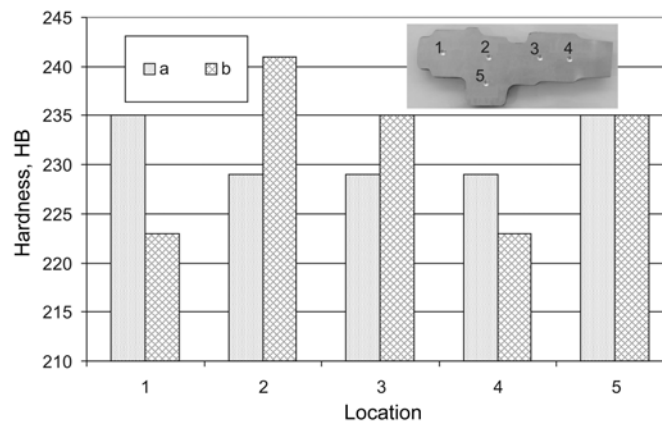


Fig. 8. Results of hardness measurement in a lengthwise cross-section of forgings made of steel 38MnSiVS6 with utilization of BY treatment (*a*, *b* – forgings obtained from two continuous cooling variants, 1–5 measurement locations)

4. Summary and conclusions

The presented efforts of utilization of controlled cooling directly after forging gave satisfactory results. To ensure realization of any cooling variant settings of three cooling zone were changed, starting with only two of the cooling zones. Mechanical testing of the specimens derived from the obtained parts indicate significant surplus of plasticity indices in all analysed variants of controlled cooling reaching 45 to 54% area reduction and 17 to 21% elongation at fracture, which is approximately twice as much as expected minimum. The high plasticity was accompanied by tensile strength nearly reaching 800 MPa (required minimum), increased to exceed this level after introducing additional cooling zone.

Prior to the experimental trials numerical modelling was carried out to estimate the end-of-forging temperature for two kinds of equipment: forging hammer and mechanical press. It was concluded that mechanical press goes along the needs of a forging process with a view to apply thermomechanical treatment as it provides consistency of temperature distribution and control of its level.

Owing to numerical calculation in the field of the metal flow the possibility of realization of forging in single-stage operation was designed despite complex part geometry. In this respect again mechanical press offers more advantages over hammer, preventing from flow defects formation and making it easier to control times and temperature of consecutive operations due to possibility of automation.

Results obtained from numerical modelling show slight fluctuations of effective strain and insignificant temperature gradients in differing in diameter cross-sections, which was confirmed by hardness measurement in the axis of the forged shaft on the lengthwise cross-section. Relatively low hardness may be an advantage during final machining of the part.

Obtained results of controlled cooling directly after forging small components of microalloyed steel indicate the possibility of using it for more compact or larger parts. Application of continuous cooling line with independent control of the cooling intensity in individual cooling zones makes it possible to produce unique cooling conditions dependent on the part geometry. From economical standpoint it offers reduction of production time, material costs and energy consumption.

Acknowledgement

Financial assistance of MEiN is acknowledged, agreement nr 11.11.110.559

References

- [1] Jahazi M., Eghbali B.: *The influence of hot forging conditions on the microstructure and mechanical properties of two microalloyed steels*, Journal of Materials Processing Technology, 2001, 113, pp. 594–598.
- [2] Marcisz J., Garbarz B.: *Design of production technology for ultrafine grained steel using thermomechanical treatment*, [Projektowanie technologii wytwarzania stali ultradrobnoziarnistej metodą obróbki cieplnoplastycznej], Hutnik – Wiadomości Hutnicze, 2006, 3, pp. 86–91.
- [3] Sińczak J., Łukaszek-Solek A., Skubisz P., Bednarek S.: *Impression-die forging of a flange with utilization of thermomechanical treatment*, [Kucie matrycowe odkuwki kołnierza z zastosowaniem obróbki cieplnoplastycznej], Hutnik – Wiadomości Hutnicze, 2007, 3, pp. 187–191.
- [4] Karabulut H., Gündüz S.: *Effect of vanadium content on dynamic strain ageing in microalloyed medium carbon steel*, Materials and Design, 2004, 25, pp. 521–527.
- [5] Chakraborty K., Chattopadhyay A.B., Chakrabarti A.K.: *A study on the grindability of niobium microalloyed forging quality HSLA steels*, Journal of Materials Processing Technology, 2003, 141, pp. 404–410.
- [6] Niechajowicz A., Tobota A.: *Warm deformation of carbon steel*, Journal of Materials Processing Technology, 2000, 106, pp. 123–130.
- [7] Ollilainen V., Kasprzeak W., Holappa L.: *The effect of silicon, vanadium and nitrogen on the microstructure and hardness of air cooled medium carbon low alloy steels*, Journal of Materials Processing Technology, 2003, 134, pp. 405–412.
- [9] Adamczyk J., Opiela M.: *Engineering of some metallurgical products of microalloyed structural steels [Inżynieria wybranych wyrobów hutniczych ze stali konstrukcyjnych mikrostopowych]*, Hutnik – Wiadomości Hutnicze, 2005, 3, pp. 162–170.

Proces kucia matrycowego stali HSLA z zastosowaniem obróbki cieplnoplastycznej

Przedstawiono zagadnienia dotyczące procesu obróbki cieplnoplastycznej stali z mikrodatkami. Zagadnienie omówiono na przykładzie procesu kucia wału pompy wysokociśnieniowej. Określono rozkład temperatury i odkształceń w objętości odkuwki w oparciu o obliczenia numeryczne procesu kucia. Ponadto przy pomocy modelowania numerycznego ustalono warunki poprawnej technologii kucia, dzięki czemu wyeliminowano bardzo kosztowne próby przemysłowe, które dla tej odkuwki były konieczne ze względu na skłonność do tworzenia zakuc. Znajomość kinetyki procesów wydzielenia w badanej stali w połączeniu z uzyskanymi rozkładami temperatury pozwoliło na określenie optymalnej temperatury kucia, czasu, szybkości i sposobu chłodzenia po kuciu. Wykonane próby przemysłowe potwierdziły zasadność przyjętej technologii. Badania wykazały uzyskanie wymaganego wysokiego poziomu własności wytrzymałościowych i plastycznych odkuwki.



Information about PhD thesis at the Civil Engineering Faculty and the Mechanical Engineering Faculty of Wrocław University of Technology

Title: *The ultimate load of masonry arch bridge spans taking into account influence of defects (in Polish)*

Nośność graniczna przęseł mostów murowanych z uwzględnieniem wpływu uszkodzeń

Author: Tomasz Kamiński

Supervisor: dr hab. inż. Jan Bień, Professor of PWr, Wrocław University of Technology

Promoting Council: Institute of Civil Engineering of WrUT

Reviewers:

Professor Jan Biliszczuk, Wrocław University of Technology,

Professor Wojciech Radomski, Warsaw University of Technology

Date of PhD thesis presentation: September 17th, 2008

PhD is available in Main Library and Scientific Information Centre of Wrocław University of Technology

The monograph contains: 217 pages, 122 figures, 46 tables, bibliography: 216 items

Keywords: *masonry bridge, analysis, test, Finite Element Method, defect, expert system*

Abstract: The presented work deals with the problem of the ultimate load assessment of masonry arch bridge spans including influence of various damage types. In the study various numerical approaches to the ultimate load evaluation based on the structural analysis as well as the expert tools supporting assessment of the ultimate load are proposed.

The applied techniques of the structural analysis are: kinematic method and the Finite Element Method (FEM). The kinematic method is based on the virtual work equation formulated for 2D system of rigid or rigid-plastic blocks representing the arch barrel and the soil backfill of the structures. All the critical aspects of the structural behaviour are captured, like limited compressive strength and negligible tensile strength of masonry, failure mode of the arch based on 4-hinge mechanism, passive pressure and live load distribution provided by the backfill.

FEM utilizes two- (2D) and three-dimensional (3D) models of masonry spans including masonry arch barrel, soil backfill and spandrel walls (in 3D models). For the arch barrel discretization an original mezomodelling technique is proposed. It consists in division of the arch into homogenised orthotropic masonry segments (representing a group of units and joints) and into individual homogeneous isotropic mortar joints. The technique is thoroughly compared with other common techniques (micro- and macromodelling) by means of simple and complex 2D and 3D cases. The proposed finite element (FE) models accommodate all the most advanced features which are: nonlinear elastic-plastic constitutive models of masonry and soil, contact

surfaces between soil and masonry or infinite elements representing the ground surrounding the structure.

Both approaches (kinematic and FE method) are used in wide-ranging parametric studies providing evaluation of the critical as well as negligible parameters of the models. The analysed parameters are: the number of masonry segments of the arch barrel division in the longitudinal and the transverse direction, localization and length of the live load, strength and density of the structural materials, modification of the boundary conditions of the soil and also presence of the spandrel walls considering various types of their connection to the arch barrel.

The proposed methods of analysis are verified by means of results of several laboratory and field destructive as well as non-destructive load tests of full-scale masonry arch bridges. A good agreement between calculations and experiments is found in the scope of both the ultimate load as well as the load-displacement relationship.

Both the kinematic and the FE method are adjusted to the analysis of the structures with various types of damage. Techniques of the damage implementation into the numerical models are presented and methodology for evaluation of the damage influence on the structure behaviour is proposed. The FE models are applied to extensive parametric study considering over 1000 cases taking into account various types, location, intensity and extent of damages.

Finally the received results of the ultimate load for intact and damaged structures are used as the knowledge base for creation of the expert tool supporting assessment of masonry arch bridges. The expert tool is designed and implemented by means of hybrid network technology utilising artificial neural networks and components based on mathematical functions. Details of the expert tool technology and methodology of its training and testing as well as an exemplary expert tool MyBriDE are presented.

Title: *Application of clinching to joining of thin-walled specimens absorbing impact energy (in Polish)*
Zastosowanie metod przetłaczania do łączenia profili cienkościennych absorbujących energię podczas zderzenia

Author: Sławomir Polak

Supervisor: Professor Zbigniew Gronostajski, Wrocław University of Technology

Promoting Council: Institute of Production Engineering and Automation, WUT

Reviewers:

Professor Professor Franciszek Grosman, Silesian University of Technology,

Professor Professor Maciej Pietrzyk, AGH – University of Science and Technology

Date of PhD thesis presentation: September 30th, 2008

PhD is available in Main Library and Scientific Information Centre of Wrocław University of Technology

The monograph contains: 127 pages, bibliography: 73 items

Keywords: *clinchng, joining, energy absorption*

Abstract: In recent years new materials, such as aluminium alloys, new-generation of steels and composites, have been increasingly used in the automotive industry. The use of such materials brings substantial benefits connected with their high strength and the vehicle's reduced weight and fuel consumption. Unfortunately the use of these materials sometimes imposes severe restrictions on the welding of aluminium and steel alloys, composites and metals or on the joining of elements with an intermediate layer between them.

The available literature does not provide any information on the dynamic deformation of thin-walled specimens joined by clinching. In the present paper, the capacities for absorbing kinetic energy by thin-walled specimens joined by clinching were researched. Double-hat thin-walled specimens joined by clinching methods: round press joining (RPJ) and square press joining (SPJ), were investigated. During the dynamic axial crushing test the behavior of thin – wall samples were better than in static test. There are the two most important parameters of clinching influencing on mode of deformation: technique and pitch of clinching. The experiments show that the RPJ clinching and application of pitch of 25 mm are the best as regards of mode deformation. They are deformed more progressive in both dynamic and quasi-static tests. In spite of lower crush force in static test, more often joining separation occurs in this test than in dynamic. The results show that clinch joining could be applied in controlled body crushing zones.

Information for Authors

Send to: *Archives of Civil and Mechanical Engineering*
Polish Academy of Sciences, Wrocław Branch
Podwale 75, 50-449 Wrocław, Poland

Archives of Civil and Mechanical Engineering (ACME) publishes both theoretical and experimental papers which explore or exploit new ideas and techniques in the following areas: structural engineering (structures, machines and mechanical systems), mechanics of materials (elasticity, plasticity, rheology, fatigue, fracture mechanics), materials science (metals, composites, ceramics, plastics, wood, concrete, etc., their structures and properties, methods of evaluation), manufacturing engineering (process design, simulation, diagnostics, maintenance, durability, reliability). In addition to research papers, the Editorial Board welcome: state-of-the-art reviews of specialized topics, letters to the Editor for quick publication, brief work-in-progress reports, brief accounts of completed doctoral thesis (one page is maximum), and bibliographical note on habilitation theses (maximum 250 words). All papers are subject to a referee procedure, except for letters, work-in-progress reports and doctoral and habilitation theses, which are briefly reviewed by the Editorial Board.

The papers submitted have to be unpublished works and should not be considered for publication elsewhere.

The Editorial Board would be grateful for all comments on the idea of the journal.

Detailed information about the Journal on web:

<http://www.pan.wroc.pl>

www.ib.pwr.wroc.pl/wydzial/czasopismoACME.html

<http://www.acme.pwr.wroc.pl>

<http://www.wmech.pwr.wroc.pl>

The papers should be submitted through the website

<http://www.acme.pwr.wroc.pl>

Price 15 zł
(0% VAT)

Subscription orders should be addressed to:
Oficyna Wydawnicza Politechniki Wrocławskiej
Wybrzeże Wyspiańskiego 27
50-370 Wrocław